

**Time-variable gravity field determination from
satellite constellations
- Swarm as an example**

Xinxing Wang

Vollständiger Abdruck der von der Fakultät für Bauingenieur- und Vermessungswesen der Technischen Universität München zur Erlangung des akademischen Grades eines

Doktor - Ingenieurs

genehmigten Dissertation.

Vorsitzende: Univ.-Prof. Dr.-Ing. Liqiu Meng

Prüfer der Dissertation:

1. Univ.-Prof. Dr.-Ing. Dr. h.c. Reinhard Rummel
2. Univ.-Prof. Dr. phil. nat. Urs Hugentobler
3. Prof. Dr. Per Knudsen, Technical University of Denmark

Die Dissertation wurde am 01.12.2010 bei der Technischen Universität München eingereicht und durch die Fakultät für Bauingenieur- und Vermessungswesen am 16.02.2011 angenommen.

Zusammenfassung

Seit ihrem Start am 17. März 2002 hat die Schwerefeldmission GRACE hochgenaue Daten zur Bestimmung von zeitvariablen Schwerefeldern geliefert. Die monatlichen GRACE-Lösungen zeigen deutlich den saisonalen Zyklus der kontinentalen Hydrologie, während die Mehrmonatslösungen das Abschmelzen polarer Eismassen in der Antarktis und Grönland, die Postglaziale Landhebung in Kanada und den globalen Meeresspiegelanstieg offenlegen. Aus diesem Grund sind GRACE-Lösungen weit verbreitet in geowissenschaftlichen Disziplinen wie Hydrologie und Ozeanographie.

Zukünftige Missionen werden spezielle Satellitenkonstellationen verwenden, um das zeitvariable Schwerefeld, welches auf die globalen Massentransporte im System Erde zurückzuführen ist, noch deutlicher zu bestimmen. In dieser Arbeit wird eine Closed-Loop-Simulation durchgeführt, um diverse Konstellationen zu analysieren. Als Ausgangspunkt für die Simulation dient die Magnetfeldmission Swarm der ESA, die aus drei Satelliten besteht und 2012 gestartet wird. Da jeder von diesen Satelliten mit GPS-Empfänger und Beschleunigungssensoren ausgestattet ist, kann die Konstellation auch für Schwerefeldschätzung genutzt werden. In dieser Hinsicht ist Swarm vergleichbar zu drei CHAMP Satelliten, wohingegen jedoch neben der absoluten GPS-Positionierung auch relative GPS Messungen genutzt werden können um die Genauigkeit der Beobachtungen zu erhöhen.

Ein 24-Monats-Simulation zur Bestimmung des zeitvariablen hydrologischen Signals wird durchgeführt. Durch diese Simulation wird das Potential der Swarm Mission für zeitliche Schwerefeldschätzungen evaluiert. Es wird gezeigt, dass Swarm das Potential hat, das zeitvariable hydrologische Signal bis zu Grad und Ordnung 6 zu bestimmen. Darüber hinaus ist die Mission auch aus theoretischer Sicht von Interesse, weil sie verschiedene Arten von inter-satellite Basislinien kombiniert, wie z.B. cross-track (Swarm A-B), along-track/radial (Swarm A-C). Deshalb kann die Swarm Konstellation als Beispiel zur Analyse der Eigenschaften von unterschiedlichen Basislinien und deren Kombinationen verwendet werden. Neben GPS Beobachtungen werden auch GRACE-type K-Band Messungen simuliert. Es wird gezeigt, dass die tandem/pendulum Konstellation eine isotrope Fehlerstruktur aufweist und damit die beste Schätzung des hydrologischen Signals ermöglicht.

Alle Analysen basieren auf der energy balance Methode, die bereits erfolgreich für die Missionen CHAMP, GOCE und GRACE implementiert wurde. Für die zeitlichen Schwerefeldschätzungen sollte die Nicht-Konservativität der zeitlichen Variationen berücksichtigt werden. Bei Vernachlässigung der Tatsache, dass zeitliche Variationen nicht konservativ sind, wird ein Fehler eingeführt. Die Größe dieser Fehler für verschiedene zeitvariable Signale wird ausgewertet. Es zeigt sich, dass ein solcher Fehler für die kontinentale Hydrologie, welche nur mäßig mit der Zeit variiert, vernachlässigbar ist hinsichtlich dem derzeitigen Niveau der Messgenauigkeit. D.h. die spezielle Gleichung für statische Schwerefeldschätzungen kann noch verwendet werden.

Wenn man bedenkt, dass die CHAMP Mission beendet ist und die GRACE Mission voraussichtlich im Zeitraum 2013-2015 beendet werden wird, könnte Swarm tatsächlich die einzige LEO-Mission sein, die einen Beitrag zur zeitlichen Schwerefeldbestimmung in der nahen Zukunft leistet. Darüber hinaus könnte auch eine Kombination von Swarm und GRACE (falls die Mission bis dahin noch nicht beendet ist) dazu beitragen, zeitliche und räumliche Aliasingeffekte in den niedrigen Graden und Ordnungen zu reduzieren, da eine solche Kombination zu einer besseren Abtastung in Raum und Zeit führen könnte. Daher kann Swarm als willkommene Ergänzungsmision zu den dedizierten Schwerefeld Missionen betrachtet werden und Swarm wird wertvolle Informationen über das statische und zeitvariable Schwerefeld liefern.

Abstract

Since its launch in 2002, the GRACE mission has provided time-variable gravity field solutions for more than 8 years. The monthly GRACE solutions clearly show the continental scale hydrological cycle, while the long-term time series reveal trends in deglaciation in Antarctica and Greenland, the post glacial rebound in Canada as well as the sea level rise. GRACE solutions are widely used in hydrology, oceanography, ice, atmosphere, solid earth and other related Earth science studies.

Future gravity missions designed to determine the time-variable gravity field will use specific satellite constellations to extract signatures of global mass transport. In this dissertation a closed-loop simulation is set up to study various constellations. Starting point for the simulation is the magnetic field mission Swarm, an ESA mission to be launched in 2012, consisting of three satellites. Since each of them is equipped with both GPS receivers and accelerometers, the constellation can be used for gravity field recovery as well. In this respect Swarm is comparable to three CHAMP satellites where in addition to absolute GPS positioning, one could use relative measurements to increase the observation accuracy.

A 24-month-simulation is carried out to recover the time-variable hydrology signal. By this simulation Swarm's potential for time-variable gravity field recovery is evaluated. It is shown that Swarm has the potential to recover the time variable hydrology signal to about d/o 6, based on 2 years of data. In addition, the mission is of interest from a theoretical point of view, because it combines different types of inter-satellite baselines, i.e., cross-track (Swarm A-B) and radial/along-track (Swarm A-C). Therefore the Swarm constellation can be used as an example to evaluate characteristics of different baselines and combinations. In order to quantify the potential of these constellations in future mission scenarios, GRACE-type K-band inter-satellite links are included as well. The tandem/pendulum constellation is shown to outperform GRACE, which provides smaller error spectrum and isotropic error patterns.

All analyses are based on the energy integral approach, which was implemented successfully for static gravity field analysis of CHAMP and GOCE as well as for time variable gravity field analysis of GRACE. Still, in case of time-variable signals, the method has its peculiarities because it is usually applied in a specialized version which only holds in conservative fields. For time-variable gravity field recovery, the non-conservativeness of time variations should be considered. Neglecting the fact that time-variable fields are not conservative and still applying the specialized observation equation, an error will be introduced. The magnitude of this error for different time-variable signals are evaluated, where it is found that for continental hydrology, which is only moderately changing in time, the error effect can be neglected at the current level of accuracy, i.e., the specialized observation equation can still be applied.

Considering that GRACE may terminate in the time frame 2013 to 2015, Swarm may continue in time-series of gravity measurements until GRACE follow-on mission is in place. Given the fact that CHAMP has already terminated, Swarm could indeed be the only LEO mission contributing to temporal variations of the low degree spherical harmonics in the near future. Moreover, even a combination of Swarm and GRACE (if it still operates after the launch of Swarm) may help to reduce temporal/spatial aliasing in the low degree harmonics by providing a better sampling in space and time. Therefore, Swarm can be regarded as a welcome complementary mission to the dedicated gravity missions and will provide valuable information on both static and time-variable gravity fields in the near future.

Keywords: Swarm, time-variable gravity field recovery, energy balance approach, satellite constellation

Acknowledgement

I would like to express my special gratitude and appreciation to my supervisor, Prof. Dr.-Ing. Reiner Rummel for giving me the opportunity to work on this very interesting and challenging topic in an optimal environment. During his supervision of this work, he provided me with mentoring and guidance with great patience and always encouraged me to grow. Without his countless support I could never have accomplished this dissertation.

I would also like to thank my co-supervisors, Prof. Dr.phil.nat. Urs Hugentobler and Dr. Per Knudsen for reviewing my work and providing me valuable comments.

I would like to thank all my colleagues at the Institut für Astronomische und Physikalische Geodäsie for the best working environment and their help to solve the problems I encountered. In particular, I am thankful to Dr.-Ing. Dieter Egger, who has helped me with his great expertise in computer programming to develop the simulation tool. Also, I would like to acknowledge Dr.-Ing. Thomas Gruber, M.Sc. Weiyong Yi and Dipl.-Ing. Lieselote Zenner for the inspiring discussions and ideas.

Furthermore, I am grateful to Dr.-Ing. Christian Gerlach for sharing his expertise on the Swarm mission as well as his valuable comments and suggestions.

Most important of all, I thank my wife and my family for their constant support in my private life and research work.

This project has been carried in the context of the TUM IGSSE project “Mass transport in the Earth system” in cooperation with DTU Space, Technical University of Denmark. The financial support by Deutsche Forschungsgemeinschaft (DFG) through the TUM International Graduate School of Science and Engineering (IGSSE) is gratefully appreciated.

Contents

Zusammenfassung	i
Abstract	ii
Acknowledgement.....	iii
1. Introduction	1
1.1. Introduction to current satellite gravimetry missions	1
1.2. Motivation of using Swarm mission for gravity purposes	3
2. Methodology	6
2.1. Introduction to energy balance approach.....	6
2.2. Simplified error analysis based on the energy balance approach	11
2.3. Frequency analysis	14
3. Time-variable gravity signal analysis.....	19
3.1. Relation between mass and spherical harmonics	19
3.2. Continental hydrology	22
3.3. Atmosphere and ocean	25
3.4. Ocean tides	29
3.5. Non-conservativeness of time-variable gravity signals.....	31
4. Simulation studies	37
4.1. Introduction to the simulator	37
4.2. Introduction to simulated constellations.....	44
4.3. Static field recovery.....	47
4.3.1. Error-free simulation	47
4.3.2. Full-error simulation.....	51
4.4. Aliasing investigation.....	56
4.4.1. Temporal aliasing for continental hydrology	56
4.4.2. De-aliasing discussion for AO and ocean tides	58

4.5.	Time-variable hydrology signal recovery.....	59
4.5.1.	General results	60
4.5.2.	Hydrology recovery with K-band constellations.....	66
4.5.3.	Hydrology recovery with GPS-only constellations	72
5.	Conclusion and discussion	82
5.1.	Summary and conclusion	82
5.2.	Discussion	85
	List of abbreviations	87
	List of figures	88
	List of tables	90
	Bibliography	91

1. Introduction

1.1. Introduction to current satellite gravimetry missions

One of the central tasks of geodesy is to measure the Earth's gravity field. Depending on the measurement types, one usually speaks of terrestrial gravimetry and satellite gravimetry. Terrestrial gravimetry includes stationary gravimetry, marine and airborne gravimetry. In these approaches the gravity field is measured by gravimeters, i.e. accelerometers measuring gravitational accelerations. The terrestrial approach has the advantage that the measurements can achieve very high accuracy at local level and so that they can be used to resolve fine structures of the gravity field. The disadvantage is that they don't provide global coverage and the results are not of the same accuracy level at global scales.

Satellite gravimetry, on the other hand, enables observations of the gravity field with global coverage and homogeneous accuracy. With the launches of CHAMP (CHAllenging Minisatellite Payload, July 15, 2000), GRACE (Gravity Recovery And Climate Experiment, March 17, 2002) and GOCE (Gravity field and steady-state Ocean Circulation Explorer, March 17, 2009), this decade (2000-2010) has been the golden season for satellite gravimetry.

The CHAMP satellite mission was designed to study the Earth's gravity and magnetic fields as well as the Earth's atmosphere (Reigber [2000]). The mission was initiated and is operated by the GFZ-Potsdam (Helmholtz-Zentrum Potsdam Deutsches GeoForschungsZentrum) since its launch. With its end on September 19, 2010, CHAMP had a life time of more than 10 years, which is far more than its designed 5-year life time. CHAMP carried onboard a GPS receiver and an accelerometer, which made it possible to do precise continuous 3D positioning and to separate gravitational and non-gravitational forces. CHAMP has been a concept-prove and test bed for the more sophisticated gravity missions GRACE and GOCE, because both of them make use of the combination of GPS receiver and accelerometer as well. Moreover, the analysis of CHAMP data allows assessing the value of non-dedicated satellite missions carrying equivalent instruments for gravity field research, Swarm or COSMIC are examples of such kind.

GOCE is the first core mission within ESA's Earth Explorer program. The main objective of the mission is to provide a high-accuracy, high-resolution global model of the Earth's static gravity field and of the geoid. GOCE is innovatively designed with a drag-free control system and satellite gravity gradimetry (SGG) measurement system. The former is designed to compensate the atmospheric drag and the latter is the key measurement instrument of GOCE, which will provide unique high-frequency information about the Earth gravity field with very high accuracy (Ditmar and Klees [2002]). The measurement principle is based on the analysis of the differences in gravitational accelerations between 3 pairs of accelerometers (the gradiometer). In this way the second derivatives of the Earth's gravitational potential, the so-called gravity gradient, can be measured, which counteracts the attenuation effect of the gravity field at satellite altitude and thus provides very accurate results. This concept is in fact similar to the low-low satellite-to-satellite tracking (SST-II), which is implemented in GRACE. While the measurements of GRACE take place between two satellites separated about 220 km from each other, the GOCE gradiometer measures gravitational and rotational acceleration difference in 3D between accelerometers units which are only ± 50 cm apart from each other. Combined with high-low satellite-to-satellite tracking (SST-hl), GOCE will lead to high resolution global and regional models of the Earth's static gravity field improving spatial scales down to 200 km.

1.1 Introduction to current satellite gravimetry missions

More information on GOCE can be found e.g. in Rummel *et al.* [2002], Johannessen *et al.* [2003], Drinkwater *et al.* [2007] or <http://www.esa.int/livingplanet/goce>.

Different from CHAMP and GOCE, the GRACE mission focuses on the temporal change of the Earth's gravity field. Since its launch, it has been providing valuable information on the temporal gravity variations with monthly or sub-monthly resolutions for a scale of 600-1000 km for nearly a decade. The mission consists of 2 satellites in a leading-following constellation, where the separation of the two satellites is actively controlled to stay within 170 to 270 km. The distance between the two satellites and its 1st time derivative are measured by a K/Ka-Band Ranging (KBR) system with a very high precision. Each GRACE satellite is equipped with a horn antenna for transmission and reception of the K/Ka-band microwave signals. The phase-shift between generated and received signals is measured with an accuracy of about 0.2 $\mu\text{m/s}$ for range-rate and 10 μm for the range (Dunn *et al.* [2003], Tapley *et al.* [2004a]).

Time-variable satellite gravity measurements can be used to address a wide variety of problems in the Earth sciences. Any geophysical process that causes a significant redistribution of mass over scales of hundreds of kilometres is a possible target. Thus the GRACE solutions are widely used in hydrology, oceanography, ice and atmosphere or solid earth studies. As an example, Figure 1-1 shows the trend of the gravity variations derived from 8 years of GRACE data, expressed in water column in cm/year. It is clear to see the mass loss in Greenland, which is caused by the accelerated melting of its ice sheet in this decade. The accelerated ice melting occurs mostly around the coastline, especially in southern Greenland. According to Velicogna and Wahr ([2005 a, b], [2006 a, b]), an ice mass loss of $248 \pm 36 \text{ km}^3/\text{year}$, which is equivalent to a global sea level rise of $0.5 \pm 0.1 \text{ mm/year}$, can be determined from the GRACE data from April 2002 to April 2006. It is also clear to see the post glacial rebound (PGR) signals over Canada, which is the viscoelastic response of the solid Earth to glacial unloading over the last thousand years. The positive trend indicates the arising of the solid Earth due to melting of the former ice sheet, which was proved by independent measurements and model predictions (Peltier [2004], Velicogna and Wahr [2002]).

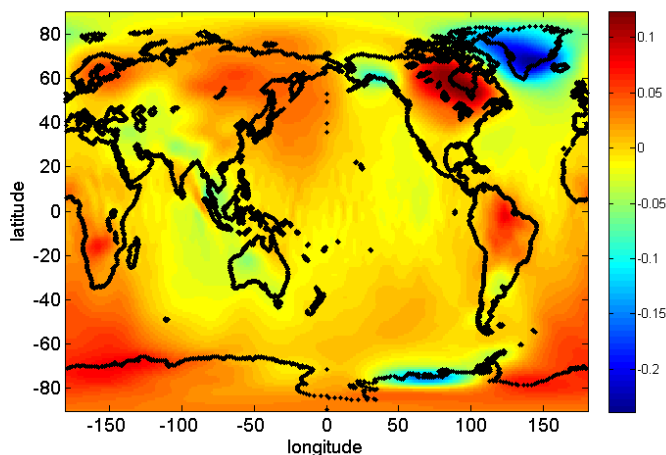


Figure 1-1 Trend derived from 8-years GRACE data, expressed in water column [cm/year]

GRACE, or in general spaceborne gravity missions aiming at the time-variable gravity field, have two distinct advantages over other techniques. First, gravity measurements provide a direct estimate of mass. Thus it is less ambiguous to interpret the results as mass changes, e.g. melting of ice sheet, than for other e.g. geometric techniques. For example, for airborne or spaceborne altimetry, the transformation of the measured elevations into mass variability of the ice sheets requires the density of the firm, which is usually poorly known. Second, GRACE measures the variations averaged over a broad region of the underlying surface, not just as point value directly beneath the satellite. Thus it inherently averages over large regions, which benefits the estimate of the total mass change. Altimetry, for example, samples the ice sheet at relatively small footprints, so that the estimate of total mass imbalance requires interpolations and extrapolations, which may introduce additional errors. Of course

GRACE has also disadvantages. On one hand, it cannot provide small-scale resolution, so it has difficulty fixing the exact location of a mass anomaly. On the other hand, GRACE measures only the total amplitude of the mass anomaly. It cannot distinguish between the different sources without additional information. For example, it is difficult to tell whether a mass anomaly detected in a continental region is in the atmosphere or in the water and snow on the surface, or in the water stored underground. Therefore, the best approach is to combine GRACE and altimetry as well as GPS observations to make use of the advantages of the different measurement systems.

GRACE has already passed the designed life of 5 years and it may terminate due to technical reasons (estimated to occur in 2013, Wiese *et al.* [2008]). Currently (10.2010) a follow-on mission and a gap-filler mission are in the planning phase but fixed schedules for such missions are not determined yet. It is therefore interesting to see if there can be a mission to continue the observation of the time-variable gravity field and to bridge the gap to the next dedicated GRACE-type mission, in case GRACE indeed fails. Since currently there is no other mission with low-low SST available, one has to focus on the missions with GPS-only measurement. The ESA magnetic field mission Swarm can be such a candidate mission.

1.2.Motivation of using Swarm mission for gravity purposes

The major part of the Earth's magnetic field has its origin in the outer fluid core. It is created by a self-sustaining dynamo process involving turbulent motions of molten iron. Since the launch of the Ørsted satellite (Neubert *et al.* [2001]) mission in 1999, a new era of satellite measurements for geomagnetic field has started. CHAMP (Reigber *et al.* [2002]) and SAC-C (Olsen *et al.* [2006]), both launched in 2000, have delivered high-precision geomagnetic data during the first years of this decade. However, all these three missions have been single-satellite missions. Although they share similar magnetic instruments, they have different science payloads, spacecraft designs and orbits. As a result they produce data with fairly different characteristics. This limits the scientific advantage of comparing data simultaneously acquired at different locations by different satellites. In particular, the irregularly varying fields produced by the external currents are then difficult to be modeled adequately. This is reported to be the main limiting factor in the accuracy of present geomagnetic field models (Friis-Christensen *et al.*, [2006]). Single-satellite missions simply cannot take full advantage of the instrument improvement achieved during the recent years. Thus, a dedicated multi-satellite mission making simultaneous measurements over different regions of the Earth is needed. Results from combined analysis of Ørsted, CHAMP and SAC-C data have confirmed this (Sabaka *et al.* [2004]). Swarm has been designed to be such a dedicated mission, which consists of three satellites with different orbit configurations to enable simultaneously measurements at different locations of the Earth.

The Swarm mission is based on a mission proposal (Friis-Christensen *et al.* [2002]) submitted in response to the ESA Earth Observation Programme call for Opportunity Mission proposals. Among 25 submitted proposals Swarm was one of the three candidates selected for feasibility studies. The Phase-A studies were finalized during 2004 and in May 2004 the Swarm mission was selected as the fifth Earth Explorer Mission in ESA's Living Planet Programme aiming at a launch in 2012 (Haagmans, R. (2004)).

The objective of the Swarm mission is to provide the best ever survey of the geomagnetic field and its temporal evolution, in order to gain new insights into the Earth system by improving the understanding of the Earth's interior and the geospace environments. More precisely, the Swarm mission will make it possible to derive the first global representation of the geomagnetic field variations on time scales from an hour to several years and directly address the challenging issue of

1.2 Motivation of using Swarm mission for gravity purposes

separating the contributions from the various field sources. Swarm has been specifically designed to simultaneously obtain a space-time characterization of both the internal field sources in the Earth's core, mantle, and crust, and the external current systems in the ionosphere and magnetosphere.

The primary research objectives of the mission are (Friis-Christensen *et al.* [2006]):

- Core dynamics, geodynamo processes, and core-mantle interaction,
- Lithospheric magnetisation and its geological interpretation,
- 3-D electrical conductivity of the mantle,
- Currents flowing in the magnetosphere and ionosphere.

In addition, two secondary research objectives have been defined:

- Identification of ocean circulation by its magnetic signature,
- Quantification of magnetic forcing of the upper atmosphere.

All three Swarm satellites feature scalar magnetometer, vector magnetometer, electric field instrument, GPS receiver and accelerometer onboard. More details about the onboard instrument and the measurement principle can be found in e.g. Kotsiaros [2009] or ESA SP-1279-6 [2004]. As the focus on this dissertation is not to recover the magnetic field but the gravity field with Swarm, the orbit constellation and the instrument combination GPS receiver – accelerometer are more of interest for this purpose. The orbit constellation is introduced in section 4.2, where simulation studies of such a constellation is carried out, while the specifications of the onboard GPS receiver and accelerometer can be found in ESA SP-1279-6 (2004). It is to notice that the accelerometer noise is not considered in the simulation studies in Chapter 4 and the GPS noise is considered to be white noise in this dissertation.

The onboard GPS receiver and accelerometer makes Swarm able to do precise 3D orbit determination and to observe non-gravitational forces. In this sense Swarm can be regarded as three single CHAMP satellites. Besides the GPS measurement for single satellites, it is also possible to derive GPS baselines between the satellites, which should be determined with an accuracy of one order of magnitude better than absolute GPS positioning (Visser [2006]). As CHAMP has already proved, Swarm should have the potential for static gravity field recovery. Furthermore, it is interesting to see if the more accurate baseline measurement can bring advantage in time-variable gravity field determination. Considering that GRACE may terminate due to technical reasons and a follow-on mission is still in planning, it is interesting to know if Swarm has the potential to determine the global time-varying signal of continental hydrology. In addition, Swarm is a very useful constellation from a theoretical point of view, because it combines baselines in all different directions, i.e. along-track (like GRACE), cross-track and radial (see e.g. Gerlach and Visser [2006]). It is well known, that the sectorial and near-sectorial coefficients are not well determined from an along-track mission like GRACE and the well known striping patterns in GRACE fields are the spatial representation of such an error structure. It is also known that other baseline constellations lead to different error structures. Therefore an analysis of such baselines and especially the combination of those are very useful for mission planning. Based on these considerations, this dissertation is dedicated to investigate the potential of Swarm in terms of static and time-variable gravity field determination via simulation studies.

Following the introduction in Chapter 1, Chapter 2 will describe the fundamental methodology and mathematics tools used in this dissertation. In section 2.1 an introduction to the energy balance approach is given for both static gravity field and time-variable gravity field determination. More generalized equations for computing the non-conservative time variations with the energy balance approach are derived and described briefly. Equations are given for both the single satellite case and satellite constellations. Section 2.2 gives a simplified error analysis based on the energy balance approach, which provides an estimation of the achievable accuracy in the simulation studies in Chapter 4. Besides the error budget for GPS measurements, GRACE-type measurement with K-band is also introduced. Section 2.3 describes several terms which will be used in frequency analysis of the time-variable gravity signals, including Fourier transform, sampling rule and aliasing as well as filtering of spherical harmonics.

Chapter 3 introduces and analyzes the time-variable gravity signals used in the simulation studies in Chapter 4. Section 3.1 links the spherical harmonics coefficients with the mass changes, explaining the principle for obtaining information about mass anomalies from the gravity products. Equations showing the calculation of the mass change on the surface of the Earth from spherical harmonics and vice versa are described. Section 3.2 deals with the analysis of the hydrology signal, in this dissertation represented by the LaD (Land Dynamic model). It begins with an introduction to the global water cycle, followed by the analysis of the LaD model. Atmosphere-ocean signal is analyzed in section 3.3, where the formulas of calculation of spherical harmonics coefficients from atmospheric and oceanic pressure data are introduced, followed by the spectral analysis of the atmosphere-ocean signal together as a system. Ocean tides signal is described in section 3.4, where tidal force, tidal potential are shortly explained. Section 3.5 discusses about the non-conservativeness of the time-variable gravity signals and demonstrates the error introduced by neglecting this property for direct tides, ocean tides, hydrology and atmosphere-ocean signals, respectively. The error is shown for both single satellite and 2-satellite-constellations.

In chapter 4 several simulation studies are carried out. The simulator and the simulated constellations are introduced in section 4.1 and 4.2, respectively. Starting from Swarm, the simulation is extended with different constellations and measurement principles. Static gravity field recovery simulation is carried out in section 4.3 and aliasing issue is discussed in section 4.4. In section 4.5 a 24-month-simulation is carried out, which attempts to recover the hydrology signal as well as its annual/semi-annual components.

Chapter 5 summarizes the results and achievements of this dissertation.

2. Methodology

2.1. Introduction to energy balance approach

One method to recover the gravity potential from satellite missions is the energy integral approach, which will be applied in the simulation studies of this dissertation. The method and its utilization in gravity field recovery has been discussed since the early days of satellite geodesy and successfully implemented after the launch of CHAMP in 2000, see e.g. Han *et al.* [2002], Gerlach *et al.* [2003] or Badura *et al.* [2005]. The approach has also been used for time variable gravity field recovery for GRACE (see Han [2004]) and is used as part of the time-wise approach for determination of the static field with GOCE (Pail *et al.* [2010]). In this section, an overview on the observational model, i.e., the energy integral, shall be given for both single satellites and satellite constellations like those used in the Swarm or GRACE missions. This does, however, not imply that the application of the method is restricted to these two examples.

Derivation of the Energy Integral

The Jacobi or energy integral for one satellite as given, e.g., by Hotine and Morrison (1969), reads

$$W - \frac{1}{2}\dot{\underline{x}}^2 = C \quad (2.1)$$

where C is an unknown constant, W is the gravity potential and \underline{x} denotes the velocity vector of the satellite in an Earth-fixed coordinate system. Separating the gravity potential into gravitational and centrifugal potential V and Z and solving for V, one finds the basic energy integral equation for gravity field determination

$$V = \frac{1}{2}\dot{\underline{x}}^2 - Z + C \quad (2.2)$$

This equation holds only in a static (conservative) gravity field, with no other forces acting but the Earth's gravitation. This becomes obvious by deriving the energy integral from the satellite's equation of motion, as was done by Schneider [1967]. The equation of motion reads

$$m \frac{d^2 \underline{x}}{dt^2} = \underline{F}, \quad (2.3)$$

where m is the mass of the satellite and \underline{F} is the sum of all forces acting on the satellite. Multiplying both sides of the equation with the satellite's velocity and assuming equality of inertial and the gravitational mass (thus m drops out and force \underline{F} is replaced by acceleration or specific force \underline{f} gives

$$\frac{d\underline{x}}{dt} \cdot \frac{d^2 \underline{x}}{dt^2} = \frac{d\underline{x}}{dt} \cdot \underline{f}. \quad (2.4)$$

Since for the left hand side it holds

$$\frac{d\underline{x}}{dt} \cdot \frac{d^2 \underline{x}}{dt^2} = \frac{d}{dt} \left(\frac{1}{2} \left(\frac{d\underline{x}}{dt} \right)^2 \right) \quad (2.5)$$

integration of equation (2.4) over time yields

$$\left(\frac{d\underline{x}}{dt}\right)^2 = \int_{\underline{x}} \underline{f} d\underline{x}. \quad (2.6)$$

From equation (2.6) it is obvious, that all accelerations \underline{f} need to be integrated along the satellites orbit. For conservative forces (like the Earth's static gravity potential W given in an Earth fixed frame) the integral can be replaced by the potential difference between the end points of the corresponding potential field. This means, that only potential differences with respect to the start point of an orbit arc can be derived. The full gravity potential is therefore only derived up to an unknown constant (which represents the integration constant, or the potential value at the start point of the orbit arc). Therefore one can write

$$\frac{1}{2}\dot{\underline{x}}^2 = W + \int_{\underline{x}} \underline{a} d\underline{x} + C \quad (2.7)$$

or equivalently

$$V = \frac{1}{2}\dot{\underline{x}}^2 - \int_{\underline{x}} \underline{a} d\underline{x} - Z + C, \quad (2.8)$$

where \underline{a} is the sum of all non-conservative forces. These are all surface forces acting on the satellite (like solar radiation pressure and atmospheric drag) as well as all time-variable gravitational and non-gravitational accelerations. If these forces are known, they can numerically be integrated along the orbit. Knowing the velocity of the satellite, the integration along the orbit can be replaced by the following integration over time

$$\int_{\underline{x}} \underline{a} d\underline{x} = \int_t \underline{a} \cdot \dot{\underline{x}} dt. \quad (2.9)$$

The Energy Integral for two Satellites

Potential differences between any two satellites can be computed by forming differences of two energy integral equations. Neglecting all non-conservative forces for the moment one can derive from equation (2.2)

$$V_2 - V_1 = \frac{1}{2}\dot{\underline{x}}_2^2 - Z_2 + C_2 - \left(\frac{1}{2}\dot{\underline{x}}_1^2 - Z_1 + C_1 \right) \quad (2.10)$$

or

$$V_{12} = \frac{1}{2}(\dot{\underline{x}}_2^2 - \dot{\underline{x}}_1^2) - Z_{12} + C_{12} \quad (2.11)$$

where the index combination $(\cdot)_{12}$ denotes relative quantities in the sense $(\cdot)_2 - (\cdot)_1$.

Rearranging the term in brackets, one can write

$$\left(\dot{\underline{x}}_2^2 - \dot{\underline{x}}_1^2\right) = \left(\dot{\underline{x}}_2 - \dot{\underline{x}}_1\right)^2 + 2\dot{\underline{x}}_1 \cdot \left(\dot{\underline{x}}_2 - \dot{\underline{x}}_1\right) = \dot{\underline{x}}_{12}^2 + 2\dot{\underline{x}}_1 \cdot \dot{\underline{x}}_{12} \quad (2.12)$$

Inserting (2.12) into (2.11) one finds the energy integral relation for any two satellites

$$V_{12} = \frac{1}{2}\dot{\underline{x}}_{12}^2 + \dot{\underline{x}}_1 \cdot \dot{\underline{x}}_{12} - Z_{12} + C_{12} \quad (2.13)$$

Energy integral for determination of the static gravity field

As shown in equation (2.8) and (2.9), the energy integral can be used to determine the static gravity field of the Earth according to

$$V = \frac{1}{2} \dot{\underline{x}}^2 - \int_t \underline{a} \cdot \dot{\underline{x}} dt - Z + C \quad (2.14)$$

where V is the static gravitational potential, Z the centrifugal potential, $\dot{\underline{x}}$ is the velocity vector of the satellite and \underline{a} is the sum of all non-conservative forces. The non-conservative forces include all surface forces acting on the satellite (solar radiation pressure, atmospheric drag, etc.) as well as all time-variable gravitational forces like tides or the effects from mass transport in the Earth system. In addition the energy integral equation (2.14) contains the unknown integration constant C , which must be estimated as an additional parameter for each continuous orbit arc.

In case of satellite constellations, the potential difference between any two satellites can be derived according to equation (2.13) as

$$V_{12} = \frac{1}{2} \dot{\underline{x}}_{12}^2 + \dot{\underline{x}}_1 \cdot \dot{\underline{x}}_{12} - \int_t (\underline{a}_2 \cdot \dot{\underline{x}}_2 - \underline{a}_1 \cdot \dot{\underline{x}}_1) dt - Z_{12} + C_{12} \quad (2.15)$$

where double indexing indicates differences between satellites, e.g., $V_{12} = V_2 - V_1$ is the potential difference between the locations of satellites 1 and 2.

Energy integral for determination of the time-variable gravity field

For time-variable gravity field determination one can split the accelerations \underline{a} in equation (2.14) in two components \underline{a}^m and \underline{a}^u , where the first represents the sum of all known (from models or measurements) gravitational and non-gravitational accelerations and \underline{a}^u are unknown time-variable gravitational accelerations. An example for the latter is the effect of continental hydrology, while the former contains measured surface forces or tidal effects known from models. Since \underline{a}^u are gravitational accelerations one can also replace them by ∇V^u for the single satellite case, or by ∇V_{12}^u for satellite constellations. Since time-variable effects are discussed, the gradients are spatial gradients at a specific epoch in a time-variable potential field, i.e., $\nabla V_{12}^u = \nabla V_{12}^u(t)$. Here it is assumed that the time-variable field can be expressed in time series of potential functions, i.e. it is allowed to express the field in potential for each epoch.

Then equations (2.14) and (2.15) can be re-written as

$$V + \int_t \nabla V^u \cdot \dot{\underline{x}} dt = \frac{1}{2} \dot{\underline{x}}^2 - \int_t \underline{a}^m \cdot \dot{\underline{x}} dt - Z + C \quad (2.16)$$

$$V_{12} + \int_t (\nabla V_2^u \cdot \dot{\underline{x}}_2 - \nabla V_1^u \cdot \dot{\underline{x}}_1) dt = \frac{1}{2} \dot{\underline{x}}_{12}^2 + \dot{\underline{x}}_1 \cdot \dot{\underline{x}}_{12} - \int_t (\underline{a}_2^m \cdot \dot{\underline{x}}_2 - \underline{a}_1^m \cdot \dot{\underline{x}}_1) dt - Z_{12} + C_{12} \quad (2.17)$$

The left hand side of the observation equations (2.16) and (2.17) is the basis for setting up the functional model of the parameter estimation process, while the right hand side is evaluated to generate the corresponding pseudo-observations. It is called pseudo-observation, because it serves as observation in the estimation process, while the original observations actually are satellite positions and acceleration measurements.

It is important to note, that only the static part of the gravitational field can be considered to be conservative. Thus, only for this static part the original line integral (see equation (2.6)) is path-independent and the integration can be replaced by corresponding potential differences along the orbit arc. In this specialized case (valid only in conservative fields) the functional model contains the potential V explicitly. But because the time-variable part is not conservative, the line integral can in general not be replaced by potential differences between the end points of the line and the corresponding time-variable potential is only implicitly introduced into the functional model by integrating gravitational gradients ∇V^u along the orbit.

In order to model the time evolution of the gravity field, the following standard procedure is recalled: one might set up a time series of potential fields, where each field is derived from observations of a certain time span and the potential is assumed to be either static through this period or it is modeled to follow a certain behavior, like a secular change. This is the standard procedure applied, e.g., in the processing centres at CSR, GFZ, JPL or others. In addition to a sequence of independent snapshots also Kalman filter solutions have been implemented to model the time evolution (Kurtenbach *et al.*, 2009). In general such strategies are reasonable as far as one can exclude aliasing effects due to unresolved short-periodic time variable effects within the chosen time span. Such effects arise, e.g., due to short periodic tidal, oceanic or atmospheric signals, which need to be removed before gravity field analysis.

If one uses the energy integral to transform satellite position and velocity (incl. low-low satellite-to-satellite-tracking) observations into potential values, one has (at least theoretically) to consider the left hand side of equations (2.16) or (2.17). There, the time variable part needs to be modelled by integrating the corresponding gravitational accelerations along the orbit. Otherwise an error will be introduced which arises from disregarding the non-conservativeness of time variable signal components. Such error will be demonstrated in section 3.5. This fact has already been pointed out by Sneeuw [2003a, c] based on general considerations on the treatment of non-conservative forces in the energy integral by Gerlach [2003].

Equations (2.16) and (2.17) show the rigorous observation models for time-variable gravity field analysis. Here both the static part V as well as the time-variable component V^u are unknown and need to be determined from either a single satellite or from a satellite constellation.

In order to set up the functional model for the estimation of the time-variable gravitational potential one might use the following expansion in spherical harmonics

$$V = \frac{GM}{R} \sum_n \left(\frac{R}{r} \right)^{n+1} \sum_m \bar{P}_{nm}(\cos \theta) \cdot (\bar{C}_{nm} \cos m\lambda + \bar{S}_{nm} \sin m\lambda) \quad (2.18)$$

or in compact notation

$$V = \sum_n \sum_m K_{nm} Y_{nm} \quad (2.19)$$

where K_{nm} are the fully normalized spherical harmonic potential coefficients of degree n and order m and Y_{nm} are the solid spherical harmonics, i.e., the product of associated Legendre functions $\bar{P}_{nm}(\cos \theta)$, the upward continuation factor $(R/r)^{n+1}$ and the sine and cosine terms; λ , θ and r are the spherical coordinates longitude, co-latitude and radius of the observation point.

In addition, one can model the time-variable potential coefficients as the sum of the static component K_{nm} , the linear drift term \dot{K}_{nm} and a periodic (e.g., half yearly or yearly) contribution of frequency ω

$$K_{nm}(t) = K_{nm}(t_0) + \dot{K}_{nm} \cdot (t - t_0) + K_{nm}^c \cos \omega t + K_{nm}^s \sin \omega t \quad (2.20)$$

2.1 Introduction to energy balance approach

Inserting (2.20) into the spherical harmonic series (2.18), one finds

$$V(t) = V(t_0) + \dot{V}(t-t_0) + V^c \cos \omega t + V^s \sin \omega t \quad (2.21)$$

where the first term corresponds to the conservative part in equations (2.16) and (2.17), while all of the last three terms contribute to the integral of non-conservative components. The left hand side of equation (2.16) then reads

$$V(t_0) + \int_t \nabla \left(\dot{V}(t-t_0) + V^c \cos \omega t + V^s \sin \omega t \right) \cdot \underline{\dot{x}} \, dt = V(t_0) + I(t) \quad (2.22)$$

where $I(t)$ represents the integral over all time dependent contributions. An analogous relation can be set up for potential differences from satellite constellations.

With this, the design matrix for estimating the unknown parameters contains the following columns for each time dependent coefficient

$$\begin{bmatrix} \frac{\partial V(t_0)}{\partial K_{nm}} & \frac{\partial I(t)}{\partial \dot{K}_{nm}} & \frac{\partial I(t)}{\partial K_{nm}^c} & \frac{\partial I(t)}{\partial K_{nm}^s} \end{bmatrix} \quad (2.23)$$

The first column contains just the partial derivatives of equation (2.19) with respect to the coefficients. The last three columns contain the partial derivatives of the integral $I(t)$ in equation (2.22) which contains the potential gradients

$$\nabla \left(\dot{V}(t-t_0) + V^c \cos \omega t + V^s \sin \omega t \right) = \nabla V^u = \begin{bmatrix} V_x^u \\ V_y^u \\ V_z^u \end{bmatrix} = \begin{bmatrix} \frac{\partial V^u}{\partial r} \cdot \frac{\partial r}{\partial x} + \frac{\partial V^u}{\partial \theta} \cdot \frac{\partial \theta}{\partial x} + \frac{\partial V^u}{\partial \lambda} \cdot \frac{\partial \lambda}{\partial x} \\ \frac{\partial V^u}{\partial r} \cdot \frac{\partial r}{\partial y} + \frac{\partial V^u}{\partial \theta} \cdot \frac{\partial \theta}{\partial y} + \frac{\partial V^u}{\partial \lambda} \cdot \frac{\partial \lambda}{\partial y} \\ \frac{\partial V^u}{\partial r} \cdot \frac{\partial r}{\partial z} + \frac{\partial V^u}{\partial \theta} \cdot \frac{\partial \theta}{\partial z} + \frac{\partial V^u}{\partial \lambda} \cdot \frac{\partial \lambda}{\partial z} \end{bmatrix} \quad (2.24)$$

Since formally, \dot{V} , V^c and V^s can be computed by simply replacing the potential coefficients K_{nm} in (2.19) by the corresponding coefficients \dot{K}_{nm} , K_{nm}^c and K_{nm}^s it holds

$$\frac{\partial(\nabla V)}{\partial K_{nm}} = \frac{\partial(\nabla \dot{V})}{\partial \dot{K}_{nm}} = \frac{\partial(\nabla V^c)}{\partial K_{nm}^c} = \frac{\partial(\nabla V^s)}{\partial K_{nm}^s} = \nabla Y_{nm} \quad (2.25)$$

With this, it follows for last tree partials in (2.23) for the single satellite case

$$\frac{\partial I(t)}{\partial \dot{K}_{nm}} = \int_t (t-t_0) \nabla Y_{nm} \cdot \underline{\dot{x}} \, dt \quad (2.26)$$

$$\frac{\partial I(t)}{\partial K_{nm}^c} = \int_t \cos \omega t \nabla Y_{nm} \cdot \underline{\dot{x}} \, dt \quad (2.27)$$

$$\frac{\partial I(t)}{\partial K_{nm}^s} = \int_t \sin \omega t \nabla Y_{nm} \cdot \underline{\dot{x}} \, dt \quad (2.28)$$

and for satellite constellations

$$\frac{\partial I(t)}{\partial \dot{K}_{nm}} = \int_t (t-t_0) (\nabla_2 Y_{nm} \cdot \underline{\dot{x}}_2 - \nabla_1 Y_{nm} \cdot \underline{\dot{x}}_1) \, dt \quad (2.29)$$

$$\frac{\partial I(t)}{\partial K_{nm}^c} = \int_t \cos \omega t (\nabla_2 Y_{nm} \cdot \underline{\dot{x}}_2 - \nabla_1 Y_{nm} \cdot \underline{\dot{x}}_1) \, dt \quad (2.30)$$

$$\frac{\partial I(t)}{\partial K_{nm}^s} = \int_i \sin \omega t (\nabla_2 Y_{nm} \cdot \dot{\underline{x}}_2 - \nabla_1 Y_{nm} \cdot \dot{\underline{x}}_1) dt \quad (2.31)$$

where $\nabla_i Y_{nm}$ indicates, that the gradient of the solid spherical harmonic Y_{nm} is evaluated at location of satellite i ($i=1, 2$).

Compared to the static component which contains just the solid spherical harmonics, the rigorous estimation of the time-variable potential coefficients is quite tedious. Here, the gradients of the solid spherical harmonics need to be integrated along the orbit. Thus it is interesting to see if one can skip these complex computation steps. To answer this, one needs to investigate how large the error due to neglecting the non-conservativeness of the time variations can be and to what extent this error will downgrade the recovery of gravity field. This issue will be discussed further in section 3.5 and 4.4.

2.2. Simplified error analysis based on the energy balance approach

As introduced in the last section, the energy balance approach is based on the energy conservation law, which states that in a conservative field, the sum of potential and kinetic energy is constant. In order to estimate the expected level of accuracy for the simulations in section 4.3 to 4.5, a simplified error analysis is performed here, which takes care of only the largest contribution in the error propagation, i.e., the velocity information of the satellites. Therefore all other terms (like centrifugal potential or non-conservative forces) are neglected and the simplified equations are written as

$$V \approx \frac{1}{2} \dot{\underline{x}}^2 \quad (2.32)$$

for the single satellite case and

$$V_{12} \approx \frac{1}{2} \dot{\underline{x}}_{12}^2 + \dot{\underline{x}}_1 \cdot \dot{\underline{x}}_{12} \quad (2.33)$$

for satellite constellations. Error propagation of equations (2.32) and (2.33) yields

$$\sigma_V^2 = \dot{\underline{x}}^2 \sigma_{\dot{\underline{x}}}^2 \quad (2.34)$$

and

$$\sigma_{V_{12}}^2 = \left(\dot{\underline{x}}_{12} + \dot{\underline{x}}_1 \right)^2 \cdot \sigma_{\dot{\underline{x}}_{12}}^2 + \dot{\underline{x}}_{12}^2 \cdot \sigma_{\dot{\underline{x}}_1}^2 \quad (2.35)$$

where $\sigma_{\dot{\underline{x}}_1}$ and $\sigma_{\dot{\underline{x}}_{12}}$ are the error standard deviations of absolute and relative velocities, respectively. In order to evaluate equations (2.34) and (2.35), some realistic values are introduced for the different quantities. These are given in Table 2-1. Hereby it is assumed, that the velocities are determined by means of GPS high-low satellite-to-satellite tracking. The accuracies of absolute and relative satellite velocities are assumed to be independent of the specific constellation, while the absolute values of relative velocities differ significantly for different constellations. Several constellation types are distinguished here: the constellations implemented in the GRACE and Swarm missions, i.e., an along-track baseline where two satellites follow each other on the same orbit (GRACE case with GPS only), a cross-track baseline, where two satellites fly side-by-side along slightly different orbits (here the longitude of the ascending node differs for about 1.4° as in case of Swarm baseline A-B) and a oblique or mixed baseline. This oblique baseline is a baseline between two satellites in about the same orbital plane, but in different altitudes. Due to the different orbital velocities in different altitudes, the oblique

2.2 Simplified error analysis based on the energy balance approach

baseline will be almost radial during some periods (periods of closest approach), while in other periods it will be almost along-track. In general it will be a mixture of along-track and radial components. In case the orbital planes are not identical there will be additional cross-track components. The baselines Swarm A-C or B-C are examples of such mixed baselines, where the orbital planes are almost identical to that of Swarm A/B in the beginning of the mission, while they will drift apart during the mission lifetime of 5 years for about 90, see Olsen *et al.* [2007] or Kotsiaros [2009]. Figure 2-1 shows the different observation geometries of the baseline between Swarm A or B and Swarm C.

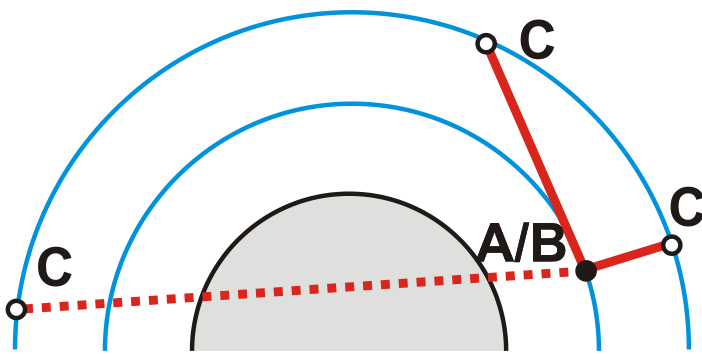


Figure 2-1 Geometry of the baseline between Swarm A/B and Swarm C

Table 2-1 Velocity and velocity errors used for the simplified error analysis

	single satellite	inter-satellite baseline		
		along-track	cross-track	oblique
velocity [m/s]	7700	250	170	15400
accuracy [mm/s]	0.1	0.01	0.01	0.01

Considering the magnitude of baseline velocities, the along-track and cross-track constellations show only moderate values. These constellations are stable in time, i.e., the relative position between the satellites are more or less constant. In the along-track constellation the satellites will approach or depart from each other depending on local gravity field structures. In addition, the cross-track baseline contains the effect of converging orbit arcs, i.e. the satellites get closer as they move towards the poles, while their distance increases as they move towards the equator. Overall, these constellations are stable in time. This is different for the oblique baseline, where the satellites move at different altitudes. Since the lower satellite is faster, the relative position is not constant. Starting, e.g., both satellites at the equator it happens after a while, that they find each other on opposite sides of the globe due to different orbital velocities. After a while, the satellites approach each other again, and this constellation shift repeats periodically. At the start epoch just described, the relative velocity will be quite small, but when being located at opposite sides of the globe, it happens, that the one satellite crosses the equator in an ascending arc with positive velocity component in z-direction, while at the same time, the other satellite crosses the equator in a descending arc with negative velocity component. Then the relative velocity between the two satellites amounts to twice the absolute velocity of one satellite, i.e., to about 15400 m/s. According to equation (2.35), this large relative velocity degrades the accuracy of potential differences, as will be shown further below. First the single-satellite case should be discussed.

Inserting the numbers given in Table 2-1 into equation (2.34) one finds for the expected error of the potential

$$\sigma_V = \dot{x} \sigma_{\dot{x}} \approx 0.77 \text{ m}^2/\text{s}^2$$

Taking just the simple difference between two single satellite solutions, without considering the baseline information between the satellites as is done in equations (2.33) and (2.35), one finds for the potential difference between two arbitrary satellites (assuming the errors of both satellites being independent of each other)

$$\sigma_{V_{12}} = \sqrt{2} \dot{x} \sigma_{\dot{x}} \approx 1.09 \text{ m}^2/\text{s}^2$$

Making use of the baseline information, one has to distinguish between the three different cases listed in Table 2-1, i.e., along-track, cross-track and oblique. For the along-track component one gets

$$\sigma_{V_{12}} = \sqrt{(\dot{x}_{12} + \dot{x}_1)^2 \cdot \sigma_{\dot{x}_{12}}^2 + \dot{x}_{12}^2 \cdot \sigma_{\dot{x}_1}^2} \approx \sqrt{7950^2 \cdot 10^{-10} + 250^2 \cdot 10^{-8}} \approx 0.08 \text{ m}^2/\text{s}^2$$

where the largest contribution comes from the first term, i.e., from the error of the baseline velocity. Since this is assumed one order of magnitude better than the absolute velocity error, also the potential difference can be determined with about one order of magnitude higher accuracy. As long as the baseline velocity is moderate, i.e., for the stable constellations, the result does not change much. Consequently, the same accuracy level of 0.08 m/s can be expected for the cross-track case.

The situation changes as soon as the relative velocity becomes large. This is the case for the oblique component. Then, with increasing relative velocity, the second term in equation (2.35) tends to dominate the error budget. Using the numbers in Table 2-1 (which is a worst case scenario) one gets

$$\sigma_{V_{12}} \approx \sqrt{23100^2 \cdot 10^{-10} + 15400^2 \cdot 10^{-8}} \approx 1.56 \text{ m}^2/\text{s}^2$$

This is about a factor of 20 worse, than the result for the stable along- and cross-track constellations. When performing a global gravity field analysis from potential differences, the recovery will be strongly degraded by epochs with large relative velocities. The result is even worse, than when using the simple difference between two single satellite solutions, though only by a factor of 1.4. Therefore the individual observations need either to be properly weighted according to the relative velocity or one could exclude baselines with large relative velocity. In the latter case, a threshold needs to be defined for the largest acceptable relative velocity. In addition, one could wonder, if, in case of satellites on opposite sides of the globe, it is possible at all to determine the inter-satellite baseline from GPS to the accuracy level assumed until now. In this case, there are no common GPS satellites in view to derive a baseline, but the baseline would have to be determined indirectly by solving for a global network including the LEO satellites. Since the quality of such a baseline is expected to be below the accuracy of a directly observed baseline, such large baselines would degrade the quality of the results even more. Both, the observability of GPS satellites and the relative velocity threshold result in the exclusion of long baselines.

Finally, it should be mentioned, that the along-track constellation is treated in the above error analysis as one with GPS observations only. The satellites fly in a GRACE like constellation, while there is no additional high-accuracy inter-satellite range observation. If one introduces such an observation, one can use the simplified error model

$$\sigma_{V_{12}} = |\dot{x}_1| \sigma_{\dot{\rho}} \quad (2.36)$$

based on the old proposal by Wolff [1969] to transform small velocity differences between two satellites in a tandem constellation into potential differences, i.e. the essence of the energy integral.

2.3 Frequency analysis

The model was never rigorously applied to real data due to residual cross-track effects, but it is well suitable for error propagation (see e.g. Han [2004]). Here the error of the potential difference depends only on the rang-rate error $\sigma_{\dot{\rho}}$ which is scaled by the satellite speed, i.e., by about 7600 m/s. Using a rang-rate accuracy of about $1 \cdot 10^{-7}$ m/s one finds

$$\sigma_{V_{12}} = 0.0008 \text{ m}^2/\text{s}^2 \quad (2.37)$$

which is about a factor of 100 better than the GPS-only solution.

2.3.Frequency analysis

In this section several terms used in the frequency analysis of the time-variable gravity signals will be briefly introduced.

Fourier transform

Fourier transform originates from Fourier series. In general, a continuous periodic function of time $x(t)$ with a period of T can be developed into a sum of sines and cosines functions. This expression is then called Fourier series and has the general form like below

$$x(t) = \frac{a_0}{2} + \sum_{k=1}^{\infty} [a_k \cos(k\omega_0 t) + b_k \sin(k\omega_0 t)] \quad (2.38)$$

with

$$\omega_0 = 2\pi/T$$

$$a_k = \frac{2}{T} \int_0^T x(t) \cos(k\omega_0 t) dt$$

$$b_k = \frac{2}{T} \int_0^T x(t) \sin(k\omega_0 t) dt$$

Each term of the Fourier series corresponds to a certain frequency (or wavelength) and the signal strength of this frequency is described by a_k and b_k . Fourier series can be written in terms of amplitude and phase or in complex form as well. Detailed formulas about Fourier series can be found e.g. in Strang [1986] or Meyer [2005].

The Fourier Transform transforms a function $x(t)$ from the time domain to its frequency domain. The representation of the original function in its frequency domain describes which frequencies are present in the original function. The work in this section is presented in greater details in Briggs [1995], Gray and Goodman [1995], Walker [1991] or Meyer [2005].

The continuous Fourier transform $X(f)$ of the function $x(t)$ is defined as

$$X(f) = \int_{-\infty}^{\infty} x(t)e^{-i2\pi ft} dt \quad (2.39)$$

Where t is time and f is frequency. The units are seconds and Hz, respectively. The inverse Fourier transform is then given by

$$x(t) = \int_{-\infty}^{\infty} X(f)e^{i2\pi ft} df \quad (2.40)$$

which transforms the function $X(f)$ in spectral domain into time domain $x(t)$. Equation (2.39) and (2.40) hold only for continuous signal. In reality, however, most of the data sets are measured at consecutive epochs and they are therefore not continuous time series but discrete values sampled at measuring points. For these signals, the equations given above cannot be implemented directly.

The transform for discrete and periodic signal is called Discrete Fourier Transform (DFT). Assume the continuous function $x(t)$ is sampled at the discrete epochs

$$t_n = n\Delta t, n = 0, 1, 2, \dots, N-1 \quad (2.41)$$

The sampled discrete function $x[n]$ will have N samples in an interval of Δt with a period of $T = N \cdot \Delta t$. The discrete Fourier transform $X[l]$ is then given by

$$X[l] = \sum_{n=0}^{N-1} x[n]e^{-i2\pi ln/N}, l = 0, 1, 2, \dots, N-1 \quad (2.42)$$

with the frequency sampling rate defined by

$$\Delta f = \frac{1}{T} = \frac{1}{N\Delta t} \quad (2.43)$$

The frequency spectrum ranges from 0 to $f = 1/(2\Delta t)$, which is defined by the Nyquist theorem. Note that $x[n]$ is discrete and assumed to be periodic. As a consequence, $X[l]$ is periodic and discrete. The Inverse Discrete Fourier Transform (IDFT) is given by

$$x[n] = \frac{1}{N} \sum_{l=0}^{N-1} X[l]e^{i2\pi ln/N}, n = 0, 1, 2, \dots, N-1 \quad (2.44)$$

A 24-month-hydrology data set from the LaD (Land Dynamic model) with a monthly resolution can be taken as an example to explain the equations above. The same data set is also used in the simulation studies in Chapter 4. In this dissertation the terms cpa (cycles per year) and cpd (cycles per day) are often used in spectral analysis, where 1 cpd equals 365 cpa. As shown in equations (2.42) and (2.43), the DFT of this data set will give a spectrum from 0 to 6 cpa in a frequency interval of 0.5 cpa. Similarly, a one-year atmosphere-ocean data with a 6-hourly resolution will have a spectrum from 0 to 730 cpa in an interval of 1 cpa.

Different algorithms have been developed to accelerate the DFT calculation process and to increase the computation efficiency. One of the methods is called the Fast Fourier Transform (FFT). The algorithm behind FFT and the realization in programming languages can be found in the literature, e.g. in [Meyer, 2005].

Sampling theory and aliasing

The discretization of a continuous time series is called sampling. In signal processing, sampling corresponds to a multiplication of a continuous signal with a Dirac pulse train. The sampled signal, which is discrete, leads to a periodic spectrum when transformed. The discrete data set is a sampled signal with certain sampling frequency of the originally continuous signal, as shown in equation (2.41) and (2.43). It is known as the Nyquist Theorem (also called sampling theorem) that a continuous signal can only be perfectly reconstructed from its discrete sample, if the sampling frequency is higher than two times the highest frequency in the original signal. If this condition is not fulfilled, the reconstruction of the continuous signal will suffer from the so-called aliasing effect because of the insufficient sampling rate. The aliasing problem can be explained with help of Figure 2-2, where the aim is to recover the mean value of a signal over a certain time span. Here the black line represents the true signal and the blue dots are the sampling epochs. The dashed black line represents the true mean of the signal and the dashed blue line shows the estimated mean, as determined by the data samples. There is a clear difference between the true mean and the estimated mean caused by the under sampling of the data, which is referred to as aliasing error.

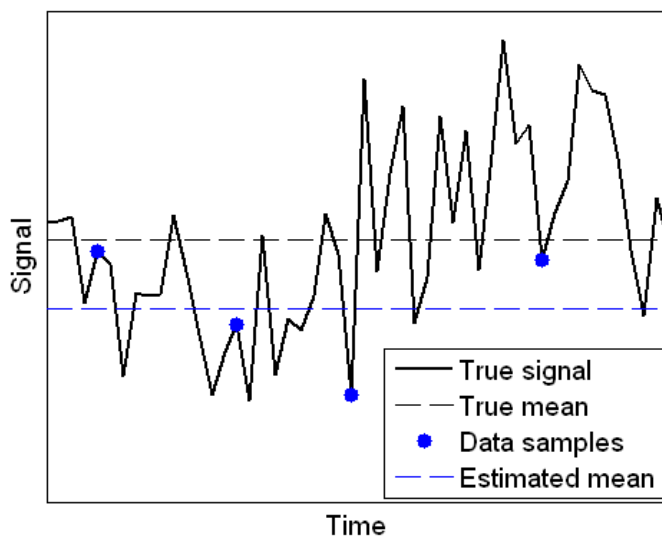


Figure 2-2 Illustration of temporal aliasing error (based on Loomis [2009])

In the field of satellite gravimetry, the sampling condition is unfortunately not always fulfilled. The situation is complicated: the discrete measurements along the orbit represent a one dimensional series, from which a field function is to be reconstructed that varies in space (on the globe) and in time. Thus two types of aliasing can happen in the case of satellite gravity missions, namely temporal or spatial aliasing because of insufficient temporal or spatial sampling, respectively. For instance, it is not possible to perfectly reconstruct a time variable signal whose period is equal or higher than the half of the satellite observation period. A similar principle holds for the spatial aliasing. For a gravity signal limited in a certain region with a certain spatial size, it is only possible to perfectly reconstruct the signal, if the spatial resolution of the satellite fulfils the sampling requirements for this region.

Theoretically, aliasing can be reduced by increasing the sampling so as to meet the Nyquist Theorem. Reubelt *et al.* [2010] have investigated the temporal/spatial aliasing issue by simulating satellite constellations with repeat orbits. Sticking to a repeat orbit has the advantage, that it is easy to interpret the time resolution by its repeat period. A β/α repeat orbit completes β revolutions in α nodal days, where β and α are integers. The repeat period of such orbit is α nodal days with a revolution time T_{rev}

= α / β nodal days. The minimum spatial and temporal resolution for a single satellite can be then determined as $D_{\text{space}} = 2\pi / \beta$ [rad] and $D_{\text{time}} = \alpha$ [nodal day]. In this case it holds

$$D_{\text{space}} \times D_{\text{time}} = 2\pi\alpha / \beta = 2\pi T_{\text{rev}} \quad (2.45)$$

For a low-Earth orbiting satellite, the revolution time T_{rev} is varying only marginally with its orbit height. Thus $2\pi T_{\text{rev}}$ can be regarded as a constant for a given orbit height, which indicates that the increasing of temporal sampling will decrease the spatial sampling and vice versa. Without compromising the temporal sampling, the spatial sampling can be improved e.g. by having additional satellites on interleaved ground tracks with a longitudinal shift. Similarly, without decreasing the spatial sampling, the temporal resolution can be improved e.g. by having additional satellites on the same ground track with a time shift. In Reubelt's 4-day- simulation, they attempted to recover the fast changing atmosphere-ocean signal, where both temporal and spatial aliasing occurs. Their results demonstrated that with appropriate constellations, it is possible to increase both space and time sampling and thus reduce the aliasing error significantly.

In this dissertation the discussions about the aliasing issue will be given in section 4.4. Since the energy integral method is implemented in the simulation studies, specific aspects of the aliasing issue regarding the non-conservativeness of the time-variable gravity signals are discussed as well.

Filtering of spherical harmonics coefficients

According to Kaula [1966], the signal strength of the gravity field as expressed in spherical harmonics decreases with increasing degree and order, while the errors of the coefficients increase as the degree and order gets larger. This can lead to highly inaccurate results as the errors from the poorly determined terms with higher degree and orders may contaminate the well-determined terms with lower degrees. A common way to avoid this effect is to use filters. The filters act as a multiplication factor to the coefficients in the spectral domain, or equivalently, as a convolution in the space domain. Depending on the property one can distinguish isotropic from non-isotropic filters. While the latter is azimuth dependent as well, the former one is only dependent on spherical distance.

The easiest isotropic filter is a direct truncation of the spherical harmonic series at a certain degree n_{max} so that the inaccurate coefficients with higher degree are not included by setting all degrees greater than n_{max} to 0. This is equivalent to a low-pass filter or a step function in the domain of spherical harmonics given by

$$W_n = \begin{cases} 1, & \text{for } 0 \leq n \leq n_{\text{max}} \\ 0, & \text{for } n_{\text{max}} < n \end{cases} \quad (2.46)$$

In space domain function (2.46) corresponds to a sinc function. The disadvantage of this filter is that during the convolution in space domain, due to the oscillations and side-lobes introduced by the sinc function, signal from faraway regions will affect the signal from the region of interest. This effect is also referred to as spatial leakage, i.e. unwanted signal content "leaks" into the desired signal.

A better choice among the isotropic filters is the Gauß-filter (Jekeli [1981], Wahr *et al.* [1998]), which is given by

$$W(\alpha) = \frac{b}{2\pi} \cdot \frac{e^{-b(1-\cos\alpha)}}{1 - e^{-2b}} \quad (2.47)$$

with

2.3 Frequency analysis

$$b = \frac{\ln 2}{1 - \cos \psi} \quad \text{and} \quad \psi = \frac{r}{R} \quad (2.48)$$

Here r stands for the radius of the Gauß-filter and R for the radius of the Earth. α is the angle between two points with a distance of $\alpha \cdot R$ on the Earth's surface. In the spectral domain the weighting factor W_n can be calculated recursively through

$$W_0 = 1, \quad W_1 = \frac{1 + e^{-2b}}{1 - e^{-2b}} - \frac{1}{b}, \quad W_n = -\frac{2n-1}{b} W_{n-1} + W_{n-2} \quad (2.49)$$

The Gauß-filter corresponds to a Gauß-function in space domain, which does not show side-lobes and oscillations and thus can be used to avoid the above mentioned problem introduced by the low-pass filter.

Peters [2007] has compared four kinds of isotropic filters, namely low-pass, Gauß, Pellinen and Hann, where he analyzed the differences and the similarities of these filters. Among the isotropic filters, the Gauß-filter is the most widely used one, which can be often found in the processing and interpreting of the GRACE monthly solutions for geophysical studies (Wahr *et al.* [2006]).

If the error structure is not only dependent of degree but also of the order, the above mentioned isotropic filters are not suitable anymore. For example, the well-known North-South stripe pattern from the GRACE solution is reported to be related to the correlation between the spherical harmonics coefficients (Swenson and Wahr [2006]). A strong correlation between coefficients of the order 15 to 18 was found and a correlated-error filter was implemented to minimize such correlations. Combined with a Gauß-filter, such filters were reported to be able to minimize the stripe pattern without eliminating large part of the signal itself.

In this dissertation the non-isotropic filter is not considered. In section 4.5, where attempt is made to recover the hydrology signal with GPS-only solutions to degree and order 6, the direct truncation filter is implemented to cut off all the coefficients from degree 7 to 30. Due to the very low cut-off degree (degree 6) the truncation filter should be good enough to exclude the errors introduced by the poorly determined coefficients with higher degrees (Wahr *et al.* [1998]).

3. Time-variable gravity signal analysis

3.1. Relation between mass and spherical harmonics

Leaving aside the measuring principle and constellation for the moment, the final products of current satellite gravity missions (e.g. CHAMP, GRACE, GOCE) are sets of spherical harmonic coefficients to a certain maximum degree and order. For example, GRACE level-2 gravity products consist of complete sets of harmonics to a maximum degree of 120, averaged over monthly intervals. Spherical harmonic coefficients can be used to generate geoid, gravity, or mass solutions. For most applications the gravity field itself might not be of direct interest. Instead it is usually the mass distribution causing the gravity field that is of more interest. To determine the mass distribution, one needs to know how to relate the coefficients to mass changes, which will be described in the following.

For GRACE, the time-variable component of the gravity field is obtained by removing the long-term mean value of the monthly solutions. The mean value can be simply determined by constructing the average of all the monthly fields one wishes to use for the analysis. The reason to remove the mean field is that it is included in the static field, while one is interested usually more in the change of density distribution of the surface of the Earth, e.g. the hydrology or ocean circulation.

The geoid height can be expressed in equation (3.1) (Chao and Gross [1987]) as

$$N(\theta, \phi) = R \sum_{n=0}^{\infty} \sum_{m=0}^n \bar{P}_{nm}(\cos \theta) (C_{nm} \cos(m\lambda) + S_{nm} \sin(m\lambda)) \quad (3.1)$$

where R is the radius of the Earth, θ and λ are co-latitude and east longitude, C_{nm} and S_{nm} are dimensionless coefficients, and \bar{P}_{nm} are normalized associated Legendre functions:

$$\bar{P}_{nm}(x) = \sqrt{(2 - \delta_{m0})(2n+1)} \frac{(n-m)!}{(n+m)!} \times \frac{(1-x^2)^{\frac{m}{2}}}{2^n n!} \frac{d^{n+m}}{dx^{n+m}} (x^2-1)^n \quad (3.2)$$

Detailed descriptions about Legendre polynomials can be found in e.g. in Heiskanen and Moritz [1967]. Now suppose there is a time-dependent change in the geoid ΔN , which can be presented in terms of ΔC_{nm} and ΔS_{nm} as:

$$\Delta N(\theta, \phi) = R \sum_{n=0}^{\infty} \sum_{m=0}^n \bar{P}_{nm}(\cos \theta) (\Delta C_{nm} \cos(m\lambda) + \Delta S_{nm} \sin(m\lambda)) \quad (3.3)$$

Let $\Delta\rho(r, \theta, \lambda)$ be the density change that causes this geoid change, one can derive the following (Wahr *et al.* [1998]):

$$\begin{Bmatrix} \Delta C_{nm} \\ \Delta S_{nm} \end{Bmatrix} = \frac{3}{4\pi R \rho_{ave} (2n+1)} \iiint \Delta\rho(r, \theta, \lambda) \bar{P}_{nm}(\cos \theta) \times \left(\frac{r}{R}\right)^{n+2} \begin{Bmatrix} \cos(m\lambda) \\ \sin(m\lambda) \end{Bmatrix} \sin \theta d\theta d\lambda dr \quad (3.4)$$

where ρ_{ave} is the average density of the Earth (5517 kg/m³).

3.1 Relation between mass and spherical harmonics

One can further define the change of surface density, i.e. the change of mass/area $\Delta\sigma$, as the radial integral of $\Delta\rho(r, \theta, \lambda)$ through a thin layer of thickness H at the Earth's surface

$$\Delta\sigma(\theta, \lambda) = \int_H \Delta\rho(r, \theta, \lambda) dr \approx \Delta\rho \cdot dr \quad (3.5)$$

Suppose this layer includes the atmosphere, ocean, ice and below-ground water storage and it is thin enough so that

$$(n_{\max} + 2)H / R \ll 1 \quad (3.6)$$

With $(\frac{r}{R})^{l+2} \approx 1$, (3.4) reduces to

$$\begin{Bmatrix} \Delta C_{nm} \\ \Delta S_{nm} \end{Bmatrix}_{surfmass} = \frac{3}{4\pi R \rho_{ave} (2n+1)} \iint \Delta\sigma(\theta, \lambda) \times \bar{P}_{nm}(\cos\theta) \begin{Bmatrix} \cos(m\lambda) \\ \sin(m\lambda) \end{Bmatrix} \sin\theta d\theta d\lambda \quad (3.7)$$

Equation (3.7) describes the contribution to the geoid due to direct redistribution of the surface mass. This change also loads and deforms the underlying solid Earth, which causes an additional geoid contribution. This contribution is typically a few percent of the gravity change caused by the surface mass change and it can be represented as

$$\begin{Bmatrix} \Delta C_{nm} \\ \Delta S_{nm} \end{Bmatrix}_{solidEarth} = \frac{3k_n}{4\pi R \rho_{ave} (2n+1)} \iint \Delta\sigma(\theta, \lambda) \times \bar{P}_{nm}(\cos\theta) \begin{Bmatrix} \cos(m\lambda) \\ \sin(m\lambda) \end{Bmatrix} \sin\theta d\theta d\lambda \quad (3.8)$$

$$\text{Or } \begin{Bmatrix} \Delta C_{nm} \\ \Delta S_{nm} \end{Bmatrix}_{solidEarth} = k_n \begin{Bmatrix} \Delta C_{nm} \\ \Delta S_{nm} \end{Bmatrix}_{surfmass} \quad (3.9)$$

Where k_n is the load Love number of degree n (Farrel [1972], Chao [1994]). The total geoid change is the sum of equation (3.7) and (3.8):

$$\begin{Bmatrix} \Delta C_{nm} \\ \Delta S_{nm} \end{Bmatrix} = \begin{Bmatrix} \Delta C_{nm} \\ \Delta S_{nm} \end{Bmatrix}_{surfmass} + \begin{Bmatrix} \Delta C_{nm} \\ \Delta S_{nm} \end{Bmatrix}_{solidEarth} \quad (3.10)$$

Or

$$\begin{Bmatrix} \Delta C_{nm} \\ \Delta S_{nm} \end{Bmatrix} = \frac{3}{4\pi R \rho_{ave} (2n+1)} \iint \Delta\sigma(\theta, \lambda) \times \bar{P}_{nm}(\cos\theta) \begin{Bmatrix} \cos(m\lambda) \\ \sin(m\lambda) \end{Bmatrix} \sin\theta d\theta d\lambda \quad (3.11)$$

One can also inversely derive

$$\Delta\sigma(\theta, \lambda) = \frac{R \rho_{ave}}{3} \sum_{n=0}^{\infty} \sum_{m=0}^n \frac{2n+1}{1+k_n} \bar{P}_{nm}(\cos\theta) (\Delta C_{nm} \cos(m\lambda) + \Delta S_{nm} \sin(m\lambda)) \quad (3.12)$$

which can be used to determine the change in surface mass density from ΔC_{nm} and ΔS_{nm} .

Inserting (3.11) into (3.3) one gets the change of geoid from the change in surface mass density via

$$\Delta N(\theta, \lambda) = \frac{3R\rho_w}{\rho_{ave}} \sum_{n=0}^{\infty} \sum_{m=0}^n \bar{P}_{nm}(\cos \theta) \frac{1+k_n}{(2n+1)} (\Delta \tilde{C}_{nm} \cos(m\lambda) + \Delta \tilde{S}_{nm} \sin(m\lambda)) \quad (3.13)$$

where ρ_w is the density of water (1000 kg/m³) and $\Delta \tilde{C}_{nm}, \Delta \tilde{S}_{nm}$ are dimensionless coefficients with no direct physical meanings. They are related to ΔC_{nm} and ΔS_{nm} via

$$\begin{Bmatrix} \Delta \tilde{C}_{nm} \\ \Delta \tilde{S}_{nm} \end{Bmatrix} = \frac{\rho_{ave}}{3\rho_w} \frac{(2n+1)}{1+k_n} \begin{Bmatrix} \Delta C_{nm} \\ \Delta S_{nm} \end{Bmatrix} \quad (3.14)$$

Or inversely

$$\begin{Bmatrix} \Delta C_{nm} \\ \Delta S_{nm} \end{Bmatrix} = \frac{3\rho_w}{\rho_{ave}} \frac{1+k_n}{(2n+1)} \begin{Bmatrix} \Delta \tilde{C}_{nm} \\ \Delta \tilde{S}_{nm} \end{Bmatrix} \quad (3.15)$$

The above results assume that the surface layer is thin enough that equation (3.6) is valid. Assume $n_{\max} = 70$, and the layer including atmosphere, which means $H \approx 10$ km, then the above relation is violated at about 11%. This is a large enough inaccuracy for some applications, e.g. the atmospheric density fluctuation studies. In contrast the mass variations in the ocean and water stored on land occur mostly entirely within 1 km, and for them equation (3.6) is accurate to about 1%, which is good enough for research studies on continental hydrology or the ocean. In fact, the single layer assumption should hold up to about degree and order 100 for hydrological or oceanographic applications (Flechtner [2007]). The hydrology recovery simulations in Chapter 4 will be carried out to degree and order 30, thus the single layer assumption is good enough for such experiments.

Errors in the estimate of surface mass change are either from the computation of the spherical harmonic coefficients or from the leakage from other signals. Here one concentrates only on the errors of the coefficients themselves. These errors can be caused by instruments, data processing, aliasing errors and other error sources. In this dissertation only the instrument and aliasing errors are discussed with simulations. As mentioned in section 2.3, aliasing errors are caused by under sampling in either time or space or both and can therefore be divided into temporal aliasing or spatial aliasing. Temporal aliasing has been a greater issue for GRACE, where the under sampled short-period signal (sub-monthly) aliases into the monthly solution. Aliasing effects can be reduced by the increased sampling rate in space or/and time. If this is not possible, they can still be reduced by modelling the short-period signals independently and remove their contribution before conducting the monthly solution. This process is called de-aliasing process. For GRACE that means modelling and removing the effects of solid Earth and ocean tides (e.g. with EOT08a, Savcenko *et al.* [2008, 2010]), atmospheric mass variations over land (e.g. with ECMWF, Flechtner [2007]) and non-tidal short period ocean bottom pressure (e.g. with OMCT, Flechtner [2007]). Any difference between the real signals and the models will remain in the GRACE solution, which is referred as de-aliasing error.

3.2. Continental hydrology

Introduction to the global water cycle

The hydrology cycle (also called water cycle) describes the continuous movement of water on, above, and below the surface of the Earth (Figure 3-1). Two major factors are responsible for the global water cycle: the Sun as the main driving factor, and gravity, which makes water to flow and to circulate. One may start the description with the ocean, where water is heated by the Sun and evaporates as vapour into the air. The water vapour in the air also contains contributions from the ice and snow on the ground, which can sublime directly into water vapour without melting into liquid water. The vapour is then taken by the rising air circulations to an upper level of the air, where cooler temperatures cause it to condense into clouds and partly to return as rain. These clouds are moved by the air circulations around the globe. The clouds collide, grow, and fall from the sky as precipitation. Some precipitation falls as snow and can accumulate as ice caps and glaciers, but most precipitation falls back into the oceans or onto land as rain. The precipitation on land flows over the ground as surface runoff. A portion of the runoff enters rivers in valleys in the landscape, moving towards the oceans. Another portion of runoff is accumulated and stored in lakes as freshwater. The rest of runoff soaks into the ground as infiltration. Some water infiltrates deeply into the ground and replenishes aquifers (saturated subsurface rock), some infiltration stays close to the land surface and can seep back into surface-water bodies as ground-water discharge and some ground water finds openings in the land surface and emerges as freshwater springs. Over time, the water cycle keeps moving and transports mass between atmosphere, ocean and the land.

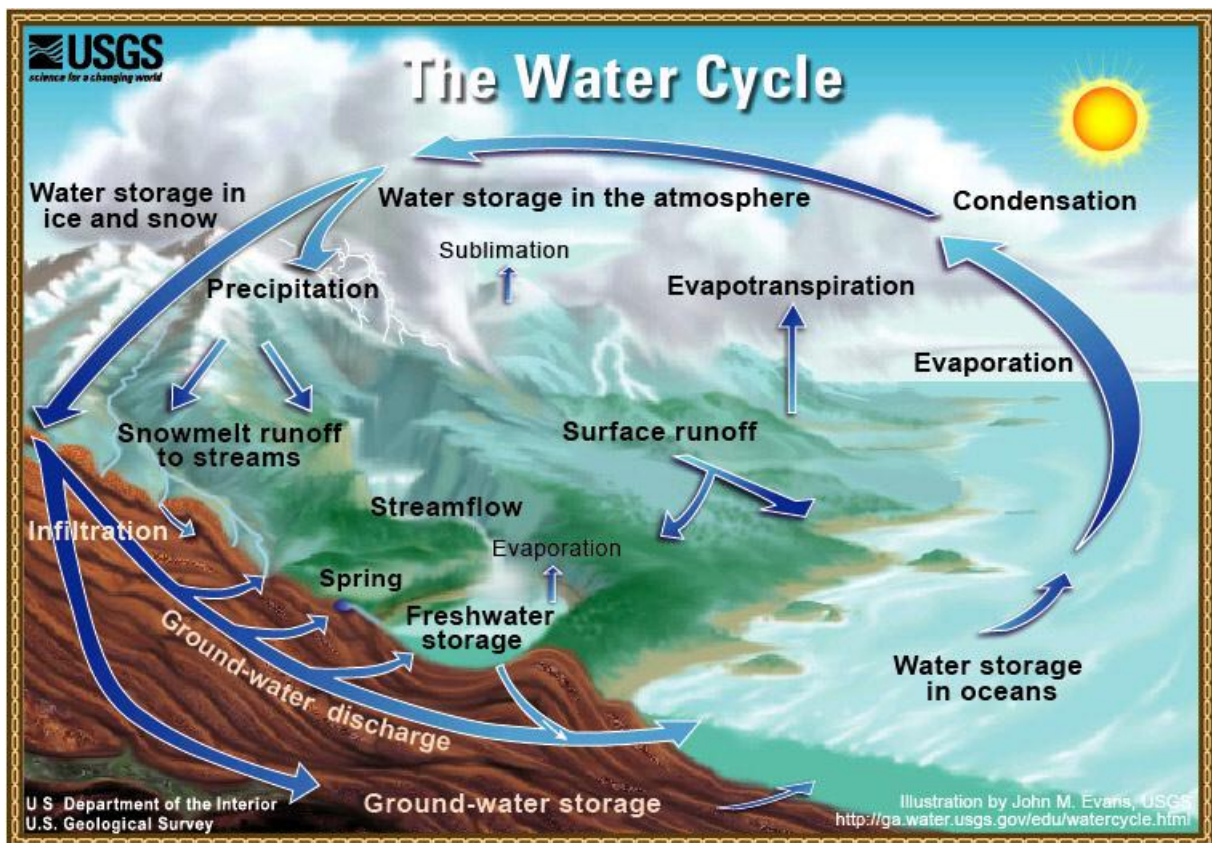


Figure 3-1 The hydrology cycle (<http://ga.water.usgs.gov/edu/watercycle.html>)

Table 3-1 represents the global water balance. As one can see the oceans contain nearly 97% of all water on the Earth, while the ice caps and glaciers store about 69% of the fresh water. The remaining fresh water is stored mainly in groundwater. The oceans, glaciers and groundwater together take about 99.94% of the whole water storage on the Earth, while the remaining 0.06% are distributed in soil, lakes, rivers and atmosphere.

Table 3-1 Global water balance (Gruber *et al.* [2009])

Water source	Water volume, in cubic miles	Water volume, in cubic kilometers	Percent of freshwater	Percent of total water
Oceans, Seas, & Bays	321,000,000	1,338,000,000	--	96.5
Ice caps, Glaciers, & Permanent Snow	5,773,000	24,064,000	68.7	1.74
Groundwater	5,614,000	23,400,000	--	1.7
Fresh	2,526,000	10,530,000	30.1	0.76
Saline	3,088,000	12,870,000	--	0.94
Soil Moisture	3,959	16,500	0.05	0.001
Ground Ice & Permafrost	71,970	300,000	0.86	0.022
Lakes	42,320	176,400	--	0.013
Fresh	21,830	91,000	0.26	0.007
Saline	20,490	85,400	--	0.006
Atmosphere	3,095	12,900	0.04	0.001
Swamp Water	2,752	11,470	0.03	0.0008
Rivers	509	2,120	0.006	0.0002
Biological Water	269	1,120	0.003	0.0001
Total	332,500,000	1,386,000,000	-	100

Spectral analysis of the hydrology signal

The classical approach is to model the water flow based on run-off or precipitation data. However, a mission like GRACE is able to measure the hydrological mass redistribution from satellite. The GRACE solutions, provided by research institutes such as GFZ, CSR or CNES (see abbreviations), can be used to estimate the hydrological variations (Wahr *et al.* [1998, 2004], Tapley *et al.* [2004 b]). Zenner [2006] has compared and demonstrated the differences in GRACE solutions from GFZ, CSR and CNES. More analysis and comparisons of the GRACE solutions from different institutions can also be found e.g. in Qiu [2008] or Peters [2007]. These differences are so far still not clearly explained and it is therefore difficult to choose one from all these solution to compute the continental hydrology signal. Besides this uncertainty, the GRACE solutions do not only contain temporal gravity signals but also errors from diverse sources, e.g. instrument noise or the imperfection of the de-aliasing product, which should be taken care of if one is only interested in the hydrology signal contained in such solutions. Therefore, instead of using the real GRACE data, the hydrology model LaD (Land Dynamic model) is used to represent the time-variable hydrology signal in this dissertation.

The LaD model is processed and distributed by the Geophysical Fluid Dynamics Lab (GFDL) from the National Oceanic and Atmospheric Administration (NOAA). This model considers the surface density for snow (q_s), ground water (q_{GW}) and surface water (q_w) in monthly resolution on a $1^\circ \times 1^\circ$ grid. The total hydrology effect can be determined then by the summation (Milly *et al.* [2002])

$$q = q_s + q_{GW} + q_w \quad (3.16)$$

The surface density q has the unit $[\text{kg}/\text{m}^2]$. Since in many applications not the surface density but the term “equivalent water height” is used, one can convert between the two units via

$$q(\theta, \lambda) = \rho_w * h_w(\theta, \lambda) = \frac{p(\theta, \lambda)}{g} \quad (3.17)$$

where ρ_w is the density of water $[1000 \text{ kg}/\text{m}^3]$, $p(\theta, \lambda)$ is the surface pressure $[\text{kg}/\text{ms}^2]$, g is the mean gravity acceleration $[\text{m}/\text{s}^2]$, $q(\theta, \lambda)$ is the surface density $[\text{kg}/\text{m}^2]$ and h_w is the equivalent water height.

3.2 Continental hydrology

The LaD model used here provides the surface density q for 29 months from January 2003 to May 2005. For each month the mean value over the 29 months is subtracted. The remaining is the variation of the surface density for each month, which will be used to compute the corresponding spherical harmonics coefficients according to equation (3.11) shown in section 3.1.

Here in this dissertation the data section from 01.2003 to 01.2005 is used. Figure 3-2 shows the month January of 2003 in geoid height in [mm]. The signal strength ranges from about -4 mm to 7 mm with a RMS of about 1 mm.

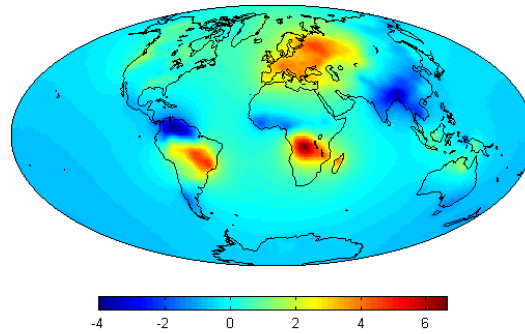


Figure 3-2 Hydrology geoid for 01.2003 in [mm], max = 6.6, min = -4.06, mean = 0.02, RMS = 1.02

A Fourier transform is applied to the selected coefficients of the 24-month LaD data, as described in section 2.3. The purpose is to find the structure of the spectrum and the most dominant frequencies.

Figure 3-3 shows the results of such an analysis in degree RMS plot. Panel a) is processed to degree and order 180 and panel b) to 30. From panel a) one can see that the signal concentrates on lower degrees. Above degree 30 the signal strength decreases significantly and above about degree 70 there is almost no signal observable. From panel b) it is obvious to see that the most dominant signals are the 1 cpa and 2 cpa components, which correspond to annual and semi-annual variations, respectively. The highest frequency from this Fourier analysis, which is determined by the Nyquist theorem, is 6 cpa, i.e. a 2-monthly frequency. The signal strength of the 6 cpa component is quite weak compared with the dominant frequencies. Over all this analysis indicates that the LaD model contains mainly low-frequency components up to a maximum of 6 cpa. Sub-monthly signal component is not included in this model.

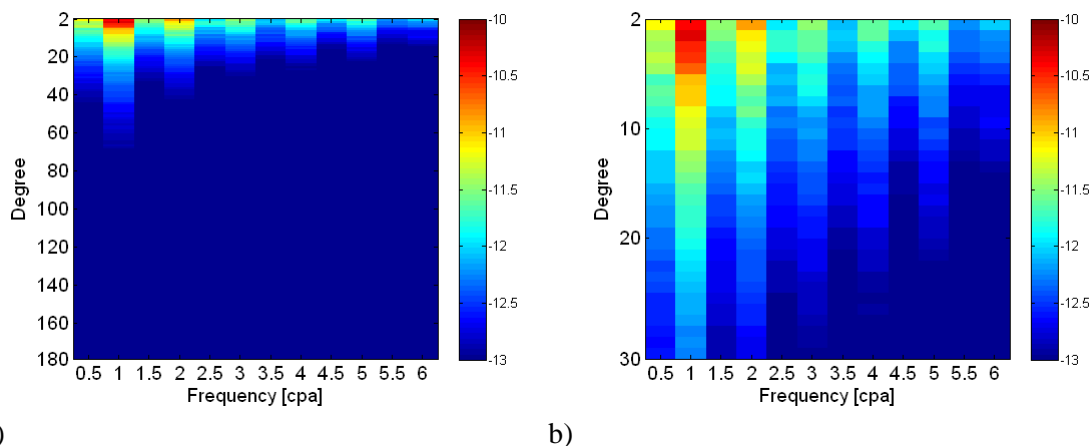


Figure 3-3 Degree RMS for LaD model over 24 months, up to degree 180 (a) and degree 30 (b)

In order to see if the hydrology signal also contains high frequency components, other models with sub-monthly resolution should be analysed. The GLDAS (Global Land Data Assimilation System, Rodell *et al.* [2004]) model, for example, is given in daily resolution, which makes it possible to analyse the signal component up to 0.5 cpd. Peters [2007] has analysed this model with the above mentioned Fourier transform and has found that there is no significant high frequency component. In fact, due to insufficient global observation data with sub-monthly resolution it is so far not clear, how much the frequency components above 6 cpa reflect the real hydrology mass change, because there are only few observations assimilated in the hydrology models. As a consequence, this dissertation will focus on 1 cpa and 2 cpa components, namely annual and semi-annual components of the hydrology signal. Simulations studies in section 4.5 will make an attempt to recovery such components with satellite constellations.

For simulation purposes, the hydrology data is processed in two different ways, depending on the simulation scenarios. It is linearly interpolated into 6-hour intervals to be consistent with the 6-hourly atmosphere and ocean data when doing the static field simulation in section 4.3 as well as for the aliasing discussion in section 4.4.1. The original data with monthly resolution is used in the hydrology recovery simulation in section 4.5.

3.3. Atmosphere and ocean

The atmosphere is one of the main contributors to mass variations in the Earth system. Atmospheric mass variations are present for frequencies ranging from a few hours to decadal periods (van Dam *et al.* [2008]). The flow of the atmosphere determines the distribution and propagation of the pressure systems around the globe. Several national meteorological services develop global atmospheric models in order to perform weather predictions for the area of interest. Two well-known global atmospheric models are ECMWF (European Centre for Medium-Range Weather Forecasts) and NCEP (US National Centre for Environmental Prediction), which are named after the institutes where the models are produced. Both models are given in 6-hourly resolution. The GFZ (GeoForschungsZentrum) regularly extracts operational analysis data at the ECMWF Integrated Forecast System (IFS) at synoptic times 0:00, 6:00, 12:00 and 18:00, in order to produce the de-aliasing product for GRACE (<http://www.ecmwf.int/research/ifsdocs/index.html>). In this dissertation the ECMWF model is used to represent the atmospheric signal.

In principle there are two methods of computing the spherical harmonic coefficients from the atmospheric mass variations: the first one is the so-called ‘surface pressure’ approach, the second one the ‘vertical integration’ (VI) approach. In the first approach, surface pressure data can be easily transformed into gravity harmonics by spherical harmonic analysis with integration and by applying specific factors for re-scaling the spherical harmonic coefficients. This simple approach is, however, not accurate enough for some high precision applications. Investigations have shown that the vertical structure of the atmosphere has to be taken into account, in order to reach the highest achievable accuracy. Therefore the vertical integration approach is used in the standard GRACE data. For the VI approach, the following input parameters are needed for the determination of the atmospheric potential (Zenner *et al.* [2010]): the point values of surface pressure P_s , the geopotential height H_s , the point values of temperature T and the specific humidity S at all 91 levels of the atmospheric model at different time steps (e.g. 6 hours). Below the major computation steps are shown. For detailed computation steps one refers to Flechtner [2007].

3.3 Atmosphere and ocean

The pressure at half-levels $P_{k+1/2}$ can be computed via

$$P_{k+1/2} = a_{k+1/2} + b_{k+1/2} P_s \quad (3.18)$$

where $a_{k+1/2}$ and $b_{k+1/2}$ are the model dependent coefficients, P_s is the surface pressure. The virtual temperature T_v can be computed by

$$T_v = (1 + 0.608S)T \quad (3.19)$$

where T is the full-level temperature and S is the full-level specific humidity defined at multi-levels k . Based on $P_{k+1/2}$ and T_v , the geopotential height at half-levels $H_{k+1/2}$ can be computed as

$$H_{k+1/2} = H_s + \sum_{j=k+1}^{k_{\max}} \frac{RT_v}{g} \ln \left(\frac{P_{j+1/2}}{P_{j-1/2}} \right) \quad (3.20)$$

where H_s is the surface geopotential height at full-levels, R is the gas constant for dry air and g is the mean gravity acceleration. With $H_{k+1/2}$ the gravity coefficients can be determined by

$$\begin{aligned} C_{nm} &= -\frac{a^2(1+k_n)}{(2n+1)Mg} \iint_{\text{Earth}} \left[\int_{P_s}^0 \left(\frac{a}{a-H_{k+1/2}} + \frac{\xi}{a} \right)^{n+4} dP \right] P_{nm}(\cos\theta) \cos m\lambda \sin\theta d\theta d\lambda \\ S_{nm} &= -\frac{a^2(1+k_n)}{(2n+1)Mg} \iint_{\text{Earth}} \left[\int_{P_s}^0 \left(\frac{a}{a-H_{k+1/2}} + \frac{\xi}{a} \right)^{n+4} dP \right] P_{nm}(\cos\theta) \sin m\lambda \sin\theta d\theta d\lambda \end{aligned} \quad (3.21)$$

With:

M - the mass of the Earth

k_n - love number

ξ - the height of the mean geoid above the mean ellipsoid

a - radius of sphere

P_{nm} - associated Legendre polynomials (normalized)

(r, θ, λ) - spherical coordinates of mass element

Oceanic mass redistributions are driven by periodic changes in the relative position of the Earth, the moon and the sun. They are also driven by the atmosphere (pressure, winds etc). Usually the oceanic effect is divided into two classes: barotropic and baroclinic. The term barotropic refers to a state of the ocean in which pressure levels and density levels coincide and the flow is driven by pressure variations and winds. Here the whole water column has a single density (Gruber *et al.* [2009]). In the baroclinic oceanic response, density is dependent not only on pressure but also on temperature. It includes the vertical density changes and requires additional forcing to handle the thermodynamic effects (Flechtner [2007]). Here pressure levels do not coincide with density levels. Generally speaking, barotropic motions are fast and they can occur from fraction of a day to a few weeks. Ocean tides are good examples for the barotropic effects. The baroclinic motions are slower and they take weeks to centuries. The El Nino effect is a good example for baroclinic motions. In this dissertation the baroclinic ocean model OMCT (Ocean Model for Circulation and Tides) is used, which originates from the HOPE model (Hamburg Ocean Primitive Equation) and has been adjusted to the weather timescale. The OMCT model allows the calculation of ephemeral tides and the wind- and pressure driven circulation. It also allows computing of the secondary effects arising from loading and self-attraction of the water column as well as nonlinear interactions between circulation and tidal induced ocean dynamics (Flechtner [2007]). The OMCT is used to derive the GRACE de-aliasing product for

non tidal short-term variations from the ocean. Since tidal induced oceanic mass redistributions and corresponding gravity effects are removed from GRACE measurements by means of another algorithm, the OMCT does not take ocean tides into account. Details concerning the applied model equations, numerical implementations, parameterizations and the derivation of gravity coefficients can be found in Wolff *et al.* [1996], Drijfhout *et al.* [1996], and Thomas [2002].

The variations in atmospheric pressure at the surface of the ocean can cause the sea water to move: high atmospheric pressure can “press” the water in such a way that the “pressed” water flows to regions where the atmospheric pressure is lower. The change in surface elevation is equal to the depression that would be registered by a water barometer. The result is that pressure changes at the surface of the ocean are not transferred to the ocean floor but compensated by the changed height of the water column. This compensation is called “inverse barometer (IB) effect”. Because of this interaction between atmosphere and ocean, they are generally considered as a system and the computed gravity coefficients from atmosphere and ocean can be combined.

Before combining the atmosphere with ocean, a mean vertically integrated field of the atmosphere and a mean ocean field are usually subtracted. The reason is that the mean mass distribution of the atmosphere and ocean refers by definition to the static part of the gravity field. Only the deviations from the mean value can be regarded as the short-term gravitational variations. In the current GRACE mission (as well as in this dissertation), mean fields of atmosphere-ocean signal obtained from the years 2001+2002 are subtracted.

After the subtraction of the mean value, the ECWMF-OMCT combination of the year 2003 is used in this dissertation to represent the fast-changing atmosphere-ocean signal (also called AO for short in the following text), where the OMCT model is forced by the ECMWF atmospheric winds and surface pressure. Figure 3-4 shows the mean value of the AO signal for January 2003, which ranges from -7.22 mm to 11.3 mm with a RMS of 3.19 mm.

Similarly to the analysis for the LaD model, the spectral frequency analysis of the AO signal is carried out, which again employs the Fourier transform as described in section 2.3. Figure 3-5 shows the degree RMS plot for the year 2003 to degree and order 180 (panel a) and 30 (panel b). As the data is given in 6 hour intervals, there are totally 1460 samples for the year 2003. This amount of data enables an analysis of the frequency up to 730 cpa, i.e. semi-diurnal variation. As one can observe the signal content is concentrated in the low degrees as well. The strongest content is to be seen below degree 10, while the signal content above degree 40 decreases significantly. Besides the lower frequency part on the upper left corner, there is a significant signal at daily frequency (365 cpa) observable. High frequencies can be also observed at 730 cpa and 705 cpa, which correspond to 12 h and 12.425 h. It is reported (ESA report 20403 van Dam *et al.* [2008]) that the AO data is primarily driven by signals with frequencies between 30 and 182 days. Besides, it also contains frequencies in the range of 0.5-2 days as well as 2-30 days. This conclusion supports the findings from Figure 3-5. These findings indicate that if the recovery of the AO signals is a primary objective of a future mission, a temporal sampling of one day or even 12 hours should be fulfilled. As described in section 2.3, such high temporal sampling will result in a very poor spatial sampling for a single sensor mission. Thus multi-sensor constellations should be developed to obtain optimal time and space resolution for AO signal recovery.

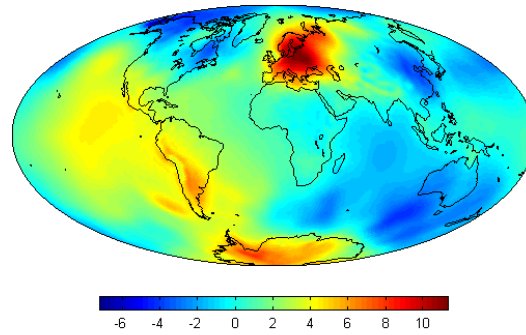


Figure 3-4 Mean AO geoid for 01.2003 in [mm], max = 11.3, mean = 1.46, min = -7.22, RMS = 3.19

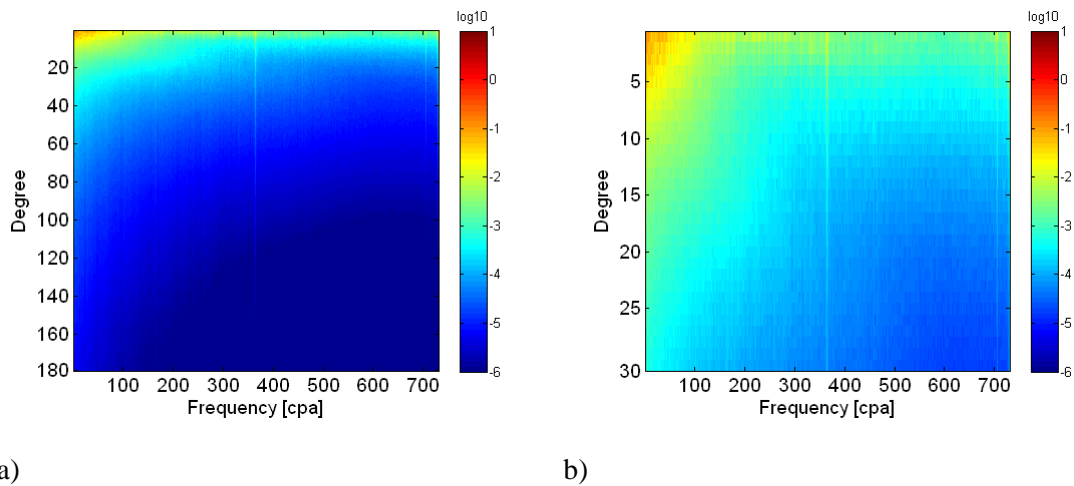


Figure 3-5 Degree RMS of AO for the year 2003, up to degree 180 (a) and degree 30 (b)

Since the mass movement and redistributions in the atmosphere and ocean occur at very high temporal frequencies, they will alias into the recovered gravity field with lower temporal resolution (e.g. with monthly resolution). This kind of aliasing error has been treated via the de-aliasing process for the current GRACE mission, where models of the AO signal are used to remove the impact of fast-changing mass variations in the atmosphere and ocean. Any difference between the reality and the model will remain in the GRACE solutions as de-aliasing error. This issue will be further discussed in section 4.4.2.

3.4. Ocean tides

Because OMCT does not include ocean tides, the ocean tide model FES2002 is included in the simulation studies in order to make the simulation environment a step closer towards reality. The purpose of this dissertation, however, is not to try to recover the ocean tides signal. The attempt is to show the non-conservativeness effect of ocean tides and its impact on the recovery of the gravity field. Nevertheless a short description about the tidal force, tidal potential and the FES2002 model itself is given here.

The gravitational force from Sun and the moon determines the orbital motion of the Earth, which is the largest effect of that force on the Earth orbit. Besides the orbital motion, there is the effect of differential acceleration between the Earth's surface and centre of mass, known as tidal effect, which is the cause of the tidal deformation of solid Earth and oceans. To a high degree of approximation, the orbital force is the average of all the gravitational forces on the earth and it equals the force acting on the centre of the earth. The tidal force is the difference of the force of a point on the earth and the average force. The tidal force, by its definition, causes no net force on the earth and so does not affect the earth's orbital motion. The tidal force from the Moon is about 2 times larger than that from the Sun, due to the fact that the Moon is much closer to the Earth than the Sun is.

The tidal force can be qualitatively described by the tidal potential. The tidal potential at a point P on the Earth due to the gravitational attraction of the moon is defined by

$$V_T = \frac{GM_M}{r_{EM}} \sum_{n=2}^{\infty} \left(\frac{R}{r_{EM}} \right)^n P_n(\cos\psi) \quad (3.22)$$

where GM_M is Moon mass times gravitational constant, R is the Earth's radius, r_{EM} is the Earth-Moon distance, ψ is the angle between the position vector of P and the position vector of the Moon, P_n is the Legendre function of degree n and the origin of the coordinate system is the centre of the Earth. For detailed derivation of the equation one refers to Schrama [2005]. In the Earth-Moon system, R/r_{EM} is about 1/60, which means the tidal potential decreases about 60 times by increasing the degree by 1. Thus in practice it doesn't make much sense to extend the tidal potential beyond degree 3. Equation (3.22) holds for the Sun as well, whereby GM_M and r_{EM} should be replaced by Sun mass times gravitational constant GM_S and the Earth-Sun distance r_{ES} , respectively.

Since equation (3.22) is dependent on the astronomical position of the moon or sun, it is not really convenient for most of the applications where tidal potential is required. Darwin (1883) invented a "letter-digit combination", known as "Darwin symbol" to describe the prominent frequencies of the tides. For example, M2 denotes the tides due to gravitational attraction of moon at a twice daily frequency. Doodson (1921) calculated an extensive table of spectral lines which can be linked to the original Darwin symbols. With the advent of the computer techniques in the 1970s, Cartwright and Eden (1973) computed new tables to verify the earlier work of Doodson. The tidal frequencies in these tables can be identified by means of so called Doodson numbers, which are computed in the following way:

$$D = k_1(5 + k_2)(5 + k_3)(5 + k_4)(5 + k_5)(5 + k_6) \quad (3.23)$$

where each k_1, \dots, k_6 is an array of integers. More details can be found in Cartwright [1993] and [1999]. In theory there exist infinite many Doodson numbers, while in practice a few hundred numbers are enough for most applications.

Ocean tides are the response of the ocean to the luni-solar gravitational attraction. They occur exactly at the same frequencies with other tides, i.e. with semi-diurnal, diurnal and long period frequency. In

3.4 Ocean tides

most of the regions on the earth the ocean tidal effects are about 0.5 to 1 meter high. In some places, e.g. Normandy and Brittany, tidal effect can be amplified to 10 meter. Figure 3-6 shows the global M2 ocean tide. The top panel shows the amplitude and the bottom panel shows the corresponding phases. The point where all phase lines join is called node. At the nodes the amplitude is 0 and the tidal wave is continuously rotating about this fixed geographical location. The contour map lines in top panel shows the amplitude of the high tide. For example, 50 cm means actually the difference between high and low tide is 100 cm. The 0 phase in the bottom panel refers to a state, where the high tide due to lunar attraction at the equator is equal to the gravitational bulge. This state is also referred as hydrostatic. In this state one assumes that the ocean water is not restricted by the ocean bottom or the coastlines and the Moon is at equator, which causes high tide at equator.

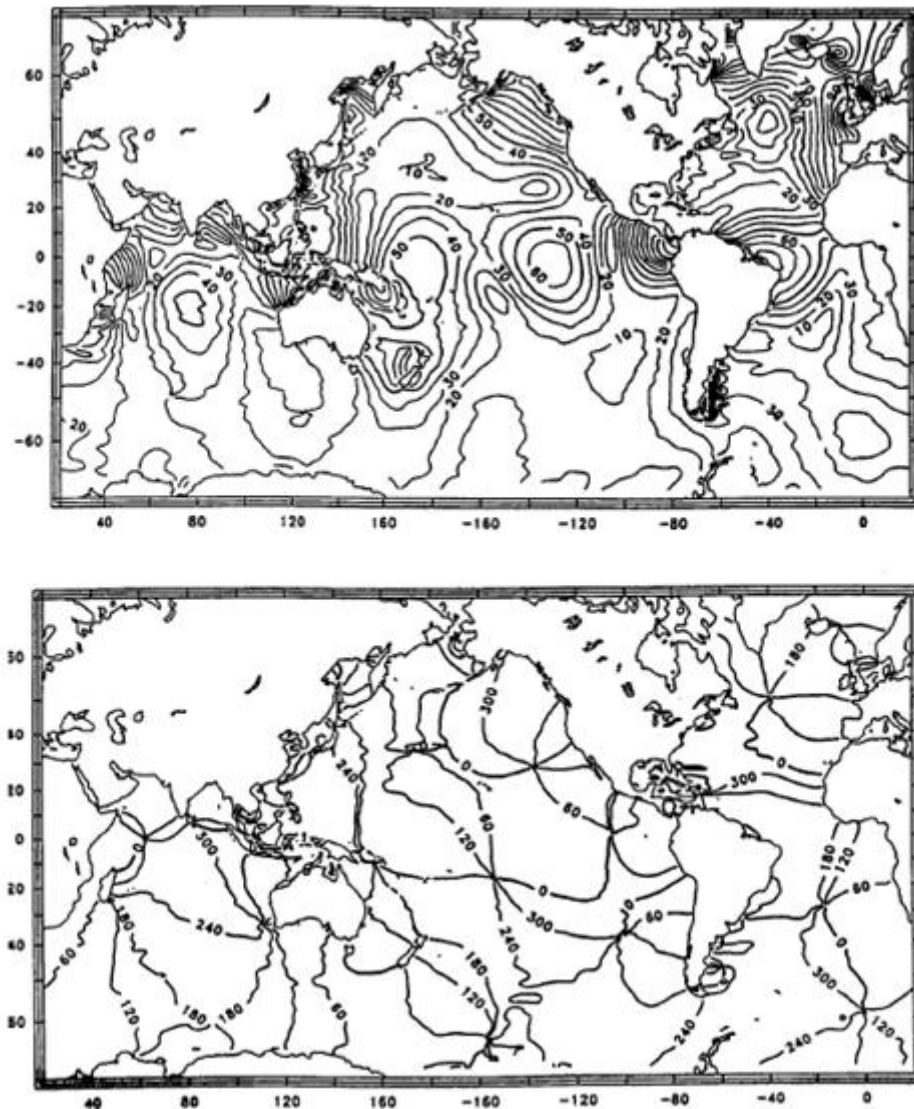


Figure 3-6 M2 ocean tides, amplitude in centimeter (top panel) and the corresponding phase (bottom panel), Schrama [2005]

Ocean tides models help to describe and understand the ocean tides quantitatively. From the 1990s on, a large number of new tidal atlases were developed, primarily to provide accurate tidal corrections for satellite altimetry applications. During this decade, the French tidal group (FTG) produced a series of finite element solutions (FES) tidal atlases. FES2002 is one of the released atlases, computed from the tidal hydrodynamic equations and data assimilation. This model consists of major tidal constituents of different frequencies, e.g. semi-diurnal M2, S2, K2 or diurnal K1, O1 components. Detailed

description of the different tidal constituents together with the corresponding frequencies and amplitudes can be found e.g. in Desai [1996] or Schrama [2005]. For more information about the FES2002 model, one refers to Lefevre *et al.* [2002] or Le Provost *et al.* [2002].

Since ocean tides redistribute mass at high temporal frequencies, their impact on the gravity solution with lower temporal resolution, e.g. monthly resolution, should be investigated. In fact, the fast-changing ocean tide is considered to be one of the sources for the remaining de-aliasing error in the temporal gravity fields recovered from GRACE (Knudsen and Andersen [2002], Seo *et al.* [2008a]). Further discussion on this issue will be given in section 4.4.2.

The hydrology, atmosphere-ocean and ocean tides signals build together the water cycle in this dissertation, neglecting ice melting. The data sets used in this dissertation are the hydrology model (LaD), atmospheric mass redistribution (ECMWF), non-tidal ocean mass redistribution (OMCT) and ocean tide model (FES2002), which will be implemented in the simulation studies in Chapter 4.

3.5. Non-conservativeness of time-variable gravity signals

If the Earth gravity field is conservative, then the integration terms in equations (2.14) and (2.15) are path-independent. In this case the potential differences along an orbit arc do not need to be computed from integration of accelerations along the orbit, but they can be computed directly from the potential field, which is by definition a conservative one. This does not hold for the time-variable components of the gravity field as they are not conservative. In order to apply the energy balance approach to the time-varying field the observation equation needs to be modified, taking into account the non-conservativeness of the field.

For time-variable gravity signals, the accelerations need to be integrated along the orbit and the resulting potential difference is path-dependent. If one neglects the non-conservativeness of the time variable part of the gravity field, an error will be introduced, which will be called the error of non-conservativeness in the following text. This holds even if the potential function is modeled to follow a certain time variable characteristic which perfectly matches reality (like a secular drift superimposed by annual or semi-annual periods). In order to show the magnitude of this error, the difference between potential values computed from (i) integration of accelerations along the orbit and (ii) directly from a given set of (time variable) potential coefficients through spherical harmonics synthesis is plotted. The latter case does not take into account the non-conservativeness of the field. The order of magnitude of the error, i.e. the difference between the results from method (i) and (ii), decides upon whether the specialized observation equations for conservative field can be applied, or the more complex equations (2.16) and (2.17) need to be implemented for the estimation of the corresponding time variations. The error due to direct tides and ocean tides, as well as due to time variable signals in continental hydrology and atmosphere and ocean (without tides) will be shown. In practice all atmosphere/ocean and tidal effects are to a large extent known from models, while the continental hydrology is the quantity to be determined. Thus the error introduced in the case of hydrology is especially important for time variable gravity field recovery using the energy integral.

In the following the results of the difference between (i) and (ii) will be presented both for a single satellite and for a two-satellite-constellation. Consequently direct tides, ocean tides, hydrology and atmosphere-ocean signals will be discussed. These four signals have different size and variability:

- Direct tide is the largest time variable effect but it is well-known. This example nicely illustrates the effect of the non-conservativeness.

3.5 *Non-conservativeness of time-variable gravity signals*

- Ocean tide is much smaller than the direct tides but it changes very fast.
- Atmosphere-ocean signal is smaller than ocean tide and it contains both low and high frequencies.
- Hydrology is comparable to atmosphere-ocean signal in amplitude, does not change fast, but it is the quantity to be determined.

Thus by investigating the above mentioned signals, the relation between the error of non-conservativeness and the magnitude as well as the variability of the individual signals can be analyzed. For detailed information on classification of the time-variable gravity signals one refers to e.g. Peters [2007] or Sneeuw *et al.* [2005]. As mentioned the investigation on the hydrology signal is more of interest as this is the only unknown quantity. It is interesting to know how large the error can be if one neglects the non-conservativeness for hydrology. If the error is small enough, one can skip the relatively complex computation as shown in section 2.1 and stick to the specialized energy equation for static field recovery.

Single satellite

In this section the error due to neglecting the non-conservativeness of the time-variable field for a single satellite is presented. As mentioned before, the error is computed for the direct tides, ocean tides, hydrology and atmosphere-ocean signal. Figure 3-7 shows the direct tidal potential computed along the orbit of Swarm A over 30 days from (i) the integration of tidal accelerations along the orbit as well as epochwise from (ii) potential coefficients of the time variable tidal field. The upper panel in Figure 3-7 shows, that both curves (i) and (ii) show the same characteristic twice per revolution signal with an amplitude of about $1.5 \text{ m}^2/\text{s}^2$. This order of magnitude is the well known size of the tidal potential (see e.g. Torge [2001]), where the twice per orbit signal is caused by the motion of the satellite in the inhomogeneous tidal field. In addition, the gray curve (i) contains a considerable drift. Taking a look at the full 30-days time series (lower panel), the overall structure of the two signals becomes visible. While the black curve (ii) stays almost constant (except for the twice per revolution signal), the gray curve (i) shows a pronounced 14-days oscillation superimposed by a drift, which turns out to be a half yearly signal in even longer time series. These frequencies are main constituents of the direct tidal signal. The difference between both curves arises from the fact that the integration of accelerations performed in (i) holds for arbitrary fields, while (ii) assumes the field to be a conservative one. Since the tidal field changes in time, it should not be regarded as conservative. Therefore it is crucial in the energy integral, to integrate all known time-variable forces along the orbit, rather than to directly compute the potential from a set of spherical harmonic coefficients. The effect of non-conservativeness is denoted by ε_{con} , where it holds (without considering the integration constant)

$$\int_t \nabla V^u \cdot \underline{\dot{x}} dt = V^u(t) + \varepsilon_{con}(t) \quad (3.24)$$

It must be noted, that ε_{con} can be quite large. In case of the direct tides the amplitude of the 14-days signal is about $50 \text{ m}^2/\text{s}^2$, while the tidal potential V^u amounts to just about $1.5 \text{ m}^2/\text{s}^2$. The relation between ε_{con} and V^u might change, depending on the field under consideration, but in general, when working with the energy integral, the non-conservativeness needs to be taken care. Otherwise large drift effects can remain in the pseudo-observations that can degrade the gravity field recovery.

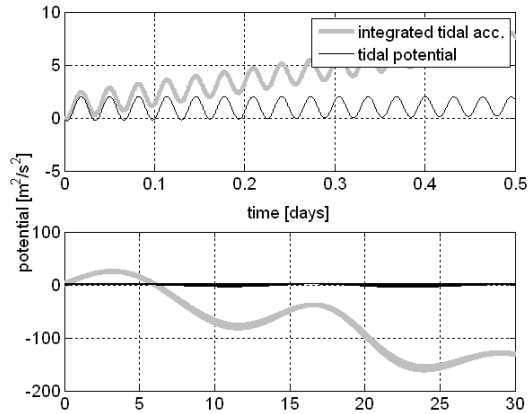
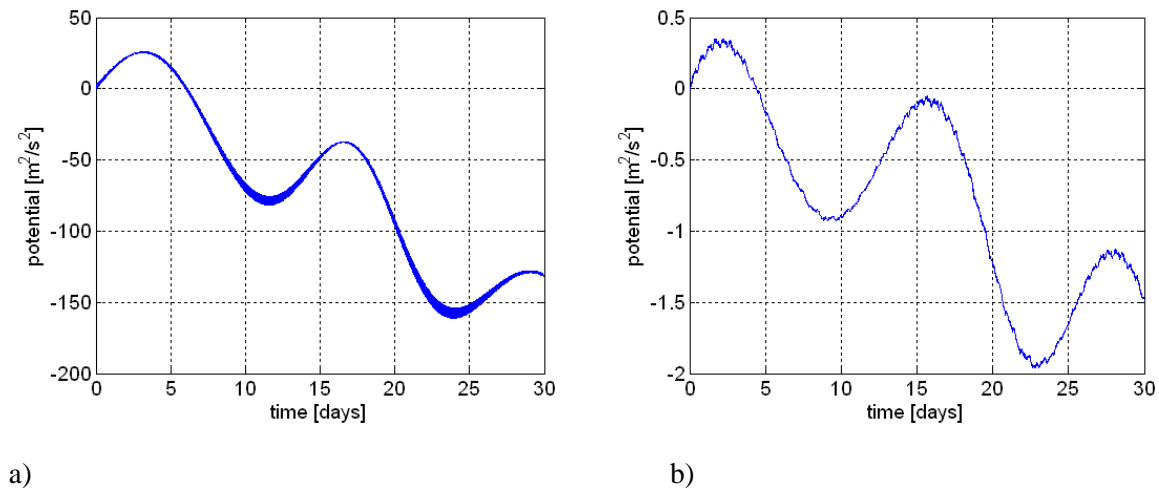


Figure 3-7 Time series of tidal potential along a satellite orbit from (gray) integration of tidal accelerations and (black) synthesis from tidal potential harmonic coefficients. The upper panel shows a zoom-in version of the first half day of the 30 days shown in the lower panel.

Figure 3-8 shows the size of ε_{con} for direct tides, ocean tides, hydrology and atmosphere-ocean signal for Swarm A. Here only the differences between directly computed potential and integrated accelerations from 1-month simulations are plotted. The size of ε_{con} for direct tides ranges from $-150 \text{ m}^2/\text{s}^2$ to about $30 \text{ m}^2/\text{s}^2$ (panel a)), which is quite large. Panel b) reveals again a pronounced 14-day signal, with an amplitude of about $0.5 \text{ m}^2/\text{s}^2$ and a superimposed drift of about $-1.5 \text{ m}^2/\text{s}^2$ per month for the ocean tides signal. In panel c) the ε_{con} for hydrology signal shows a linear drift with much smaller magnitude of about $0.5\text{e-}3 \text{ m}^2/\text{s}^2$ per month, superimposed with an oscillation of about $0.1\text{e-}3 \text{ m}^2/\text{s}^2$. The atmosphere-ocean signal in panel d) shows a quasi-periodic pattern with amplitude of about $0.12 \text{ m}^2/\text{s}^2$, superimposed with an oscillation of about $2\text{e-}3 \text{ m}^2/\text{s}^2$. It can be seen that in general, the non-conservativeness of the time-variable gravity signals can cause a drift for a single satellite, the size of which varies for different signals. The size of ε_{con} for individual signals is summarized in Table 3-2.



a)

b)

3.5 Non-conservativeness of time-variable gravity signals

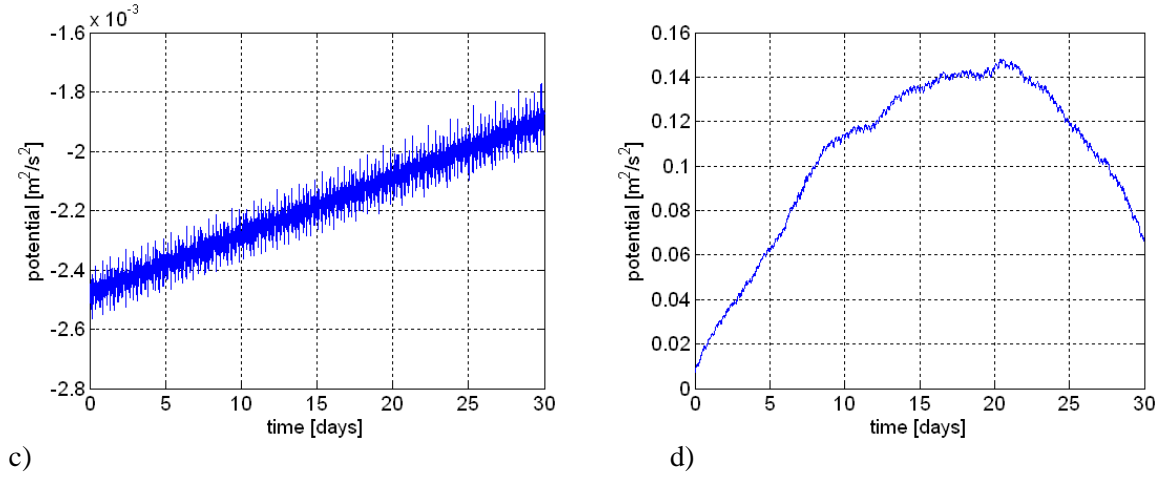


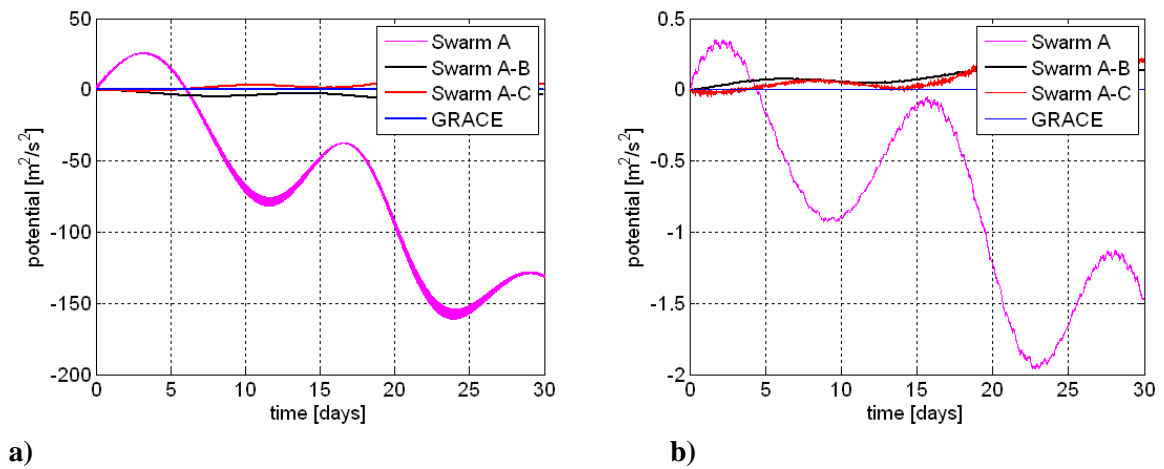
Figure 3-8 Effect of non-conservativeness for a single satellite (m^2/s^2), a) direct tides, b) ocean tides, c) hydrology and d) atmosphere-ocean

2-satellite-constellation

In case of satellite constellations like Swarm A-B or GRACE, the long wavelength structure of (i) can be expected to be very similar for different satellites orbiting the earth at the same time and at almost the same place. Therefore, when dealing with potential differences between satellites, ε_{con} can be expected to be smaller than for a single satellite. Then it holds

$$\int_t (\nabla V_2^u \cdot \dot{\underline{x}}_2 - \nabla V_1^u \cdot \dot{\underline{x}}_1) dt = V_{12}^u(t) + \varepsilon_{con}(t) \quad (3.25)$$

Similarly, the difference between (i) and (ii) for different signals is plotted in Figure 3-9. For reference the single satellite case (Swarm A) is plotted as well. The statistical values are summarized in Table 3-2.



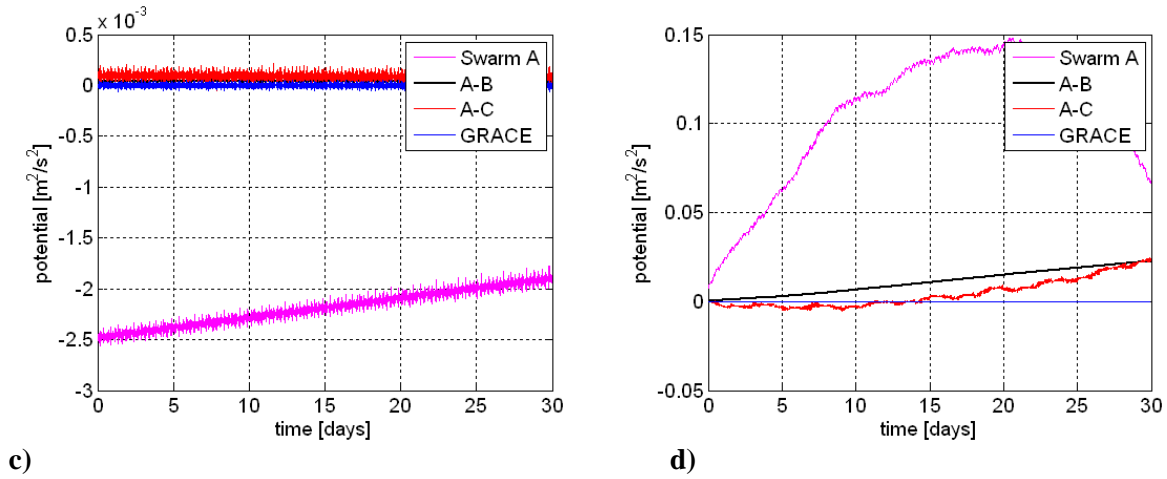


Figure 3-9 Effect of non-conservativeness for 2-satellite constellation ([m²/s²]), a) direct tides, b) ocean tides, c) hydrology, d) atmosphere-ocean

Table 3-2 Difference between integrated accelerations and directly computed potential [m²/s²]

Constellation	Max	Mean	Min	Sigma
Direct tides				
Swarm A	156.81	68.59	-23.92	58.44
Swarm A-B	-0.085	-3.57	-6.11	1.41
Swarm A-C	6.76	2.68	-1.03	2.13
GRACE	0.04	0.0031	-0.02	0.012
Ocean tides				
Swarm A	0.35	-0.75	-1.96	0.66
Swarm A-B	0.14	0.078	-8.1e-3	0.033
Swarm A-C	0.23	0.075	-0.049	0.064
GRACE	1.3e-3	-1.69e-5	-1.6e-3	2.97e-4
Hydrology				
Swarm A	0	-2.2e-3	-2.6e-3	1.70e-4
Swarm A-B	6.18e-5	4.16e-5	0	1.80e-6
Swarm A-C	2.17e-4	8.88e-5	-6.91e-5	1.62e-5
GRACE	6.58e-5	-2.16e-8	-2.5e-3	1.07e-5
Atmosphere-ocean				
Swarm A	0.148	0.105	0.0075	0.0372
Swarm A-B	0.023	0.011	3.25e-4	0.0068
Swarm A-C	0.025	0.0044	-0.0053	0.0079
GRACE	7.5e-3	7.7e-7	-1.82e-4	3.26e-5

As expected, the size of ϵ_{con} is smaller for 2-satellite constellations than for the single satellite. Figure 3-9 a) and b) show that also some 2-satellite constellations, namely Swarm A-B and A-C, show periodic signatures, although the periodic pattern is much smaller than for the single satellite. In panel d) Swarm A-B and A-C show a linear drift instead of the quasi-periodic pattern for Swarm A. In all cases the GRACE constellation shows the smallest effect and ϵ_{con} stays almost always constant around 0 for all the time-variable gravity signals. The reason might be the way that the GRACE constellation is generated here: there is no second orbit simulated and GRACE B is generated by taking the position of GRACE A at an earlier epoch, where the two epochs are about 200 km apart from each other. In this way the value of two epochs may not vary much. However, since the real GRACE mission is indeed a leading-following formation with a distance of about 220 km between the two satellites, the

3.5 Non-conservativeness of time-variable gravity signals

long wavelength structure can still be expected to be similar for both satellites. Thus the non-conservativeness effect for the real GRACE mission should be smaller than that for a single satellite as well.

It is interesting to compare the numbers in Table 3-2 with the results of the simplified error analysis in section 2.2. There, error standard deviations of $0.08 \text{ m}^2/\text{s}^2$ were given for GPS-baselines and $8 \cdot 10^{-4} \text{ m}^2/\text{s}^2$ for inter-satellite links of K-band quality. The comparison gives some indication on whether the error ε_{con} can be neglected or not, i.e., whether the simple but specialized observation equation can be used, or the more complex generalized version needs to be used to recover time-variable signal components. In conclusion one can state, that the error cannot be neglected both for single satellites and satellite constellations in case of tidal effects. At least for high-accurate K-band links, this also holds true for mass variations in atmosphere and ocean, where the error ε_{con} is above the K-band accuracy. In case of GPS-baselines, the error of atmosphere-ocean is below the observation accuracy. For all those signals it must however be stated, that they are to a large extent known from models or external observations and therefore they do not need to be recovered. Thus, they show up as reductions on the right hand side of the observation equations (2.14) to (2.15), where the integration along the orbit is straightforward and does not increase the complexity of the computations. Remaining model residuals might be small enough for ε_{con} to be neglected. The same holds true for the time variations caused by continental hydrology. These are obviously moderate enough not to generate large values of ε_{con} , i.e., the field can be considered to be conservative, at least considering the current accuracy level of the observations (both GPS and K-band). Therefore one can conclude that sub-monthly variations in continental water storage (represented by LaD model) are so small, that the hydrology component of the gravity field can be considered conservative, i.e., static within one month. In consequence, one can apply the specialized observation equations in recovering monthly fields of continental water storage.

To sum up, it is clear that all these time variations are not conservative and therefore their contribution has to be taken care of. Depending on the object to recover, different treatments should be implemented:

- If one aims to recover the static field only, all known non-conservative gravity forces should be removed via integration of the corresponding accelerations along the orbit to avoid the impacts of non-conservativeness on the recovered static field. This case will be further discussed in section 4.3.
- If the time variation is the objective to determine, one needs to follow the complex computation steps listed from equation (2.18) to (2.31) to exclude the non-conservativeness impacts, strictly speaking. As discussed above, the impact of non-conservativeness for hydrology signal, however, is even below the current K-band accuracy level. This indicates that it should be acceptable to ignore the non-conservativeness of hydrology and still stick to the energy integral used for static field determination, assuming all other time variations are well-known or accurate enough measured. This issue will be further investigated in section 4.4 and 4.5.

4. Simulation studies

4.1. Introduction to the simulator

The simulations described in this chapter are all based on the same software package, which is a set of programs in different programming languages and platforms, including C/C++ and Matlab. In this section a brief introduction to the simulator itself is given. For the convenience of description, the full calculation chain is illustrated as a flowchart in Figure 4-1. Note that different colors and shapes of the objects in the plot have different meanings:

- Ellipsoidal boxes in this plot contain the parameters and coefficients, which are either input or output of the individual calculation processes
- Black rectangular boxes stand for the calculation processes
- Black arrows indicate the data flow
- Red boxes together with red arrows represent the optional possibilities for control and comparison purposes
- The yellow ellipsoidal box with the blue arrow stands for the option of adding time variations in orbit simulation

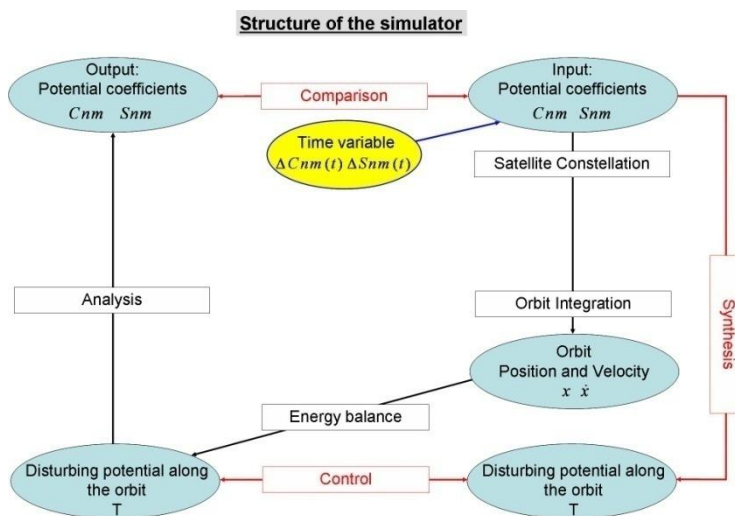


Figure 4-1 Simulation flowchart (based on Peters [2007])

The main components of the simulator will be described in the following.

Orbit integration

The integration of a satellite orbit in a given gravity field provides time series of position vector $\underline{x}(t)$ and velocity vector $\underline{\dot{x}}(t)$. Note that in this simulator only gravitational forces are implemented, non-

4.1 Introduction to the simulator

gravitational force models, such as atmospheric drag, albedo or solar radiation pressure are not considered. The realization of the orbit integration is described briefly below.

The gradient of the gravitational potential V can be computed in an Earth-fixed coordinates system as

$$\nabla V = \begin{pmatrix} \partial V / \partial x \\ \partial V / \partial y \\ \partial V / \partial z \end{pmatrix} \quad (4.1)$$

where $\underline{x}(t)$ stands for the time series of the 3-dimensional positions.

The partial differentials of the potential V (see equation (2.18)) can also be expressed in the spherical coordinates $\{r, \theta, \lambda\}$ as

$$\frac{\partial V}{\partial r} = -\frac{GM}{r^2} \sum_{n=0}^{\infty} (n+1) \left(\frac{R}{r}\right)^{n+1} \sum_{m=0}^n \bar{P}_{nm} [\bar{C}_{nm} \cos m\lambda + \bar{S}_{nm} \sin m\lambda] \quad (4.2)$$

$$\frac{\partial V}{\partial \theta} = \frac{GM}{r} \sum_{n=0}^{\infty} \left(\frac{R}{r}\right)^{n+1} \sum_{m=0}^n \frac{\partial \bar{P}_{nm}}{\partial \theta} [\bar{C}_{nm} \cos m\lambda + \bar{S}_{nm} \sin m\lambda] \quad (4.3)$$

$$\frac{\partial V}{\partial \lambda} = \frac{GM}{r} \sum_{n=0}^{\infty} \left(\frac{R}{r}\right)^{n+1} \sum_{m=0}^n m \cdot \bar{P}_{nm} [\bar{S}_{nm} \cos m\lambda - \bar{C}_{nm} \sin m\lambda] \quad (4.4)$$

The formulas to calculate the fully normalized Legendre functions \bar{P}_{nm} and their derivatives are described e.g. in Heiskanen and Moritz [1967]. Combining equation (4.1) to (4.4), the gradient of the gravitational potential can then be written as following:

$$\frac{\partial V}{\partial x} = \frac{\partial V}{\partial r} \frac{\partial r}{\partial x} + \frac{\partial V}{\partial \theta} \frac{\partial \theta}{\partial x} + \frac{\partial V}{\partial \lambda} \frac{\partial \lambda}{\partial x} \quad (4.5)$$

$$\frac{\partial V}{\partial y} = \frac{\partial V}{\partial r} \frac{\partial r}{\partial y} + \frac{\partial V}{\partial \theta} \frac{\partial \theta}{\partial y} + \frac{\partial V}{\partial \lambda} \frac{\partial \lambda}{\partial y} \quad (4.6)$$

$$\frac{\partial V}{\partial z} = \frac{\partial V}{\partial r} \frac{\partial r}{\partial z} + \frac{\partial V}{\partial \theta} \frac{\partial \theta}{\partial z} + \frac{\partial V}{\partial \lambda} \frac{\partial \lambda}{\partial z} \quad (4.7)$$

To implement a transform between spherical and Cartesian coordinates the following partial differentials are needed:

$$\begin{aligned} \partial r / \partial x &= \sin \theta \cos \lambda & \partial r / \partial y &= \sin \theta \sin \lambda & \partial r / \partial z &= \cos \theta \\ \partial \theta / \partial x &= \cos \theta \cos \lambda / r & \partial \theta / \partial y &= \cos \theta \sin \lambda / r & \partial \theta / \partial z &= -\sin \theta / r \\ \partial \lambda / \partial x &= -\sin \lambda / (r \sin \theta) & \partial \lambda / \partial y &= \cos \lambda / (r \sin \theta) & \partial \lambda / \partial z &= 0 \end{aligned} \quad (4.8)$$

For every integration epoch, the gravitational forces act on the satellite and affect its orbit. The acceleration vector of the satellite can be computed via the relation $\underline{\ddot{x}} = \nabla V$ and is then transformed from the Earth-fixed to the inertial system. There it is integrated twice, which gives the velocity vector $\underline{\dot{x}}(t)$ and position vector $\underline{x}(t)$, respectively. The $\underline{\dot{x}}(t)$ and $\underline{x}(t)$ vectors are transformed back to the Earth-fixed system for further calculations. For details of the transformation one refers to Schmidt [1999].

The realization of the above mentioned orbit integration process is based on C/C++ programs, which inherits the *IAPG orbit integrator* and is modified for the purpose of this dissertation. It runs under an open sourced Integrated Development Environment *CodeBlocks* (www.codeblocks.org), which is

platform independent and thus offers the possibility of a smooth implantation also under LINUX. The orbit integrator provides integrated satellite orbits based on given initial conditions, which includes simulation parameters such as starting time, integration duration, sampling rate, initial satellite position and velocities etc. The gravity field model is modified in such a way that besides the static field EGM96, also time variations can be taken into consideration for orbit integration. Depending on the chosen options, the integrator is able to take one or a combination of the following time variation models into consideration:

- Hydrology signal (LaD model), either in 6-hourly or in monthly resolution
- Atmosphere and ocean signal (ECMWF-OMCT) in 6-hourly resolution
- Ocean tides model (FES 2002)

Output files contain the error-free orbits, given in 3-dimensional positions and velocities. If chosen, it can also provide the accelerations due to time variations at the integration epochs. These outputs are then the input parameters for the energy balance equation to calculate the disturbing potential.

Time variation

When chosen, time variations can be added to the static field EGM96. Depending on the resolution of the time variations, i.e. monthly or 6-hourly, different algorithms apply. For monthly resolution the hydrology signal is added to the beginning of each month to the static field. Within a month there is no interpolation implemented. For the variations given in 6-hourly resolution the temporal signal is added every 6 hours with linear interpolation in between. Table 4-1 explains this interpolation algorithm, where “S” stands for static field EGM96, “C1”, “C2”, “C3”, “C4” stand for the time variation coefficients at 0h, 6h, 12h and 18h on the first day, “t” stands for time and is given in seconds. The “gravity status” rows means that the gravity field at 0h, 6h or 12 h are the summations of the static field and the corresponding time variation. Within every 6 hours, the time variations are linearly interpolated using the neighbouring epochs, which is shown in the row “Change within 6 hours”. The row “gravity field at epoch” represents the gravity field at current epoch, which is a combination of the static part, the time-variable part at and the interpolation part within every 6 hours. In this sense the gravity field is changing almost constantly as in the real world.

Table 4-1 Adding time variation to static filed

Time	0h	6h	12h	18h
Time variable from all sources	C1	C2	C3	C4
Gravity status	S + C1	S + C2	S + C3	...
Change within 6 hours	$\frac{C2-C1}{6} \cdot \frac{t}{3600}$	$\frac{C3-C2}{6} \cdot \frac{t}{3600}$	$\frac{C4-C3}{6} \cdot \frac{t}{3600}$...
Gravity field at epoch	$S + C1 + \frac{C2-C1}{6} \cdot \frac{t}{3600}$	$S + C2 + \frac{C3-C2}{6} \cdot \frac{t}{3600}$	$S + C3 + \frac{C4-C3}{6} \cdot \frac{t}{3600}$...

Synthesis

From the given potential coefficients, the disturbing potential at a given position $\{r, \theta, \lambda\}$ can be directly calculated by

$$T(\underline{x}, t) = \frac{GM}{R} \sum_{n=0}^{\infty} \left(\frac{R}{r(t)}\right)^{n+1} \sum_{m=0}^n \bar{P}_{nm}(\cos \theta(t)) [\bar{C}_{nm} \cos m\lambda(t) + \bar{S}_{nm} \sin m\lambda(t)] \quad (4.9)$$

The coefficients \bar{C}_{nm} and \bar{S}_{nm} indicate that the even zonal coefficients from degree 0 to degree 8 of a normal gravity field are subtracted. The calculation of the disturbing potential from the synthesis approach will be used as a control of the energy balance approach. Meanwhile, the difference between the disturbing potential calculated from the energy balance approach and directly from synthesis can be used to compute the constant C. In the simulation the constant C equals the difference of the potential value at first simulation epoch.

Energy balance approach

The energy balance method has been described in Chapter 2. Given the position and velocity, the energy balance equation provides the disturbing potential along the orbit, which will be used as input by the analysis step.

Backward calculation (Analysis)

This step is the inverse of the synthesis and therefore named analysis. The analysis step takes the disturbing potential as input and computes the unknown potential coefficients by means of least squares adjustment. Sneeuw [1994 and 2003b] has given the computation process in detail. In case of SST high-low the partial derivatives of the disturbing potential with respect to the spherical harmonics coefficient can be computed as:

$$\frac{\partial T}{\partial C_{nm}} = \frac{GM}{R} \left(\frac{R}{r}\right)^{n+1} \bar{P}_{nm}(\cos \theta) \cos m\lambda \quad (4.10)$$

$$\frac{\partial T}{\partial S_{nm}} = \frac{GM}{R} \left(\frac{R}{r}\right)^{n+1} \bar{P}_{nm}(\cos \theta) \sin m\lambda \quad (4.11)$$

All these partial derivatives of each coefficient at each epoch, as shown in equation (4.12), form the design matrix A, which has a dimension of $(K \times (N + 1)^2)$, where N is the maximum degree of the coefficients to be determined and K is the number of observation epochs.

$$A = \begin{pmatrix} \frac{\partial T(1)}{\partial \bar{c}_{00}} & \frac{\partial T(1)}{\partial \bar{c}_{10}} & \dots & \frac{\partial T(1)}{\partial \bar{c}_{n0}} & \frac{\partial T(1)}{\partial \bar{c}_{11}} & \dots & \frac{\partial T(1)}{\partial \bar{c}_{mn}} & \frac{\partial T(1)}{\partial \bar{s}_{n0}} & \dots & \frac{\partial T(1)}{\partial \bar{s}_{mn}} \\ \frac{\partial T(2)}{\partial \bar{c}_{00}} & \frac{\partial T(2)}{\partial \bar{c}_{10}} & \dots & \frac{\partial T(2)}{\partial \bar{c}_{n0}} & \frac{\partial T(2)}{\partial \bar{c}_{11}} & \dots & \frac{\partial T(2)}{\partial \bar{c}_{mn}} & \frac{\partial T(2)}{\partial \bar{s}_{n0}} & \dots & \frac{\partial T(2)}{\partial \bar{s}_{mn}} \\ \vdots & \vdots \\ \frac{\partial T(K)}{\partial \bar{c}_{00}} & \frac{\partial T(K)}{\partial \bar{c}_{10}} & \dots & \frac{\partial T(K)}{\partial \bar{c}_{n0}} & \frac{\partial T(K)}{\partial \bar{c}_{11}} & \dots & \frac{\partial T(K)}{\partial \bar{c}_{mn}} & \frac{\partial T(K)}{\partial \bar{s}_{n0}} & \dots & \frac{\partial T(K)}{\partial \bar{s}_{mn}} \end{pmatrix} \quad (4.12)$$

The unknown coefficients can be solved through the least squares adjustment

$$x = (A^T P A)^{-1} A^T P \omega \quad (4.13)$$

with the error variance-covariance matrix of the coefficients $\Sigma_x = (A^T P A)^{-1}$, where:

- x is the vector of unknowns, here the spherical harmonics coefficients
- A is design matrix
- P is the weight matrix
- ω contains the time series of observations (here the disturbing potentials)

The weight matrix P is given by

$$P = \sigma_0^2 C^{-1} \quad (4.14)$$

where:

- σ_0^2 is a priori standard deviation of unit weight
- C is the variance-covariance matrix of the observations

Elements of the P matrix are proportional to the inverse of the corresponding error variance. That means an observation gets a larger weight, if its variance (or standard deviation) is smaller. In other words, the more accurate the observation is the larger weight it gets. If all the observations are equally accurate and uncorrelated, P will be a unit matrix. This assumption is adopted throughout this dissertation except for the additional discussion about the Swarm A-C baseline later in section 4.5. There all observations are assumed to be not equally accurate but still uncorrelated, as a results P is a diagonal matrix.

The backward calculation process is done with the Matlab program package SATLAB (Schmidt [1999]). As an option white noise of different noise levels can be added to the orbits before analysis.

Comparison

The output of the analysis is a set of potential coefficients. These coefficients can be compared with the input potential coefficients. The results of such comparisons provide an insight into the gravity recovery simulation and provide diverse meaningful information, related to the simulation purpose. The comparison results will be explained in details in the simulation results.

Validation of the simulator

Before running simulations it is important to make sure that the simulator is closed-loop. Thus a validation is necessary to test the accuracy of the simulator. For this purpose one test simulation is carried out. The results should show the correctness and the accuracy of the simulator.

This simulation is based on following settings:

- Static gravity field: EGM96
- Maximum degree: $N = 30$
- Starting Kepler elements: $a = 6378.137+370$ km, $I = 87^\circ$, $e = 0.003$, $\Omega = \omega = M_0 = 0$
- Integration length: 30 days, from 01.01.2003 to 30.01.2003
- Integration steps: $\Delta t = 30$ s
- Without time variations and orbit noise

Figure 4-2 panel a) shows 10 days of ground track of the simulated satellite orbit. The ground track reaches a relatively good coverage in 10 days already. It is seen that due to the high inclination the flight direction is nearly parallel to the meridian direction. The sampling rate of 30 seconds agrees with the normal temporal resolution of a dynamic or kinematical orbit (Peters [2007]) and is therefore dense enough. The disturbing potential along the orbit, computed from the energy balance approach, amounts from -800 to +600 m^2/s^2 (after subtracting the mean value), as shown in Figure 4-2 panel b). As a control the difference between the disturbing potential derived from the energy balance and that computed directly by synthesis along the orbit is computed and plotted in Figure 4-2 panel c). The difference is in the order of $10^{-6} \text{m}^2/\text{s}^2$, which is about 10^{-14} relative to the mean value of the disturbing potential (about $-2.98 \text{e}+007 \text{m}^2/\text{s}^2$). This difference in the disturbing potential results in a difference between the recovered field and the input EGM96 field. Figure 4-3 a) shows the difference in geoid height, which ranges from about $-0.04 \mu\text{m}$ to $0.04 \mu\text{m}$ (max = $0.038 \mu\text{m}$, min = $-0.042 \mu\text{m}$, mean = $-4.3\text{e}-5 \mu\text{m}$, sigma = $0.010 \mu\text{m}$). Panel b) shows the comparison directly in spherical harmonics. The biggest difference occurs for the term C_{00} with a relative error of about $1.421 \cdot 10^{-14}$. The C_{00} term contains the mass of the Earth including the mean mass of atmosphere-ocean and it has by definition the value 1, as the total mass of the earth is assumed to be constant. Here the difference in C_{00} is always neglected in comparisons of simulation results. Besides, the degree 1 terms, namely C_{10} , C_{11} and S_{11} , which describe the mass centre of the Earth with respect to the origin of the coordinate system, are always set to 0 in this dissertation. In this way it is assumed that the coordinate system always follows the change of the centre of mass of the earth, which may move due to mass transport and mass redistributions in the earth system. Thus the comparisons in all the simulation studies always start from degree 2, i.e. differences in degree 0 and 1 terms are neglected.

Apart from the error of the degree 0 term, relative large errors can be seen also for the coefficient of order 15 to 17. Swenson and Wahr [2006] have found a similar phenomenon for GRACE. This is a typical phenomenon of orbit resonance. There are also correlations between coefficients with even or odd degrees, i.e. even and odd coefficients do not correlate with each other, but coefficients of even or odd parity may correlate with each other. Despite these phenomena, in general the errors are so small that they can be regarded as numerical errors. Thus the simulator is regarded as closed-loop.

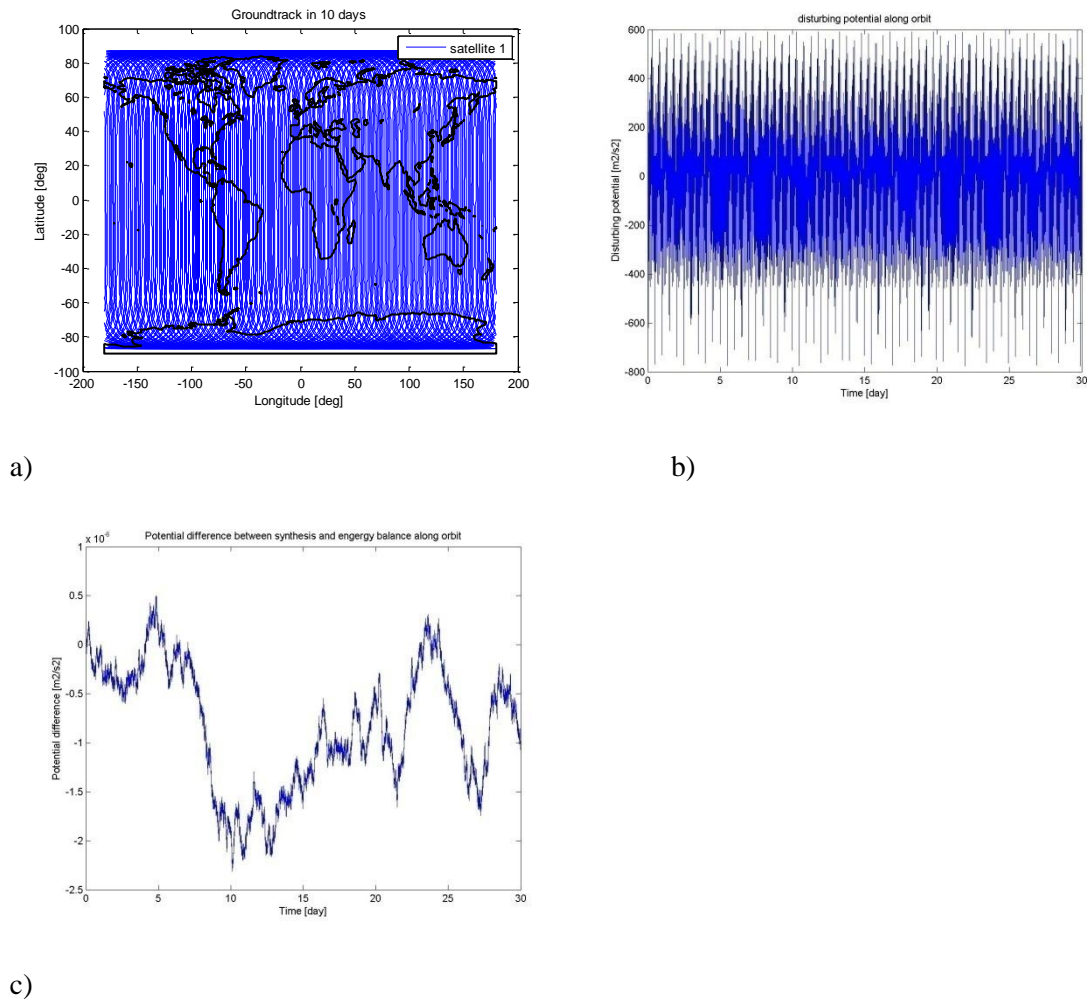


Figure 4-2 a) ground track plot of 10 days, b) disturbing potential along the orbit from energy balance, c) the difference between b) and the disturbing potential directly computed from synthesis

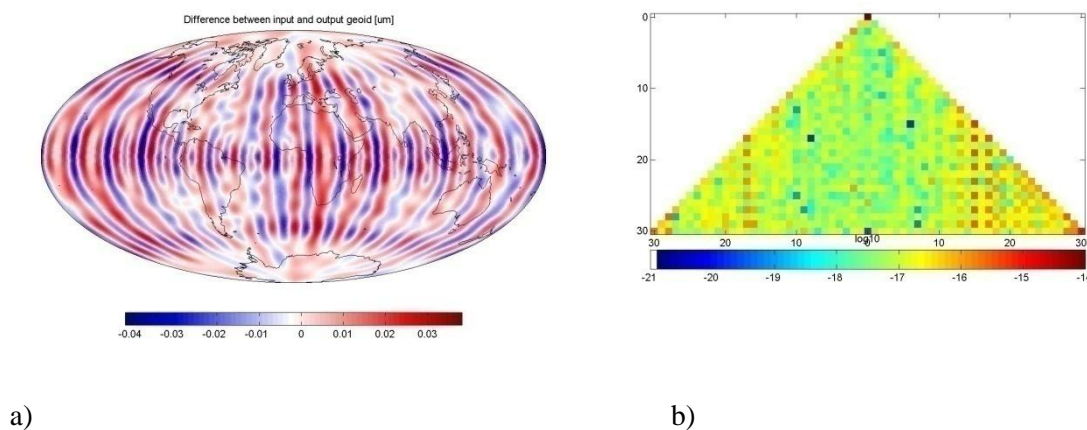


Figure 4-3 Difference between recovered and original EGM96 field in geoid (panel a)) and in spherical harmonics coefficients (panel b))

As the simulator is closed-loop, there will be no error introduced by the simulator itself during the whole computation process. Thus the differences between the input and output coefficients can give an insight to the recovery capability for various cases and provide meaningful information.

4.2. Introduction to simulated constellations

As introduced in section 1.2, one objective of this dissertation is to evaluate Swarm's potential for gravity field recovery. As a consequence, the Swarm constellation is the starting point of the simulation studies in this chapter. As mentioned, the Swarm mission is an approved satellite mission of ESA, which aims at the global determination of the outer, inner and lithospheric magnetic field of the Earth as well as the temporal evolution of the inner and outer field. Swarm is scheduled to be launched in 2012 and is expected to give new insights into the Earth's interior and climate. More details about the mission can be found e.g. in (Olsen *et al.* [2007]). The Swarm constellation consists of two low orbiting satellites (Swarm A and B) and a third one at higher altitude (Swarm C). The two lower satellites will fly initially in a circular orbit at 450 km altitude, which is similar to the orbit altitudes of CHAMP and GRACE, while the third satellite will fly at 530 km. As a result of different altitude and slightly different inclination (87.4° for Swarm A/B and 88° for Swarm C), the orbital plane of Swarm C will change with time with respect to the orbital planes of A and B (Figure 4-4, Olsen *et al.* [2007]). Each of these three satellites carries onboard a GPS receiver and an accelerometer. They make it possible to do precise continuous 3D positioning and to separate gravitational from non-gravitational forces. Thus the set-up is comparable to three single CHAMP-like gravity solutions. Moreover, thanks to spaceborne differential GPS, one can determine the relative position vectors between these three satellites. These GPS baselines can be used as observations for gravity field determination and they are expected to bring an improvement against the single solutions, as the relative positions can be determined with an accuracy about one order of magnitude higher than the absolute positions of the individual satellites. The absolute GPS position accuracy for CHAMP is about 2-3 cm and the relative position of GRACE -based on GPS only- has been reported to be of mm-accuracy (Visser, 2006). Based on these performances, it is expected that the same accuracy of the relative positions can be achieved for the Swarm mission as well.

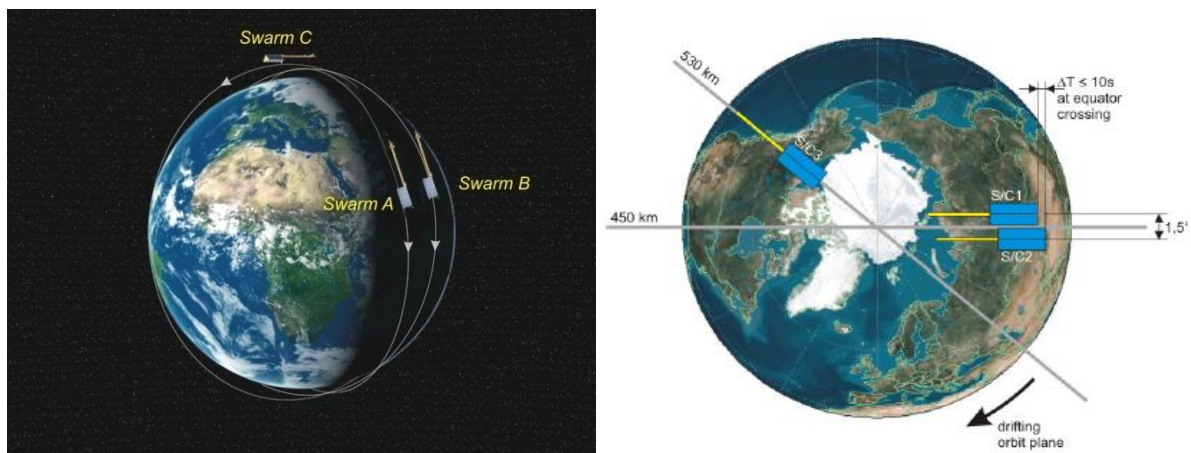


Figure 4-4 The Swarm constellation (Olsen *et al.* [2007])

Swarm provides two possible baseline measurements: the cross-track A-B baseline and the oblique A-C baseline, as described in section 2.2. The two lower satellites are designed according to 2 requirements: 1) Swarm B has a shift of 1.4° in longitude direction from Swarm A; 2) Swarm B has a time shift between 2 and 10 seconds to Swarm A within 60 days and the maximum time difference between Swarm A and Swarm B when crossing the equator shall be 10 seconds (Olsen *et al.* [2007]), in this way the collision at poles will be avoided. Figure 4-5 a) shows the changing of the scalar distance between A and B at 450 km for 1 day. As seen from the picture the distance varies from about 10 km at pole region to about 180 km at the equator. Although the distance between these two satellites changes with time for each revolution, the measurement direction remains cross-track throughout the mission for this A-B baseline. In contrast, both distance and geometry change strongly

with time for the baseline A-C. Figure 4-5 (b) plots the scalar distance between A and C for about 7 days from the mission start. As seen the distance can change from about 100 km to about 14000 km. Besides the changing scalar distance, the measurement direction of this baseline also changes with time: it can be radial, along-track or not possible at all (Figure 4-5 c)). This changing geometry makes it not possible to have a steady long-term observation with the A-C baseline.

To form a baseline measurement with the desired accuracy as given in Table 2-1 it is necessary to have 5-6 GPS satellites in common view. This criterion is fulfilled by A-B baseline, but obviously not always for A-C as they can be placed on the opposite sides of the Earth. Based on this a threshold of about 5000 km for the longest baseline is introduced in the simulator, which disregards the epochs where relative position between A and C is too large to have the required number of GPS satellites in common view. Besides that, as introduced in the simplified error analysis, the advantage of the baseline over the absolute GPS measurement for single satellite, i.e. the increased accuracy, will be lost if the relative velocity between two satellites is too large. Due to the changing geometry there is large amount of epochs where the relative velocity between A and C is so large that the advantage of GPS baseline cannot be guaranteed anymore. The above mentioned threshold is also approximately equally effective to a threshold of 5000 m/s for the largest baseline velocity, which ensures that the assumed accuracy level can be achieved for the baseline A-C. By applying the threshold there are in total about 23% of all the epochs qualified for forming the A-C baseline measurement with pre-defined accuracy. Later on in the hydrology recovery simulation details about the epochs in each month where the A-C baseline can be formed will be given for the entire simulation period of 2 years.

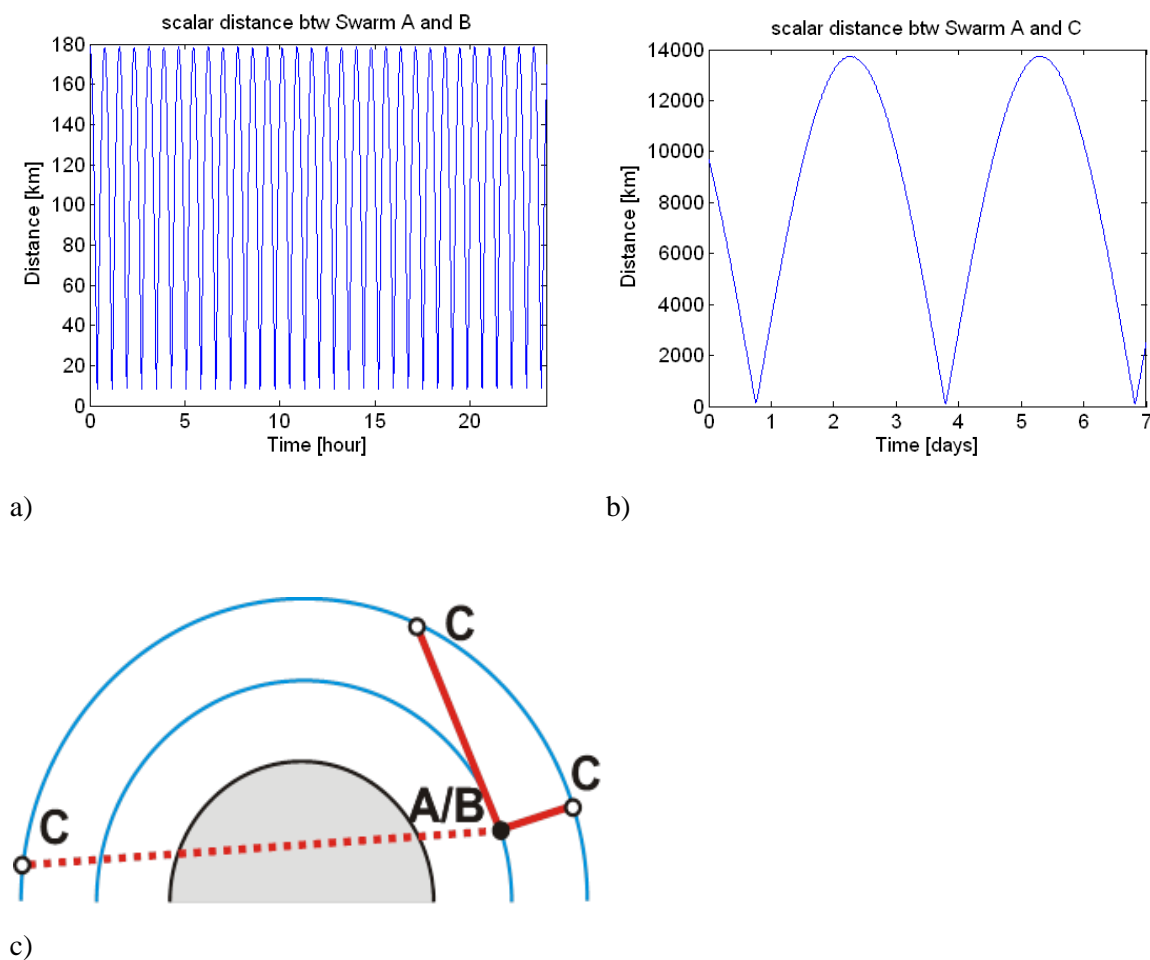


Figure 4-5 Scalar distance between Swarm A and B (a), scalar distance between Swarm A and C (b), the changing geometry of baseline A-C (c)

4.2 Introduction to simulated constellations

The Swarm constellation is the starting point for further simulations. Based on the Swarm constellation, the simulation is extended and also other constellations and measurements are simulated. These include e.g. a GRACE-like constellation and the assumption of a K-band measurement system. To sum up, the following constellations are simulated:

- Swarm constellation. The orbit height is 500 km for Swarm C and 350 km for Swarm A/B in the simulation. For this constellation the single satellite (e.g. Swarm A) as well as the baseline measurement A-B and A-C will be discussed (the baseline B-C is not included, because it is linearly dependent on the combination of A-B and A-C and does not provide additional information). The orbit altitude corresponds approximately to the status of the real Swarm mission after 3 years (Olsen *et al.* [2007]), as in the reality the orbital heights of Swarm A/B and Swarm C will decrease due to friction in the upper atmosphere from 450 km respectively 530 km down to 350 km respectively 500 km within the first three years. Since there is no atmospheric drag included in the simulator, the lower altitudes of 350 km and 500 km are selected as a mean of the planned mission duration of five years. The lower altitude will of course slightly increase the resolution of the recovered gravity field model with respect to what one can expect at the beginning of the mission. The orbit plane of C is set to be identical with that of A/B at simulation start, in order to study the change of the A-C baseline from mission beginning. This constellation, entitled *Swarm*, will only make use of GPS observations. The constellation consists of the three satellites A, B and C, as shown in Figure 4-6.
- A GRACE-like constellation. The term “GRACE” in this paper does not refer to the real GRACE mission. It is a GRACE-like constellation of 2 satellites in leading-following formation. Swarm A is considered as the leading satellite, a satellite A1 which is following about 200 km behind Swarm A on the same orbit is regarded as the second satellite, see also Figure 4-6. The K-band measurement is simulated by making use of equation (2.37) in section 2.2. In this paper this constellation is called *GRACE* short for “GRACE-like constellation”.
- A pendulum constellation with K-band measurement. In addition to the GPS-based Swarm A-B baseline measurement, the same constellation with an inter-satellite link of K-band type is simulated. This allows studying the potential of such a constellation for future missions. This scenario will be called *pendulum* in order to distinguish from the Swarm A-B GPS baseline.
- A 3-satellite-constellation. This constellation combines the above mentioned GRACE and pendulum constellations and thus consists of satellites A, A1 and B. K-band type inter-satellite links are simulated between A-A1 and A-B. This constellation is entitled *tandem/pendulum*.

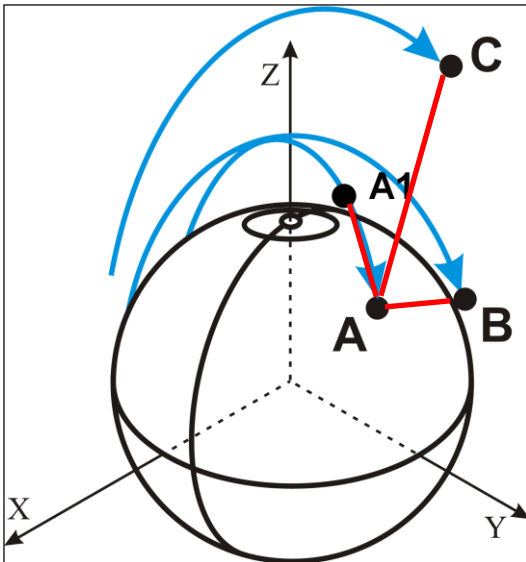


Figure 4-6 Simulated constellations, inter-satellite links marked in red.

4.3. Static field recovery

In this section it is attempted to recover the static gravity field, according to equations (2.14) and (2.15), where all time variable effects are assumed to be known such that their effect can be removed by integration of the corresponding accelerations along the orbit. This removal process will be called reduction in the following. In section 4.3.1 the results from error-free simulations are presented. The discrepancy between the input gravity field model (used for orbit integration) and the recovered output field are used as estimates of the numerical integration errors, which are introduced by performing the reduction process, i.e. by integrating the accelerations of time variations along the orbit. The size of the error depends on the characteristics of the accelerations, on the sampling interval and the chosen integration algorithm. In the simplest case, one might substitute the integration by a summation of the discrete values given along the orbit. It will be investigated how accurate this simple algorithm is and how that relates to the accuracy level which can be expected from the different satellite constellations in reality, i.e., including observation errors, which will be shown in section 4.3.2.

4.3.1. Error-free simulation

In section 4.1 it was shown that the simulator is closed-loop. In addition, it is assumed here that all the temporal variations are perfectly known from models or measured by the onboard instruments. In this way it should be possible to remove these signals perfectly. Thus the remaining error from the error-free simulation with time variation reduction should solely contain the numerical error introduced by the integration of time-variable gravity accelerations, which is used for the reduction of non-conservative effects in the energy integral. For consistency the sampling rate stays here 30 seconds. The simulation is carried out for January of 2003. The static gravity field is computed from EGM96 complete up to degree and order 70. In the simulation it is to be recovered up to degree and order 70 in

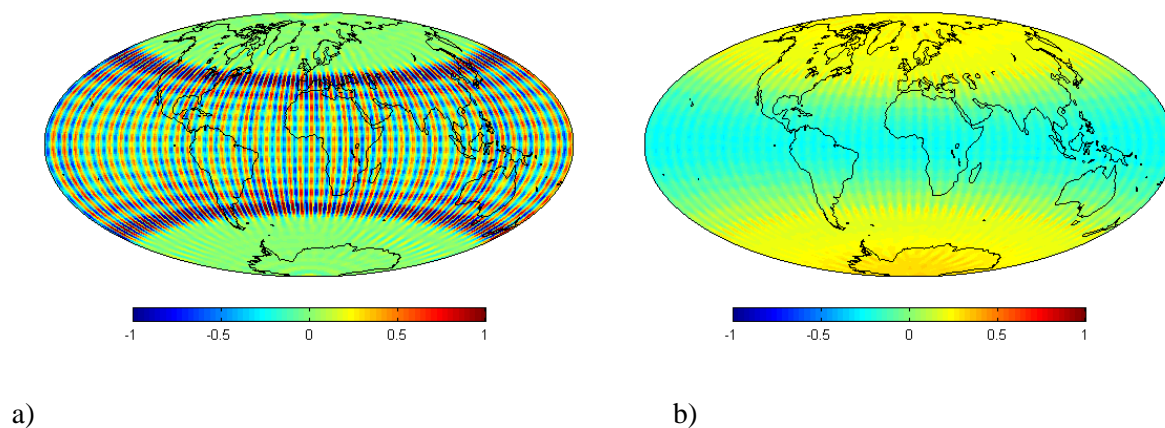
4.3 Static field recovery

the presence of time variations. The time-variable effects included are: ocean tides, atmosphere and non-tidal ocean variation (AO) and continental hydrology (H). The simulation conditions are listed in Table 4-2. Note that the hydrology model (LaD) is given originally in monthly resolution and it is interpolated into 6-hours interval to be consistent with the AO signal. The AOH signal together will be interpolated linearly between every 6 hours, as shown in Table 4-1. The ocean tide model FES2002 is included to degree and order 20.

Table 4-2 Simulation conditions

Temporal variations	Model	max. degree	Temporal resolution
Atmosphere/ocean	ECMWF-OMCT	70	6 hours
Hydrology	LaD	70	1 month/6 hours
Ocean tides	FES2002	20	---

Figure 4-7 shows the differences between recovered static field and the input EGM96 up to degree and order 70 without applying the reduction. The statistical values are summarized in Table 4-3. One can see that the time variations AOH and ocean tides together can contribute to more than 1 m geoid error in the case of Swarm A. For Swarm A-B a yellow-blue-yellow pattern is observable, which indicates that the zonal terms are not well determined. Among all the cases GRACE is affected least from the time variations. For all cases, reduction should be applied.



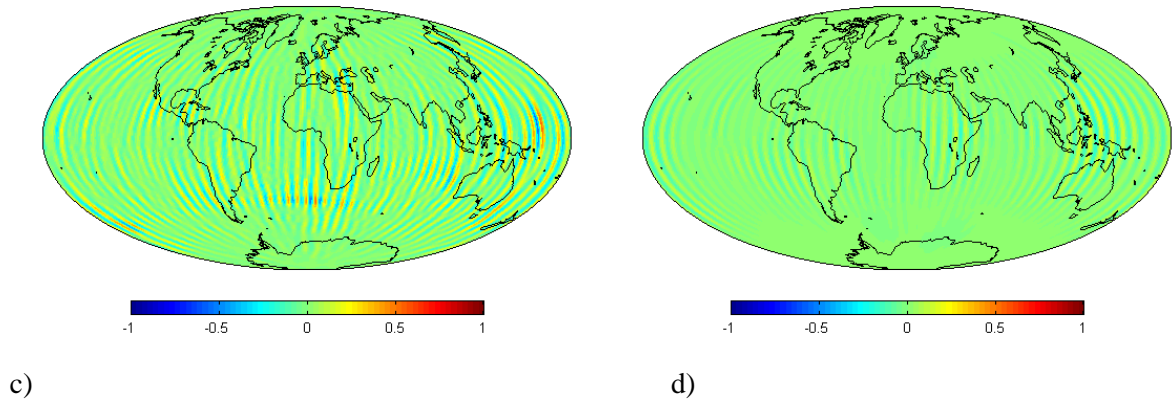


Figure 4-7 Geoid difference between recovered field and EGM96 without reduction, a) Swarm A, b) Swarm A-B, c) Swarm A-C, d) GRACE, all in [m]

Table 4-3 Geoid difference between recovered and original EGM96 field without reduction in [m]

Constellation	Max	Mean	Min	Sigma
Swarm A	1.62	2.93e-3	-1.66	0.39
Swarm A-B	0.35	0.078	-0.31	0.18
Swarm A-C	0.59	2.46e-4	-0.58	0.10
GRACE	0.19	9.09e-4	-0.21	0.037

After applying the reduction procedure, the differences between recovered fields and EGM96 are significantly reduced, as shown in Figure 4-8 and Table 4-4. It is obvious that the reduction procedure works for all cases. The error in geoid has decreased to below 1mm in all cases, which indicates that the major effect of the time variations is removed successfully. The same structure for Swarm A-B can be still observed, indicating that this error structure is not dependent on time variations but on the measurement direction itself. The remaining differences, as mentioned before, come from diverse numerical integration effects. While the orbit integrator selects internally a nearly arbitrarily fine integration step, the reduction procedure is only done every 30 seconds. Therefore the reduction only represents the signal at the epochs every 30 seconds but not the signal within the 30 seconds interval. If one can increase the sampling rate to e.g. 1s, the reduction procedure will work more effectively, which is proved by a separate test. To avoid redundancy this is not shown here. Furthermore, the integration is substituted by a simple summation of the discrete values every 30 seconds. A more accurate numerical integration algorithm can improve the results as well. By comparing the values in Table 4-4 with the error level derived from the simplified error propagation in section 2.2 (note that one needs to convert between potential and geoid), one can conclude that the reduction procedure works well enough despite the above mentioned numerical effects. It thus demonstrated that all effects of the temporal variations can be nearly fully removed, assuming that these signals are known or modelled accurately enough.

4.3 Static field recovery

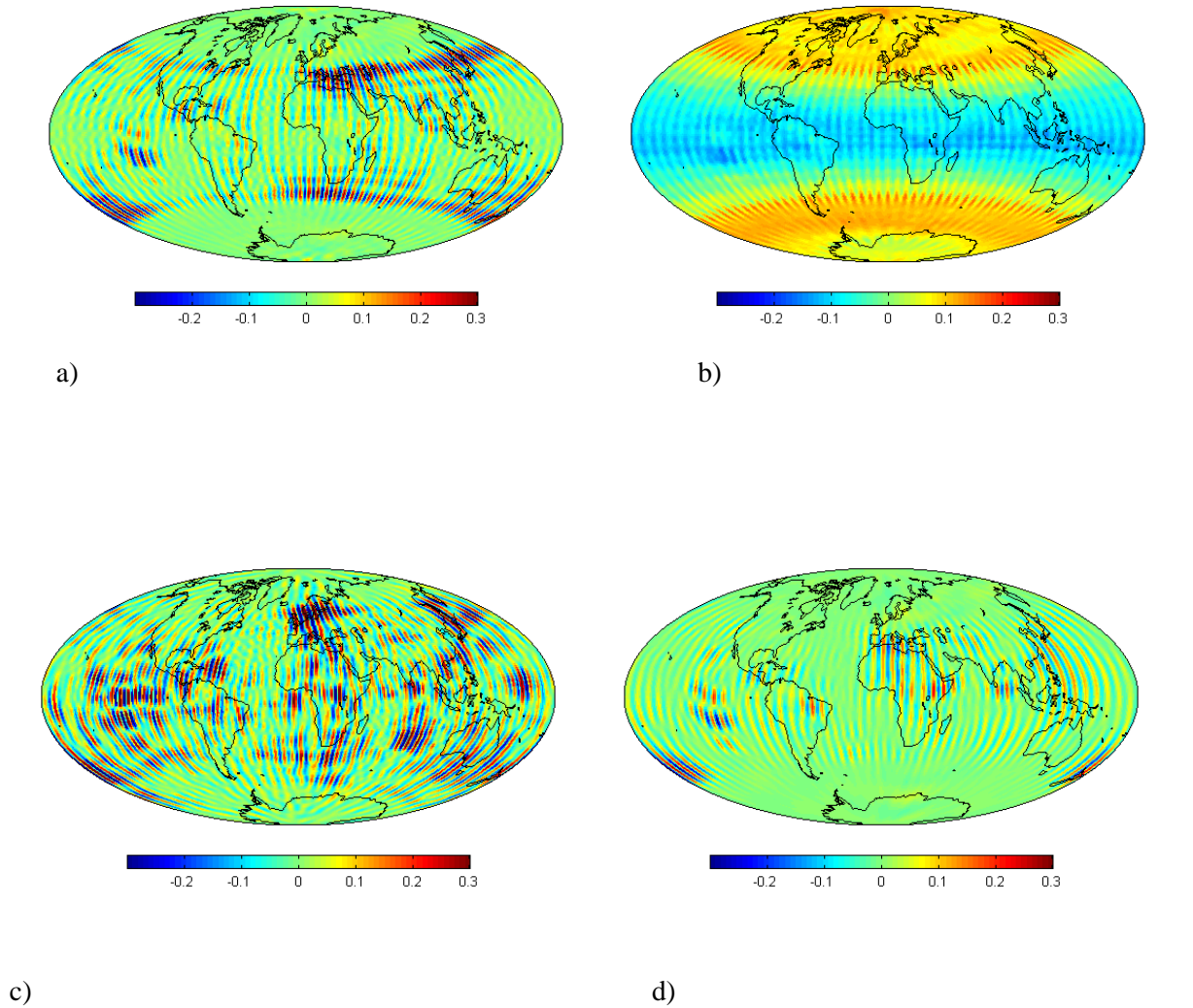


Figure 4-8 Geoid difference between recovered field and EGM96 with correction, a) Swarm A, b) Swarm A-B, c) Swarm A-C, d) GRACE, all in [mm]

Table 4-4 Geoid difference between recovered and original EGM96 field with reduction, in [mm]

Constellation	Max	Mean	Min	Sigma
Swarm A	0.39	2.21e-4	-0.40	0.070
Swarm A-B	0.18	0.027	-0.17	0.077
Swarm A-C	0.78	-1.80e-4	-0.70	0.10
GRACE	0.28	-4.88e-5	-0.33	0.04

It should be taken into account, that in the above simulation the temporal variations are perfectly known. This is not the case for reality, where there is always a difference between the true signal and the applied models or the onboard measurements. Then one can expect residuals between the true field and the recovered field, which might still introduce some long wavelength error characteristics, smaller than shown in Figure 4-7 and Table 4-3, though.

4.3.2. Full-error simulation

As shown in the last section, all temporal variation effects involved in this article can be effectively reduced for a static gravity field recovery, assuming that they are known accurately enough. In this section white noise is added to the simulated orbits and the noise level is listed in Table 4-5 below. The remaining simulation conditions are identical to those listed in Table 4-2. Additionally to the existing constellations, the pendulum and tandem/pendulum constellations are simulated. One combined solution, i.e. Swarm A combined with A-B, is presented as well.

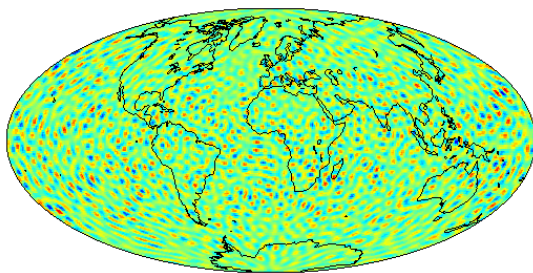
Table 4-5 Noise level for the simulation in [mm] and [mm/s]

	Abs. position	Abs. velocity	Rel. position	Rel. velocity
noise (σ)	10	0.1	1	0.01

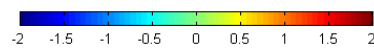
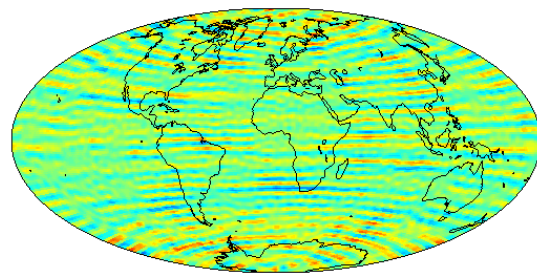
For each constellation a 1-month simulation is carried out for January 2003 and reductions are applied to remove the non-conservative impacts of the temporal variations. The recovered fields are then compared with EGM96 to degree and order 70 in terms of geoid height and also directly in potential coefficients. The geoid differences are plotted in Figure 4-9 and the statistical values of the comparison are listed in Table 4-6. Note the unit is given in meters. For convenience of description, all constellations are marked with numbers.

Table 4-6 Difference between recovered field and EGM96 in [m]

Constellation	Max	Mean	Min	Sigma
Swarm A (a)	1.87	-8.6e-3	-2.06	0.41
Swarm A-B (b)	1.57	0.04	-1.30	0.42
Swarm A-C (c)	2.02	-7e-4	-1.99	0.40
Swarm A+(A-B) (d)	1.23	-8.6e-3	-1.30	0.29
GRACE (e)	0.006	4.5e-6	-0.0057	0.0011
Pendulum (f)	0.015	1.03e-5	-0.015	0.0031
Tandem/pendulum (g)	0.0016	4.14e-6	-0.0016	3.76e-4



a)



b)

4.3 Static field recovery

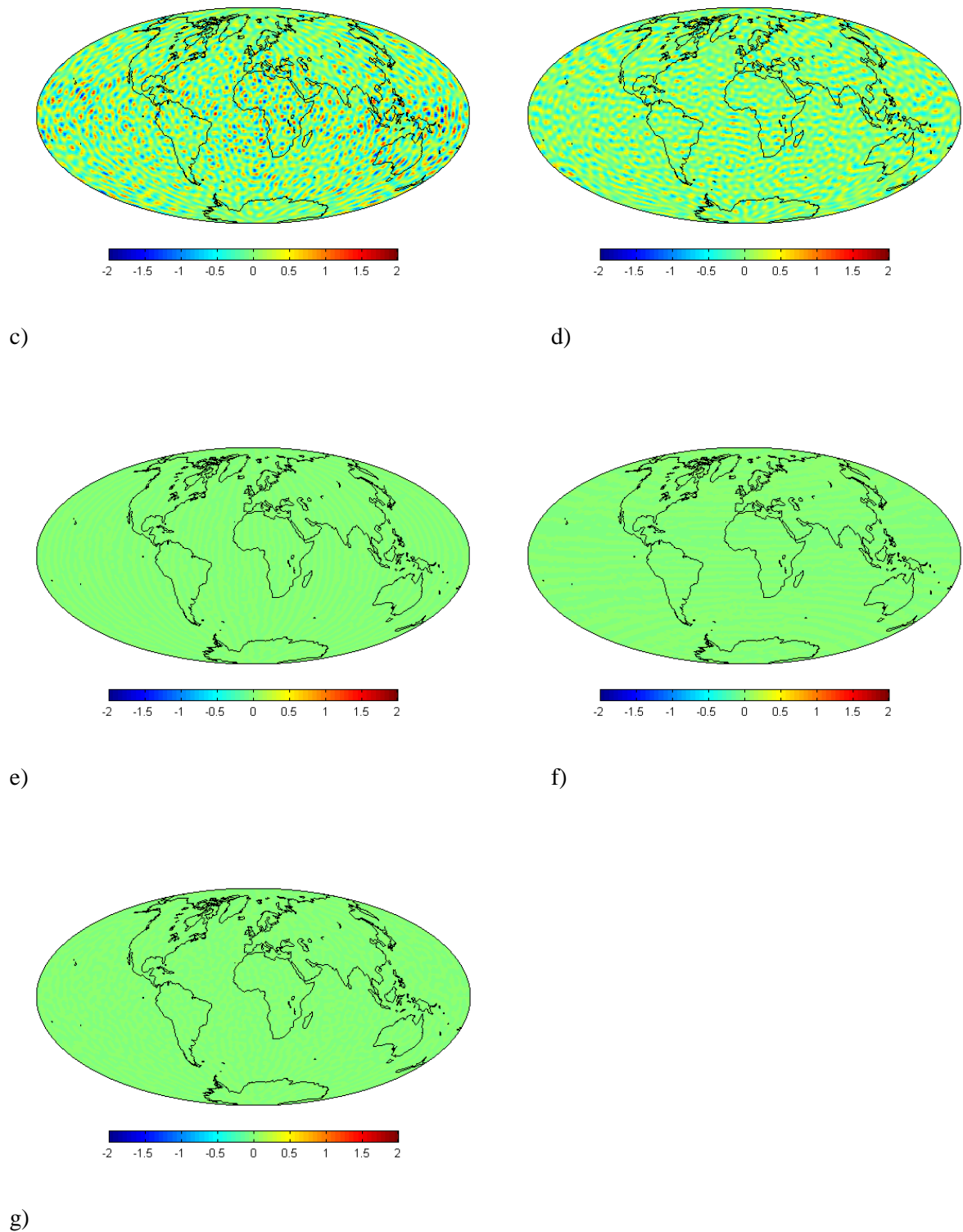
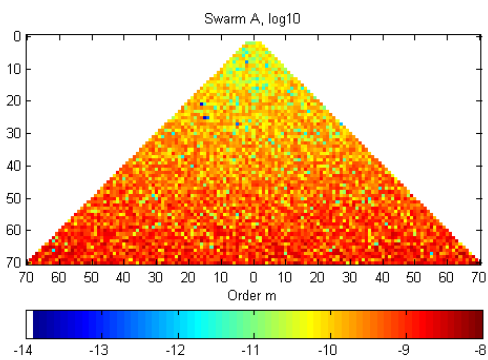


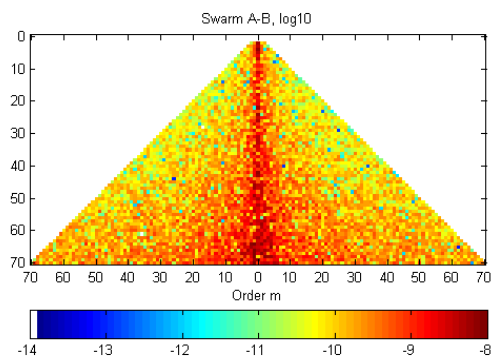
Figure 4-9 Geoid difference between recovered field and EGM96, with reduction, with noise, a) Swarm A, b) Swarm A-B, c) Swarm A-C, d) Swarm A+(A-B), e) GRACE, f) pendulum, g) tandem/pendulum, in [m]

From Figure 4-9 and Table 4-6 it is obvious that the constellations with K-band accuracy, i.e., case (e) to (g) offer an accuracy of about 100 times better than the GPS-only solutions, which meets the expectations from the error analysis in section 2.2. The single solution and the two baseline solutions show similar results (case (a) to (c)). Case (d) combines (a) and (b) and offers a slightly better result.

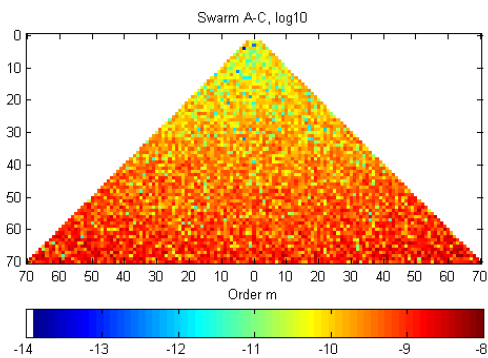
The comparison of the coefficients in the form of a triangle plot, Figure 4-10, gives basically the same information as the geoid plots comparison in Figure 4-9 and Table 4-6, however in spectral characteristics. The triangles reveal the different sensitivity of different constellations (note the different colorbar for GPS and K-band solutions). The cross-track constellations (b) and (f) are in general less sensitive to the zonal coefficients in the central column of the triangles, while the sensitivity to the sectorial coefficients is high. The opposite is true for the along-track constellation (e), with higher sensitivity to the zonals than to the sectorials. Although case (f) features a K-band and therefore offers much better overall recovery accuracy than (b), the zonal coefficients are still less well determined than the other coefficients. Thus the spectral sensitivity is independent from the accuracy of the measurement systems implemented but only dependent on the constellation. The best result is achieved by the tandem/pendulum constellation, which combines the advantages of along-track and cross-track observations and provides an isotropic error behavior with no preference to certain coefficients of the same degree. Among the GPS-only solutions, the combination case (d) takes advantage of both (a) and (b) and it is thus slightly better than both.



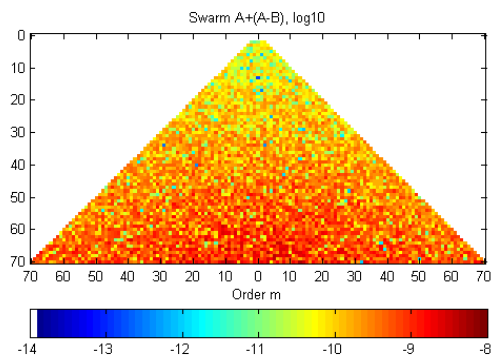
a)



b)



c)



d)

4.3 Static field recovery

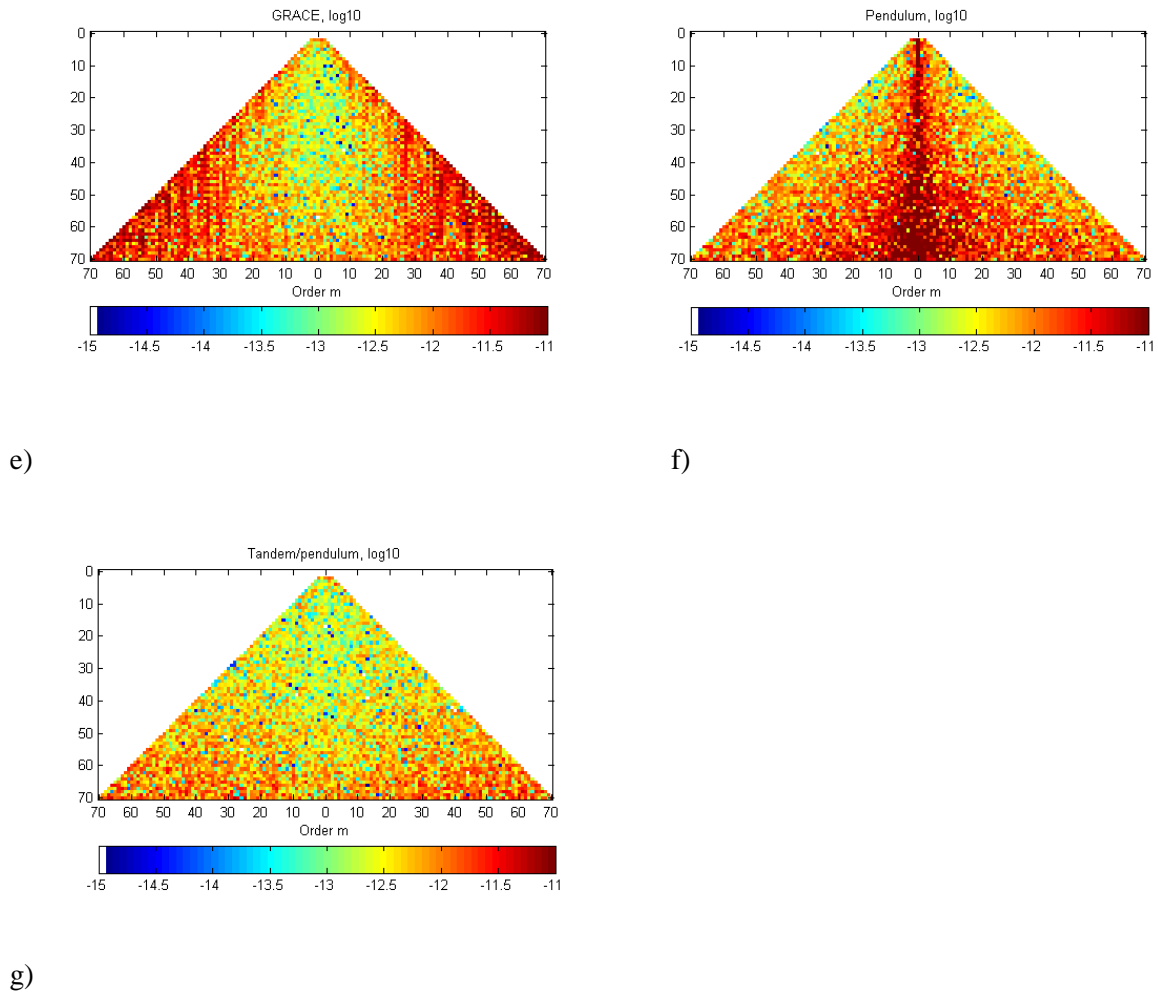


Figure 4-10 Comparison of the potential coefficients, a) Swarm A, b) Swarm A-B, c) Swarm A-C, d) Swarm A+(A-B), e) GRACE, f) pendulum, g) tandem/pendulum

The Swarm A-C baseline deserves a closer investigation. As described before the geometry of this baseline changes with time. The baseline contains along-track and radial components as long as the satellites move in the same orbital plane – otherwise there are cross-track components in addition (see also Gerlach *et al.* [2006]). As stated in section 4.2, by applying the threshold only about 23% of the data remain available. This number might be further decreased by the fact that the orbital planes of Swarm A and Swarm C drift apart from each other during the mission life time. Then it becomes evident, that also the distribution of the remaining epochs is not homogeneous, as most baselines can be formed, when the satellites are close to the poles. Due to different orbital velocities and drifting of orbit planes, the distribution of the remaining data points is not stable from month to month and for certain periods of the mission it will not be possible to have enough observation for gravity field recovery at all. For the considered month, however, the solution from the baseline A-C is acceptable.

Figure 4-11 represents the degree RMS plot of all constellations. The GPS-only solutions have a spectral resolution of about degree 70, which fits to the actual results achieved by CHAMP (Reigber *et al.* [2007], Sneeuw *et al.* [2003 b]). In general the spectral resolution will be increased when using relative observations along baselines, while the accuracy for the lower degree coefficients will be decreased as compared to a single satellite constellation like CHAMP. Constellations (e) to (g) are, as expected, about two orders of magnitude better than the GPS-only solutions. In order to see the full potential of constellations (e) to (g) for static gravity field determination the simulation would need to

be extended to degree and order 150 or more. Also note the decreasing RMS values when going from GRACE or a pendulum constellation to a pendulum/tandem combination.

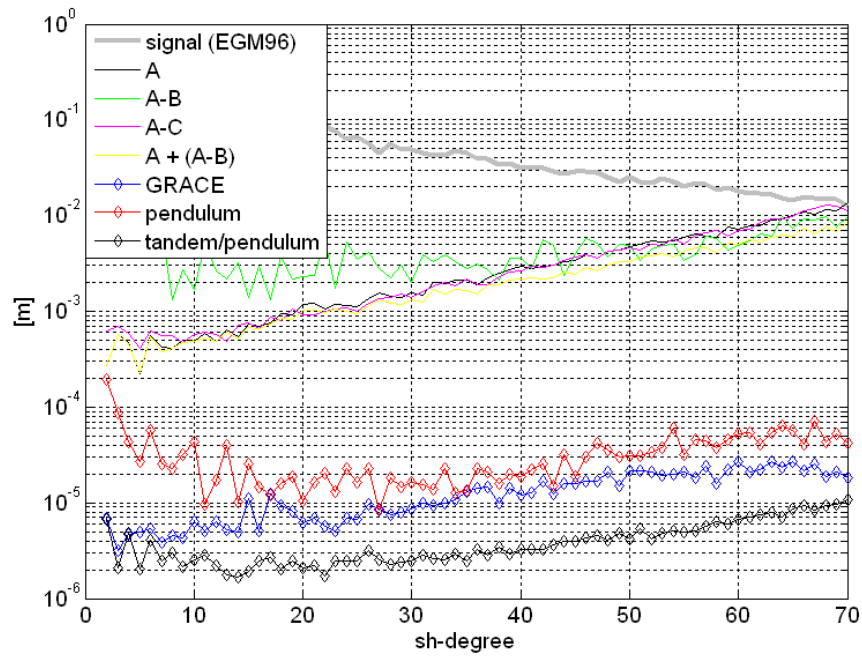


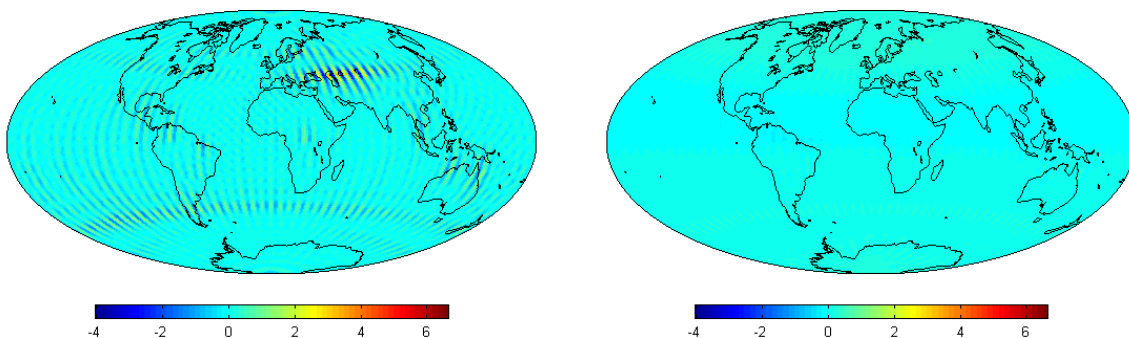
Figure 4-11 Degree RMS plot for static gravity field recovery

4.4. Aliasing investigation

Before attempting to recover the continental hydrology signal in section 4.5, the aliasing issue of the involved time-variable gravity signals should be discussed. Like for the real GRACE mission, the de-aliasing of atmosphere-ocean and ocean tide signals is assumed to be perfect, i.e. their impact is assumed to be fully removed from the observation equations. This assumption is close to be valid in few of the high quality of atmosphere-ocean models. This assumption is applied in the simulation here, as the de-aliasing products are exactly the time variations used in orbit integration. In the reality, however, this will not apply as there is always a difference between the de-aliasing products and the real mass variations. This issue will be shortly discussed in section 4.4.2. While the necessity of the de-aliasing of these fast-changing variations is well known and it is already implemented for the current GRACE mission, the temporal aliasing issue due to the unknown hydrology signal is not often discussed. This issue will be investigated in section 4.4.1.

4.4.1. Temporal aliasing for continental hydrology

Spectral analysis in section 3.2 shows that the strongest signal contents of the hydrology model LaD are annual (1 cpa) and semi-annual (2 cpa) frequencies. The remaining frequencies are much weaker, e.g. the 2-monthly frequency (6 cpa) is roughly 1/100 of the signal strength of the annual component. This indicates that one can expect the signal strength of sub-monthly frequency to be relatively small, which should lead to a relatively small temporal aliasing effect. Here the aliasing investigation is based on a 1-month error-free simulation for January 2003. Within this month the hydrology signal is assumed to be changing linearly, which is realized by linearly interpolating the two neighboring months, i.e. January 2003 and February 2003. The hydrology signal is superimposed to the EGM96 static field to degree and order 70. The recovered field should correspond to EGM96 plus the mean hydrology field over this month. The differences between the recovered field and the input field are caused by aliasing effect and theoretically also errors of non-conservativeness. In a simulation, the latter can be calculated exactly by making the difference between the integration of the accelerations and the temporal potential computed directly from the time variation coefficients, as shown in section 3.5. Thus the time series of potential values derived from the energy integral can be corrected for this error before doing the analysis. When doing so, the results barely changes, which suggests, that the error of non-conservativeness can be neglected for moderate temporal variations as those caused by linearly changing hydrology. This supports the conclusions in section 3.5. Therefore, the errors shown in Figure 4-12 and Table 4-7 can be regarded to be solely aliasing effects.



a)

b)

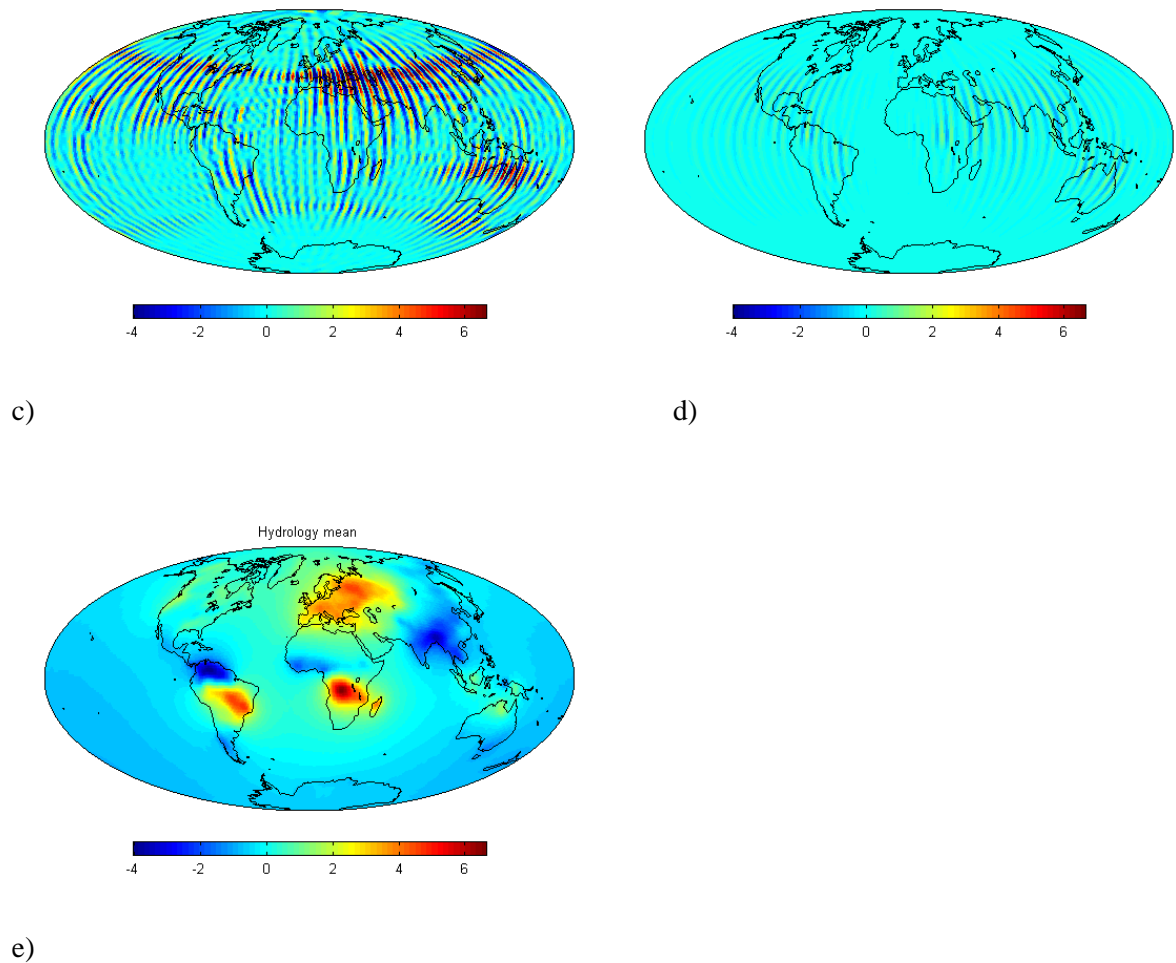


Figure 4-12 Aliasing effect from hydrology in [mm], a) Swarm A, b) Swarm A-B, c) Swarm A-C, d) GRACE, e) H mean

Table 4-7 Aliasing effect from hydrology in [mm], d/o 70

Aliasing effect				
Constellation	Max	Mean	Min	Sigma
Swarm A (a)	3.63	-0.02	-3.80	0.41
Swarm A-B (b)	0.32	0.05	-0.32	0.12
Swarm A-C (c)	10.75	0.03	-11.36	1.49
GRACE (d)	1.49	-0.01	-1.49	0.22
Signal				
	Max	Mean	Min	RMS
H mean (e)	6.60	0.02	-4.06	1.02

Figure 4-12 a) to d) show the aliasing effect from hydrology for different constellations and e) gives the mean signal of the simulated month. The worst case is the A-C baseline, where the standard deviation is as large as 1.5 mm, which is larger than the signal itself. For other cases the standard deviations of the aliasing error are less than 0.5 mm, which is about 50% of the signal. The degree RMS plot for Swarm A, Figure 4-13, shows that the aliasing error is larger than the LaD signal after about degree 40. This indicates that the aliasing effects prevent the detection of the time-variable

4.4 Aliasing investigation

hydrology signal above about degree 40 even for a purely linear trend in an error free simulation. As the errors in the higher degrees will contaminate the recovery seriously, a low-pass filter should be introduced with cut-off between degree 30 and 40. As an example, the aliasing error for Swarm A gives a standard deviation of 0.0119 mm (max = 0.0741 mm, mean = -6.3024e-04 mm, min = -0.0657 mm) in geoid height, which is only about 1% of the signal strength of hydrology. Besides, the hydrology signal is concentrated on the lower degree and orders, while the signal strength of higher degrees is quite weak, as discussed in section 3.2. Based on these results, all input models (static field and hydrology) in the 2-years simulation in section 4.5 will be limited to degree and order 30.

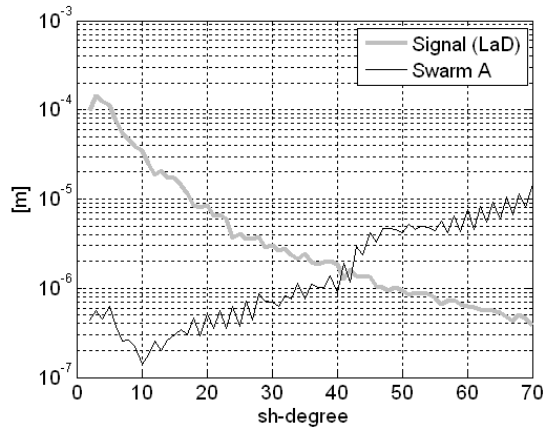


Figure 4-13 Degree RMS of Swarm A

4.4.2. De-aliasing discussion for AO and ocean tides

For the current GRACE mission the rapid-changing atmosphere-ocean signal is removed by using the best available models. This so called de-aliasing process does not solve the insufficient sampling in time and/or space, but tries to exclude the variations which may cause aliasing. So far the de-aliasing process is regarded as error-free, i.e. one assumes the de-aliasing product perfectly removes the impact of the AO signal. As mentioned before, this assumption is not perfectly true in reality, due to the fact that there is always a difference between the models used for such process and the reality. In a recent study (Zenner *et al.* [2010]), the error has been introduced into the de-aliasing product to investigate if this helps to obtain a more accurate GRACE gravity field time-series. The conclusion was that for the currently achieved GRACE accuracy level, atmospheric model uncertainties do not play a prominent role in the error budget of GRACE gravity field solutions. This conclusion should also hold for the GPS-only measurement, as it has even a much higher error budget than the current GRACE mission.

Zenner *et al.* [2010] also pointed out that if the predicted accuracy of GRACE were achieved, the uncertainties in atmosphere models could have a real effect on the recovered gravity field. This conclusion is supported by other studies, e.g. Wiese *et al.* [2008], where satellite constellations are simulated with improved inter-satellite laser ranging instrument and drag-free system. There the difference between two GRACE AOD models is regarded as the de-aliasing error and the results show that once this error is considered, all the simulated formations determine the gravity field fairly equally. The advantage of the 4-satellite-Cartwheel formation, which achieves an accuracy of one order of magnitude better than other constellations when the de-aliasing error is not considered, disappears as the recovery is affected by the de-aliasing error. Over all, these studies suggest that for a future mission with an accuracy level better than the current GRACE mission, the de-aliasing error of atmosphere-ocean signal must be considered as it will have a significant impact on the recovered field.

Similar to the atmosphere-ocean signal, the ocean tides signal is subtracted for de-aliasing by using the currently available tides model for the current GRACE mission. This is accomplished by using e.g. CSR4.0 (Eanes and Bettedpur [1995]), NAO99 (Matsumoto *et al.* [2000]) or EOT08 (Savcenko and Bosch [2008]). All these models are assumed to be error-free de-aliasing products, i.e. they are assumed to represent perfectly the real behaviors of the ocean tides. This assumption cannot hold fully in reality and thus the error of such ocean tide de-aliasing product will remain in the GRACE solution and corrupt the recovered gravity fields. Han *et al.* [2004] have investigated the time-variable aliasing effects of ocean tides on monthly mean GRACE gravity fields and it was found that the model error in the S2 constituent causes larger errors than the measurement noise for the recovered coefficients below degree 15. The errors in K1, O1 and M2 constituents can corrupt the harmonic coefficients of order 30 to 36 and all corresponding degrees, but they can be reduced to below the measurement noise level by monthly averaging. Visser *et al.* [2010] have investigated the ocean tides aliasing effect for future space-borne gravimetric satellite constellations. There the observation of gravity changes due to continental hydrology has been defined as a test case for assessing the impact of the ocean tide errors. It was found that the ocean tides aliasing error strongly depends on the satellite constellation and the choice of orbital parameters. The error can be reduced by increasing the temporal sampling of the mission, which can be achieved by appropriate constellation flight. For a future mission with laser-based measurement system, the aliasing error of ocean tides will have more significant impact and therefore it must be treated appropriately to avoid serious corruption of the recovered gravity field. More discussions on this issue can be found e.g. in Ray and Luthcke [2006], Seo *et al.* [2008a,b] or Moore and King [2008].

An attempt will be made to recover the continental hydrology in the next section. There the key question is whether the GPS-only based measurement has the potential for such a recovery at all. For the error budget of such measurements, the above mentioned de-aliasing error will not play an important role. Thus the de-aliasing error for atmosphere-ocean and ocean tide is not included in the simulations in section 4.5.

4.5. Time-variable hydrology signal recovery

In this section an attempt is made to recover the hydrology signal with different constellations, including GPS-only and K-band measurements. The former is more of interest, while the latter should confirm the results already achieved by GRACE. Ditmar *et al.* [2009] have concluded that the insufficient GPS accuracy is the key limiting factor for GPS-only measurement to detect the temporal variations. Thus the key question is, if it is possible at all to obtain temporal variations with GPS-only measurements, e.g. with the Swarm mission. In order to investigate this issue, a 24-month simulation is carried out here, aiming at the recovery of the hydrology signal represented by the LaD model. Other time variations such as atmosphere-ocean signal and ocean tide signal are assumed to be fully reduced and therefore they are not included in this section. Furthermore, as discussed in section 3.5 it is acceptable to consider the hydrology to be static within a month. Based on these considerations, the hydrology model is superimposed to the static EGM96 at the beginning of each month. The sampling rate applied here remains 30 second in order to be consistent with previous simulations and to reduce the computation effort. Orbit noise is applied here, where the noise level is the same as in Table 4-5. The highest degree and order for recovery is set to be 30, as discussed in section 4.4.1. The recovery results are shown below.

4.5.1. General results

First the degree RMS plots of two different months are presented in Figure 4-15, where the top panel represents May 2003 and the bottom panel October 2003. The figure shows that all K-band constellations can recover the hydrology variations to about degree and order 20 to 30. Again the tandem/pendulum combination benefits from the isotropic error behavior and shows the potential of a recovery even beyond degree 30. It is also obvious that in general it is impossible to recover hydrology signal with GPS-only based constellations. Ditmar *et al.* [2009] claims that the GPS errors should be reduced 30-100 times in order to catch some hydrology signal. This number meets the previous error analysis in section 2.2 that the K-band range observation is about 100 times more accurate than GPS positioning.

As described before, the Swarm A-C baseline changes with time and the quality of its solution varies from month to month. As seen from the figure, the A-C baseline solution offers a good quality for October. It is comparable to the combined solution A+(A-B), where the single solution A is combined with the baseline solution A-B. But for May it is orders of magnitude worse than the other solutions. In fact there are only 3 months in the total simulation duration of 2 years (January, February and October of 2003), where A-C offers acceptable results. During all remaining months the quality is worse than other constellations.

Figure 4-14 shows the ratio of epochs usable for forming the A-C baseline measurement for gravity field recovery during the 2-years period. It is obvious that as the orbit plane of C drifts away from that of A/B, the percentage of epochs where A-C baseline observation can be formed decreases with time. In December 2004 observation of the baseline is limited to only about 9% of the total data in this month. Furthermore, the epochs, where it is possible to use A-C baselines as observations, are spatially not evenly distributed. As the orbit planes drift from each other the A-C baseline can be mostly formed around the pole regions. This makes it even harder to have a steady and spatially evenly distributed long period observation using the A-C baseline. This special geometry between A and C should always be investigated before one attempts to use A-C baseline observations to recover the gravity field. However, if it turns out, that determination of the baselines with acceptable accuracy is not limited to short baselines with enough common GPS satellites, one should consider using all epochs with proper weighting. This issue will be discussed later.

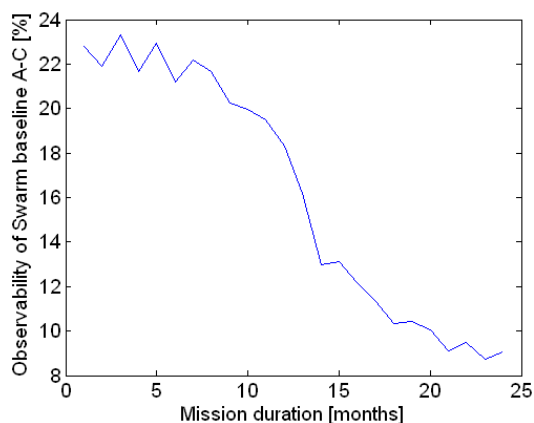


Figure 4-14 Observability of Swarm A-C baseline during 2 years

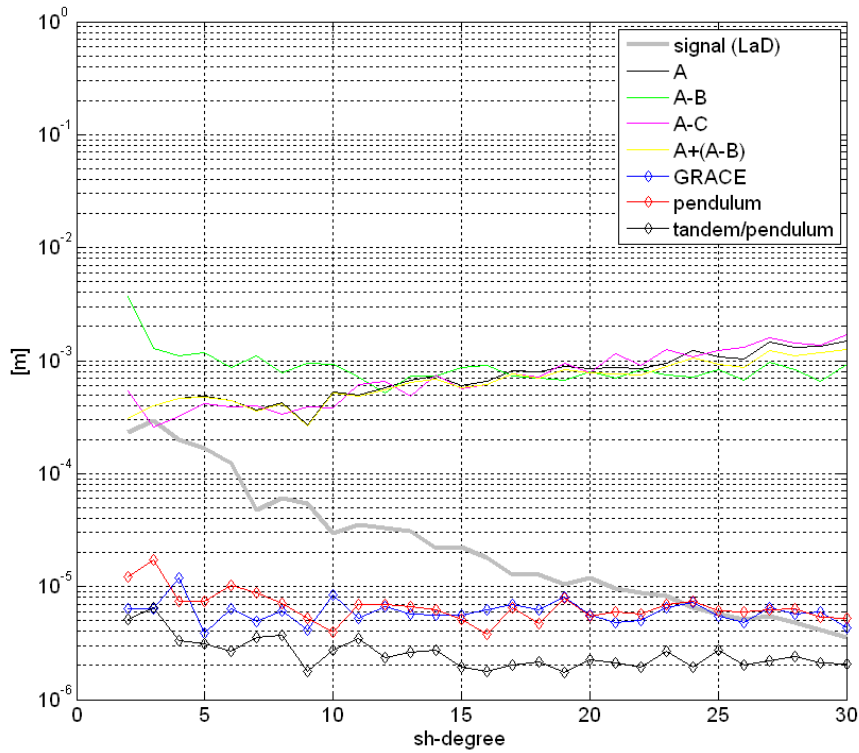
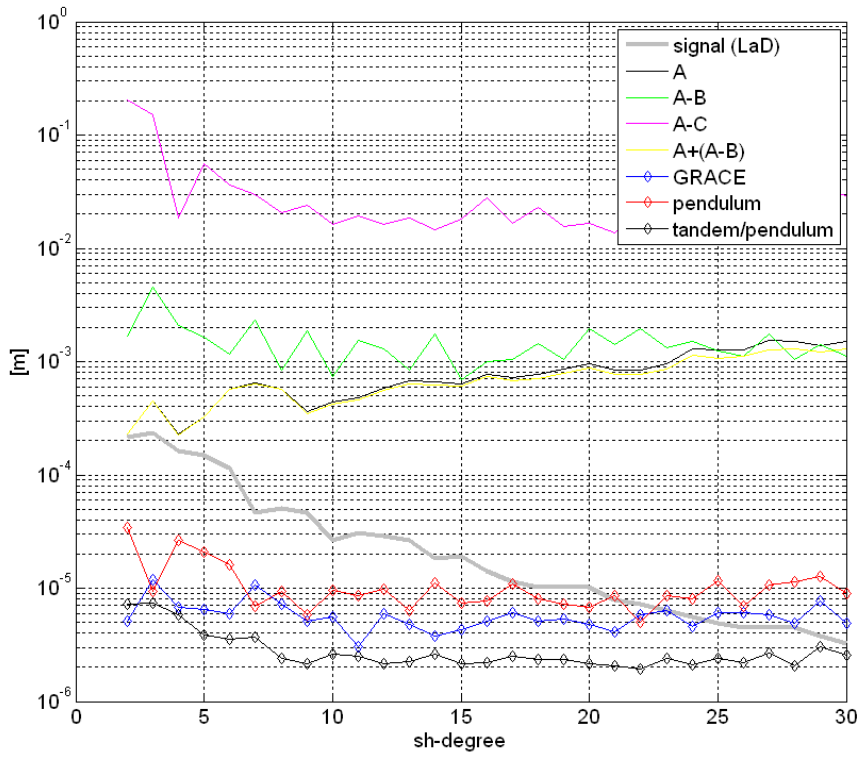


Figure 4-15 Degree RMS for May (top panel) and October (bottom panel)

4.5 Time-variable hydrology signal recovery

Reigber *et al.* [2003] have combined CHAMP data with four SLR satellites, namely Lageos 1, Lageos2, Stella and Starlette, to recover the C20 and C30 coefficients and found that the CHAMP data may stabilize the time series estimation process in general. A direct answer to the question, if CHAMP can recover these terms, was not given, as the length of the data was too short (63 1.5 day arcs). They suggested to process more than 1 year CHAMP data to further investigate this issue. Following this conclusion, an attempt is made here to recover the coefficients C20 and C30 of the LaD model from Swarm stand-alone simulated data, which is shown in Figure 4-16 to Figure 4-18. The corresponding statistical values are listed in Table 4-8. Seen from these figures, all the single solutions from Swarm A, B and C seem to be able to determine the C20 and C30 coefficients. Both the amplitude and the phase fit well to the LaD model, although the recovery errors can be more than 50% of the signal for single satellite solutions, as shown in Table 4-8. A large part of the recovery error is due to a few large deviations. The baseline solutions, however, are generally poor. This supports the expectation, that relative (or difference) measurements increase the resolution in the high degrees, while the accuracy is decreased for the very low degrees. The baseline A-B solution gives poor quality in the first 10 months while the A-C solution is extremely bad in the last few months. As a result, the recovery errors of A-B and A-C baselines are orders of magnitude larger than the signal itself, as can be seen from Table 4-8. Only the combined solution A+(A-B) gives satisfactory results, which is quite similar to the Swarm A solution. However, it seems that except C20 all other degree 2 terms, i.e. C21, C22, S21, S22, are poorly determined, see Figure 4-19 and Table 4-8, where the recovery errors from single satellite solutions can be 3 to 6 times larger than the signal itself. This may explain why it seems to be impossible to recover the very low degree part of the hydrology signal with Swarm from the degree RMS plots (Figure 4-15). One should also notice that the RMS represents a global mean value and thus only roughly reflects the possibility for recovery of spatially limited signal structures (like those of continental hydrology).

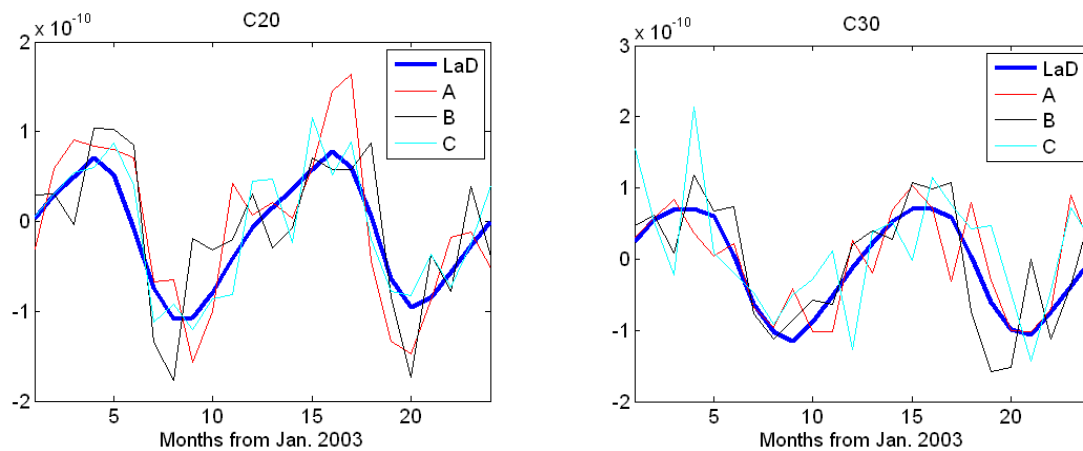


Figure 4-16 C20 (left) and C30 (right) determined from Swarm A, B and C

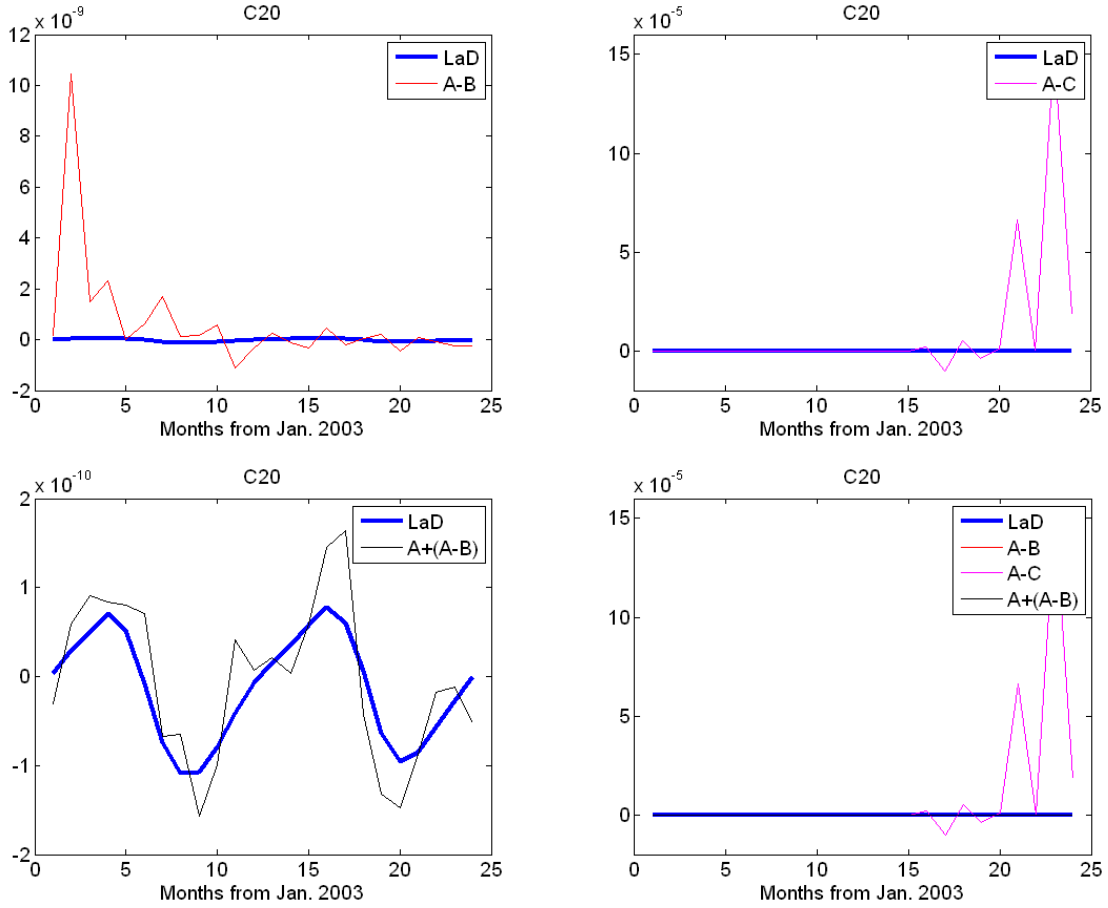
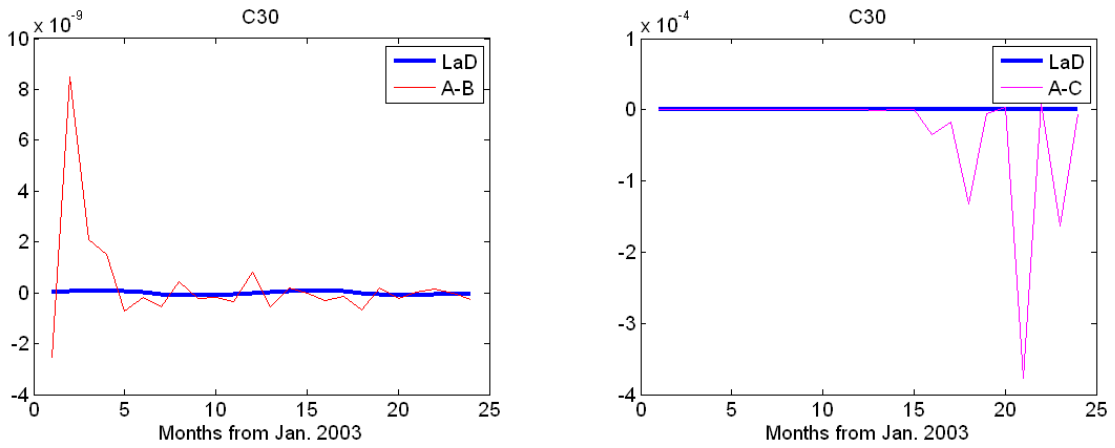


Figure 4-17 C20 determined from baseline solutions



4.5 Time-variable hydrology signal recovery

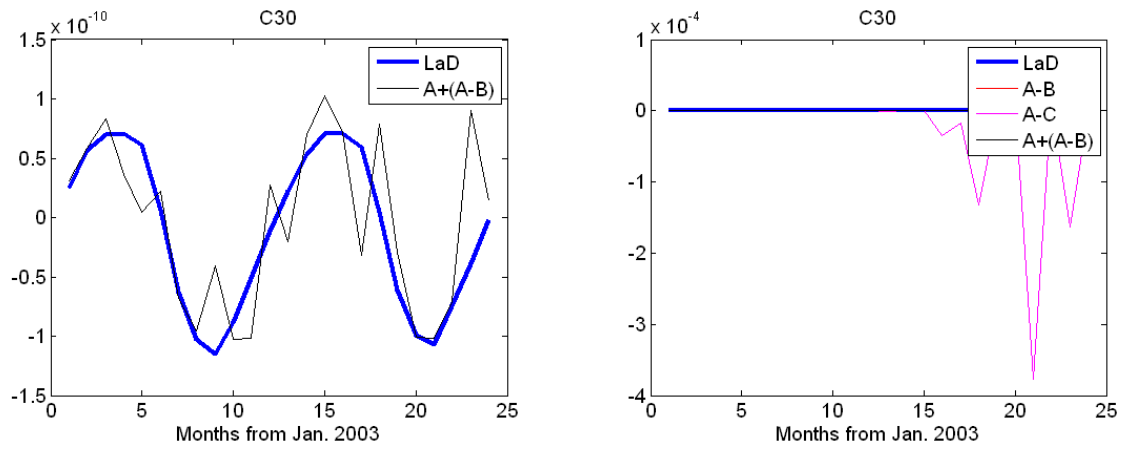


Figure 4-18 C30 determined from baseline solutions

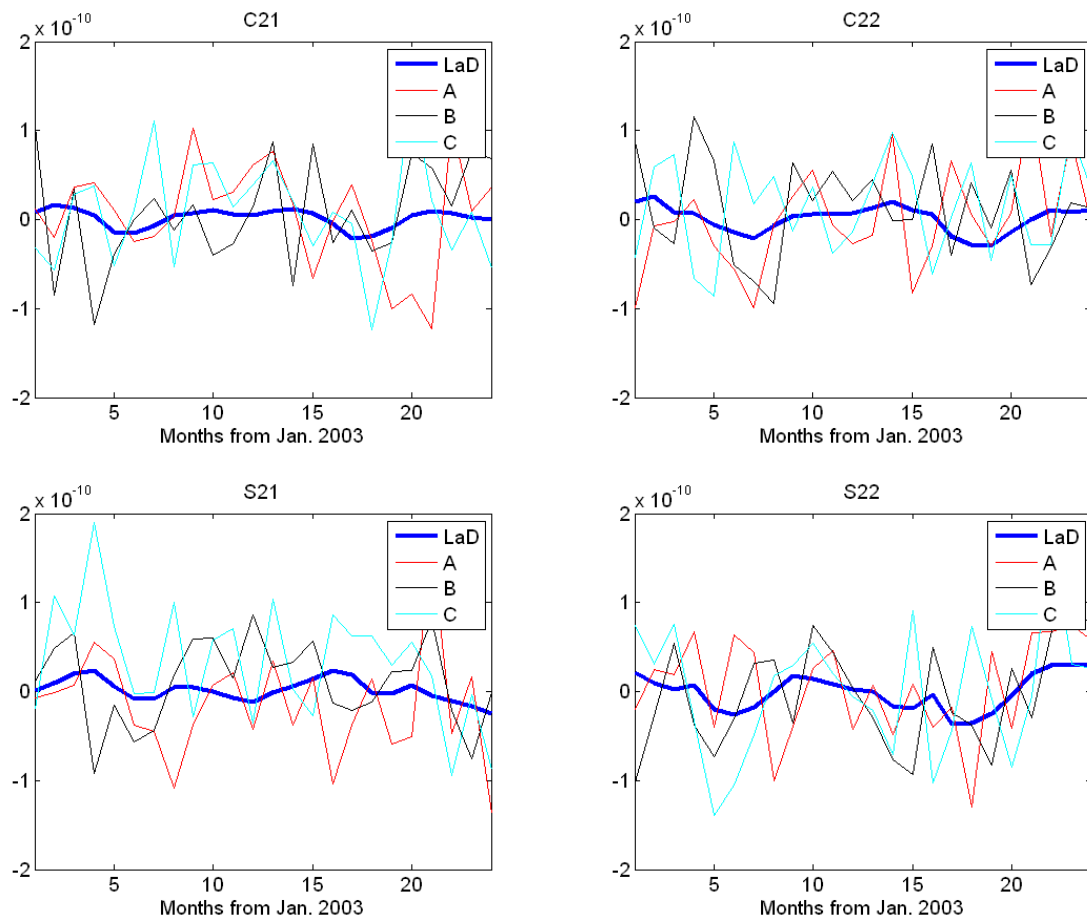


Figure 4-19 Determination of C21, C22, S21, S22 from single satellites

Table 4-8 Single coefficients recovery from Swarm constellation

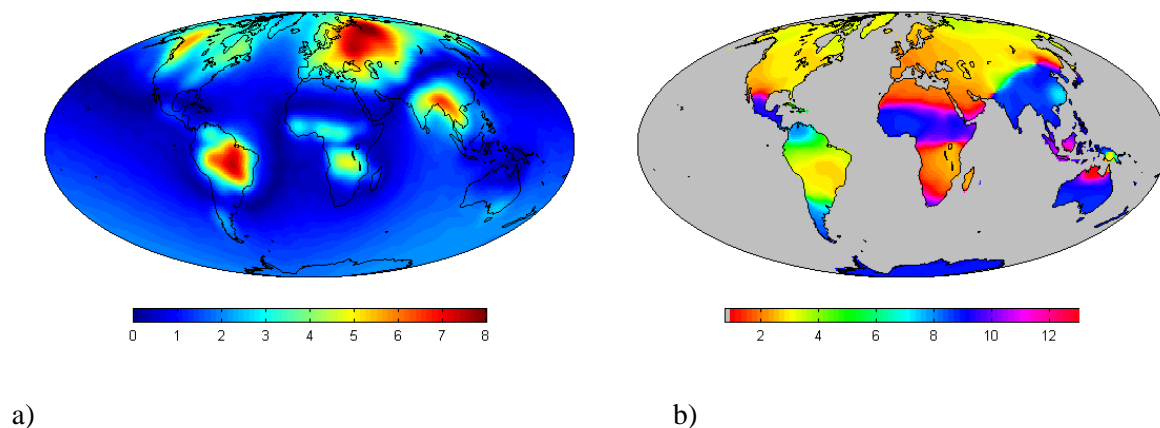
Signal strength				
	Max	Mean	Min	RMS
C20 (LaD)	7.83e-11	-1.24e-11	-1.08e-10	6.01e-11
Difference between the recovered and original coefficients (C20)				
	Max	Mean	Min	Sigma
Swarm A	6.87e-11	-8.94e-12	-1.04e-10	4.65e-11
Swarm B	7.83e-11	-6.66e-12	-9.26e-11	5.05e-11
Swarm C	5.91e-11	-5.58e-12	-5.81e-11	3.14e-11
Swarm A-B	1.06e-09	-6.63e-10	-1.04e-08	2.16e-09
Swarm A-C	9.93e-06	-9.65e-06	-1.52e-04	3.28e-05
Swarm A+(A-B)	6.84e-11	-8.99e-12	-1.02e-10	4.64e-11
Signal strength				
	Max	Mean	Min	RMS
C30 (LaD)	7.11e-11	-1.02e-11	-1.15e-10	6.61e-11
Difference between the recovered and original coefficients (C30)				
	Max	Mean	Min	Sigma
Swarm A	9.06e-11	-7.35e-12	-1.29e-10	4.48e-11
Swarm B	9.65e-11	-6.69e-12	-1.06e-10	4.76e-11
Swarm C	1.15e-10	-2.21e-11	-1.43e-10	6.54e-11
Swarm A-B	2.54e-09	-3.01e-10	-8.42e-09	1.88e-09
Swarm A-C	3.77e-04	3.03e-05	-9.06e-06	8.32e-05
Swarm A+(A-B)	9.10e-11	-7.28e-12	-1.29e-10	4.47e-11
Signal strength				
	Max	Mean	Min	RMS
C21 (LaD)	1.59e-11	1.47e-12	-2.13e-11	1.03e-11
Difference between the recovered and original coefficients (C21)				
	Max	Mean	Min	Sigma
Swarm A	1.32e-10	-4.52e-12	-9.93e-11	5.60e-11
Swarm B	1.22e-10	-6.37e-12	-9.56e-11	5.72e-11
Swarm C	1.04e-10	-5.81e-12	-1.40e-10	5.56e-11
Signal strength				
	Max	Mean	Min	RMS
C22 (LaD)	2.54e-11	9.80e-13	-2.99e-11	1.49e-11
Difference between the recovered and original coefficients (C22)				
	Max	Mean	Min	Sigma
Swarm A	1.20e-10	1.49e-12	-1.30e-10	5.71e-11
Swarm B	8.71e-11	-1.07e-11	-1.08e-10	5.18e-11
Swarm C	8.07e-11	-1.29e-11	-1.02e-10	5.50e-11
Signal strength				
	Max	Mean	Min	RMS
S21 (LaD)	2.36e-11	1.63e-12	-2.50e-11	1.24e-11
Difference between the recovered and original coefficients (S21)				
	Max	Mean	Min	Sigma
Swarm A	1.28e-10	1.75e-11	-1.72e-10	6.03e-11
Swarm B	1.16e-10	-8.95e-12	-9.80e-11	4.78e-11
Swarm C	8.42e-11	-3.10e-11	-1.67e-10	5.74e-11

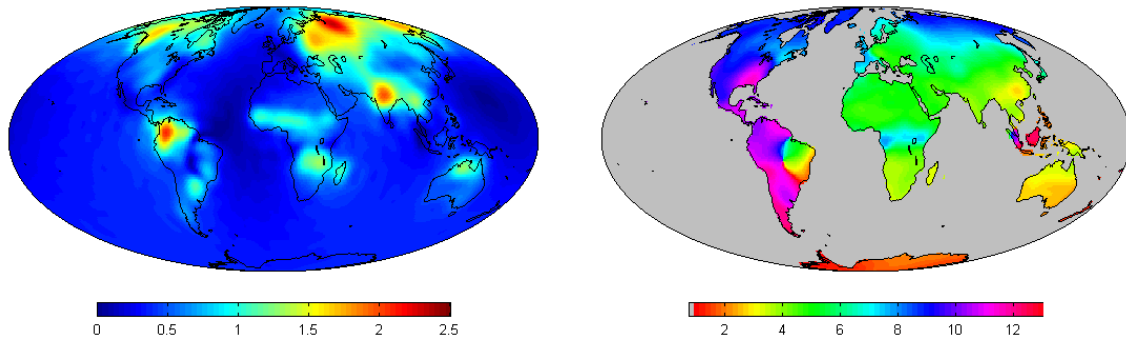
Signal strength				
	Max	Mean	Min	RMS
S22 (LaD)	3.10e-11	-6.34e-13	-3.63e-11	2.00e-11
Difference between the recovered and original coefficients (S22)				
	Max	Mean	Min	Sigma
Swarm A	9.98e-11	-4.79e-12	-9.06e-11	4.95e-11
Swarm B	1.26e-10	4.67e-12	-6.01e-11	5.06e-11
Swarm C	1.18e-10	-1.79e-12	-1.46e-10	6.44e-11

Besides the recovery of the single coefficients, an attempt is made to recover the annual (1 cpa) and semi-annual (2cpa) components of the hydrology signal. As mentioned, these are the largest amplitude components in the LaD model. First the recovery results from the K-band constellations up to d/o 30 are shown in section 4.5.2. Since the GPS-only solutions are not capable to recover the signal up to d/o 30 anyway, another experiment is made to recover the signal to degree and order 6 (section 4.5.3), which corresponds to a low-pass filter being applied after recovery of monthly mean fields.

4.5.2. Hydrology recovery with K-band constellations

Figure 4-20 shows the annual and semi-annual component of the hydrology signal together with its phase. Note that the phase is scaled in such a way that it corresponds to months. The number 1 corresponds to January and 12 to December. For example Figure 4-20 b) means the big bullet eye in Euro-Asia in Figure 4-20 a) happens in March to April every year. It is also to notice that the semi-annual signal is smaller than the annual signal and thus more difficult to recover than the latter. Note the different scales for annual and semi-annual components.





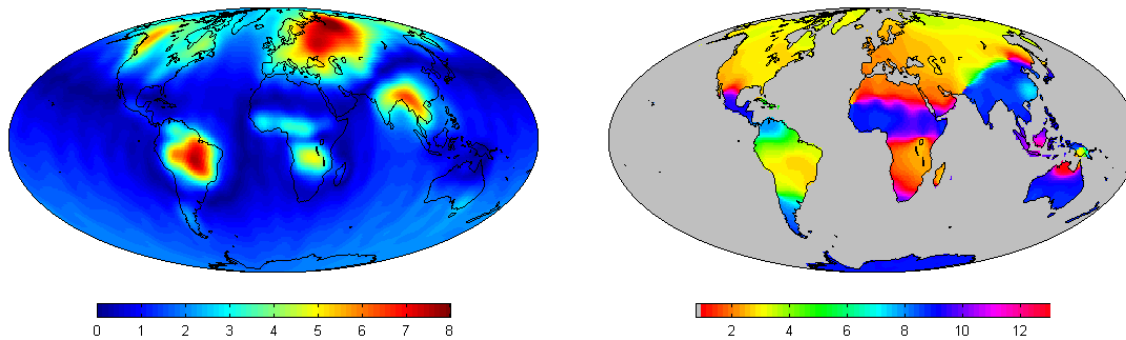
c)

d)

Figure 4-20 Annual and semi-annual component of LaD model, a) annual amplitude [mm], b) annual phase, c) semi-annual amplitude [mm], d) semi-annual phase

Results for the different K-band constellations are shown in Figure 4-21, where the recovered annual and semi-annual signals are plotted. For convenience all recovery scenarios are marked with different case numbers, where case 1 to 3 correspond to GRACE, pendulum and tandem/pendulum constellations, respectively. As mentioned the GPS-only constellations cannot recover the hydrology to degree and order 30 at all. Thus their solutions are not shown here.

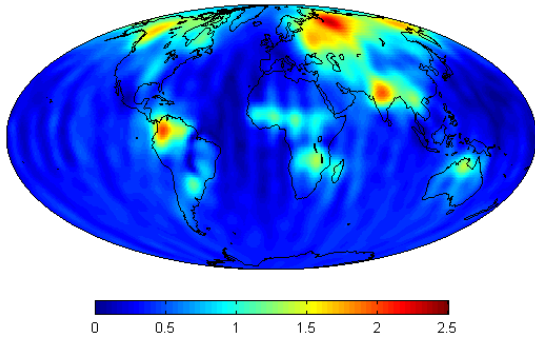
Case 1 Recovery by GRACE constellation



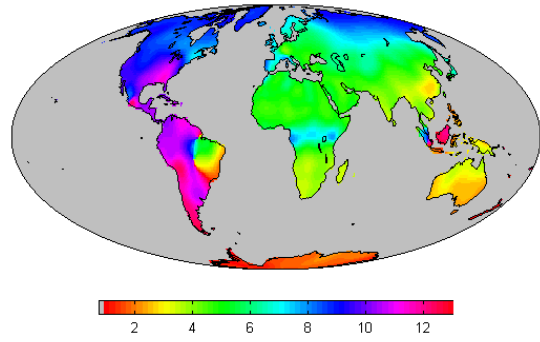
a)

b)

4.5 Time-variable hydrology signal recovery

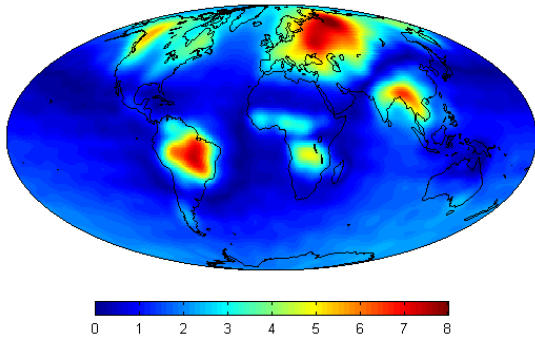


c)

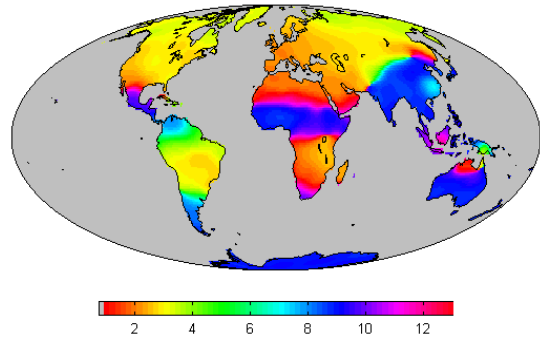


d)

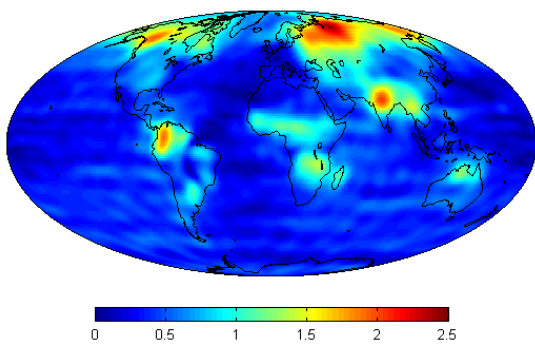
Case 2 Recovery by pendulum constellation



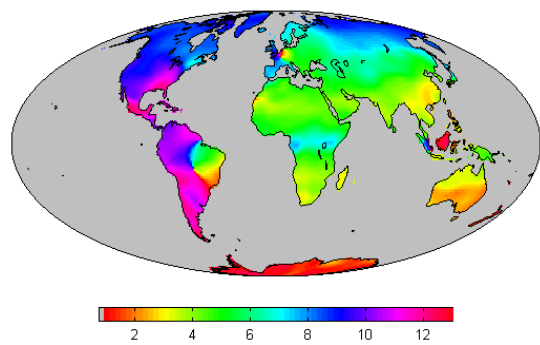
a)



b)



c)



d)

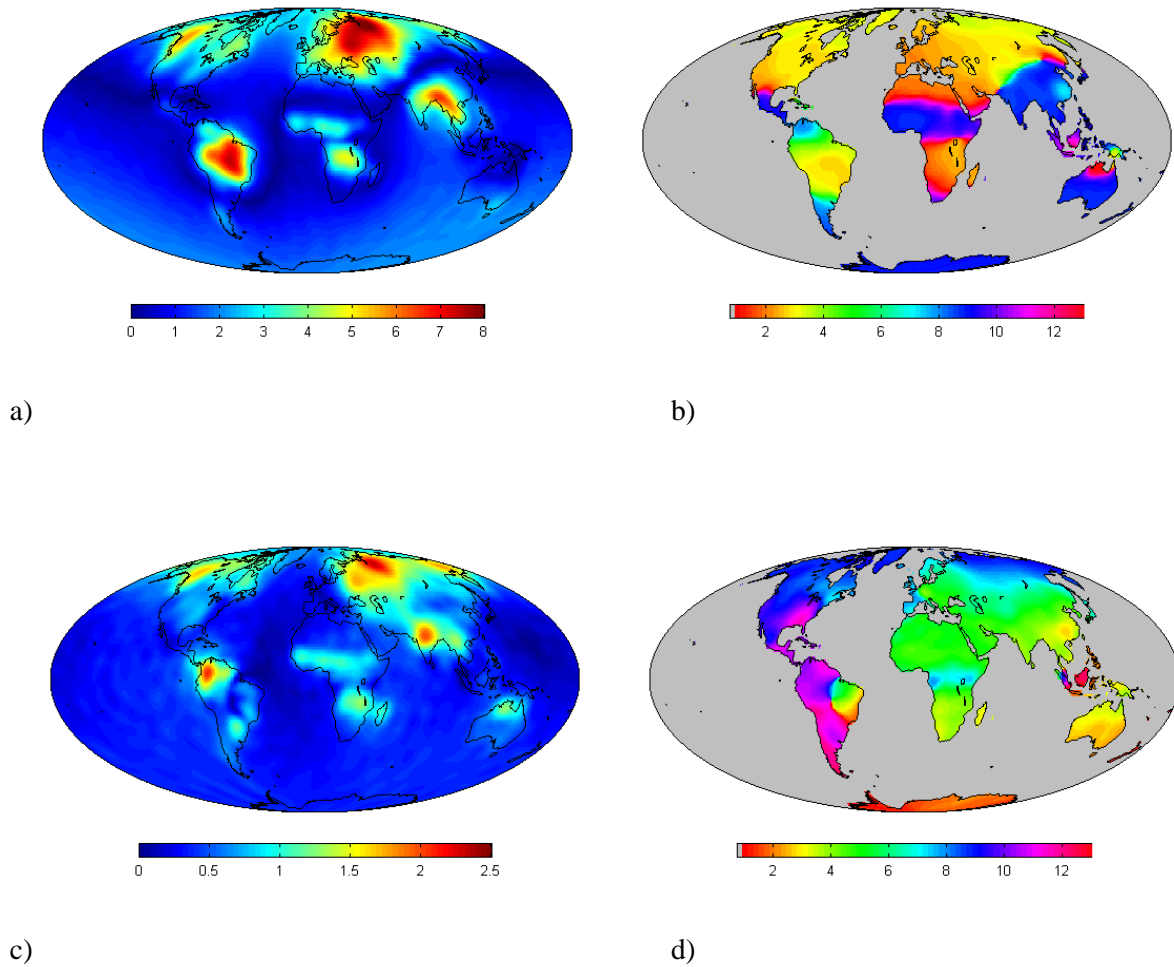
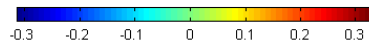
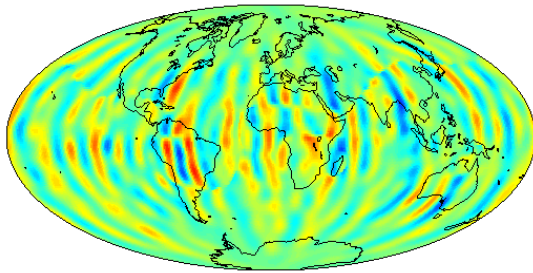
Case 3 Recovery by tandem/pendulum constellation

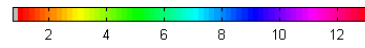
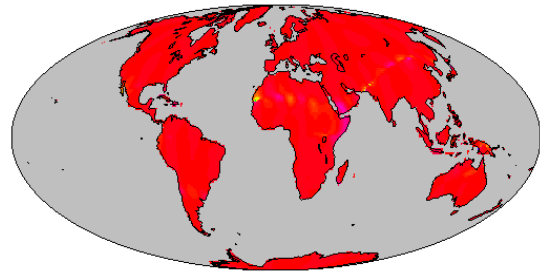
Figure 4-21 Hydrology recovery from different K-band constellations, a) annual amplitude [mm], b) annual phase, c) semi-annual amplitude [mm], d) semi-annual phase

As expected the recovery results by the K-band constellations show similar structure to the input signal. In Figure 4-22 the difference between the recovered fields and the original LaD model is shown. The corresponding statistics are listed in Table 4-9.

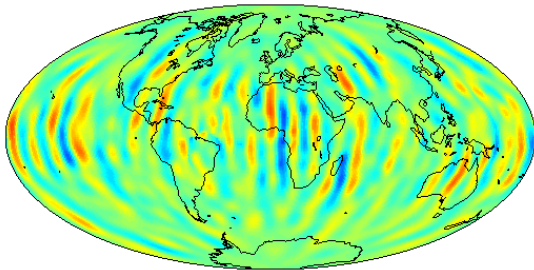
Difference of case 1, recovery by GRACE constellation



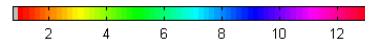
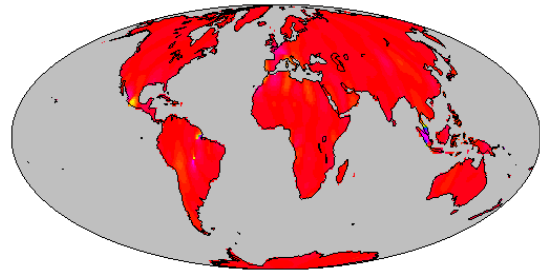
a)



b)

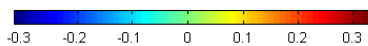
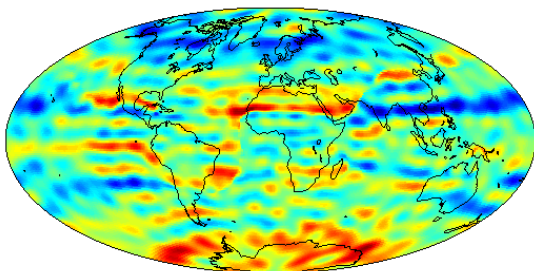


c)

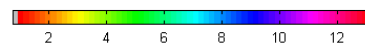
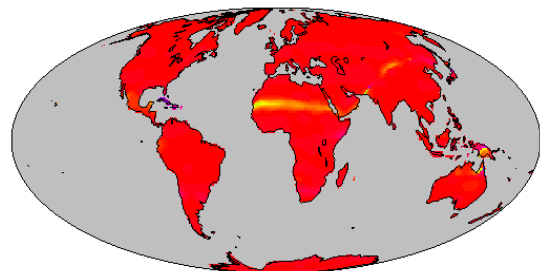


d)

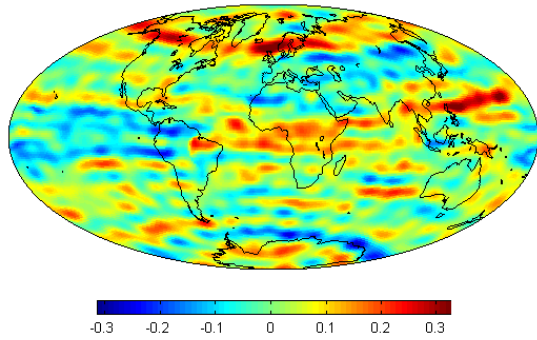
Difference of case 2, recovery by pendulum constellation



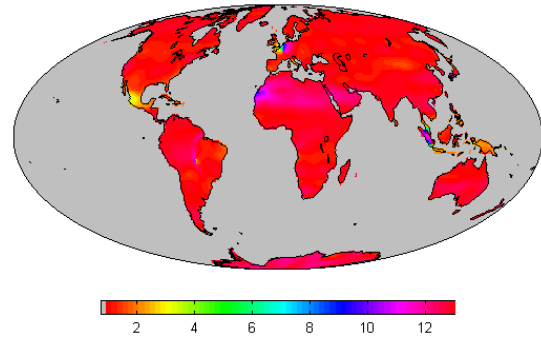
a)



b)

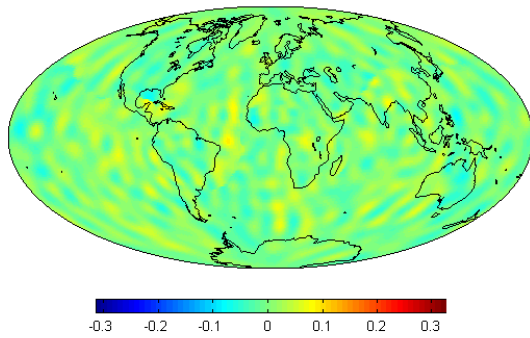


c)

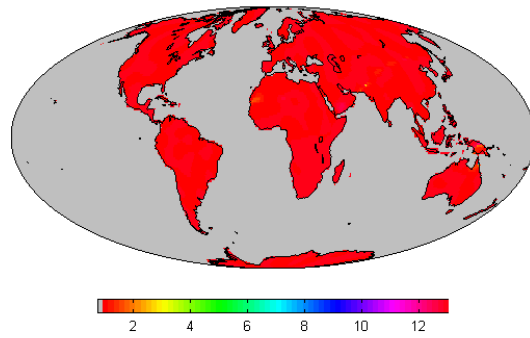


d)

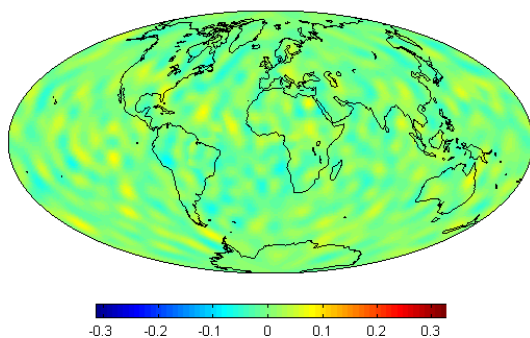
Difference of case 3, recovery by tandem/pendulum constellation



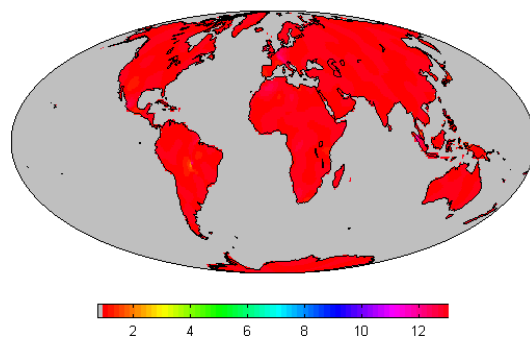
a)



b)



c)



d)

Figure 4-22 Difference between recovered hydrology signal and LaD model to d/o 30, a) annual amplitude [mm], b) annual phase, c) semi-annual amplitude [mm], d) semi-annual phase

Table 4-9 Geoid difference between recovered and original hydrology, K-band constellation, in [mm]

Constellation	Max	Mean	Min	Sigma
Difference in annual component				
GRACE (case 1)	0.23	2.6e-3	-0.21	0.05
pendulum (case 2)	0.32	2e-4	-0.31	0.10
tandem/pendulum (case 3)	0.09	6.5e-4	-0.08	0.021
Difference in semi-annual component				
GRACE (case 1)	0.20	2.9e-3	-0.20	0.05
pendulum (case 2)	0.39	0.03	-0.29	0.09
tandem/pendulum (case 3)	0.08	4.5e-4	-0.08	0.019
Signal strength				
	Max	Mean	Min	RMS
Annual signal	8.23	1.91	2.9e-3	1.35
Semi-annual	2.32	0.52	2.3e-3	0.34

Obviously the K-band constellations can recover the annual signal very well. As shown in Table 4-9, the error of the recovery is below 0.1 mm for both case 1 and 2. There are phase shifts observable, especially in Africa for case 2. The geoid plots reveal the characteristic stripe patterns oriented North-South for GRACE and East-West for the cross-track pendulum mission. In reality, apart from this typical anisotropic error characteristic of the GRACE constellation, also aliasing due to temporal and spatial undersampling of the time variations as well as errors in the de-aliasing products are likely to contribute to the stripe pattern (Reubelt *et al.* [2010]). Swenson and Wahr [2006] have analyzed the spatial correlations in GRACE errors and developed correlated-error filtering to mitigate the stripe patterns. As the corrections for AO and ocean tides are assumed to be perfect in this simulation, the stripe patterns shown here can be attributed solely to the observation geometry. Since the phase picture of the signal is mostly oriented in East-West direction, it can also be expected, that a GRACE-type tandem mission is better suited to resolve the phase than a pendulum mission, since the errors of the former are oriented perpendicular to the phase picture, while the error characteristics of the pendulum mission is similar to the phase picture. This is supported by Figure 4-22.

The stripe pattern can be expected to vanish for the tandem/pendulum combination, which leads to an isotropic error characteristic (see case 3) of Figure 4-22). Also the phase is resolved with no significant phase shifts. The statistical values in Table 4-9 show that the tandem/pendulum combination improves the global geoid error by a factor of 2 to 5. However, it should be noted that a pendulum constellation is challenging from an engineering point of view. Since the orbits of the two satellites cross at the poles, the two satellites will switch their relative position. Therefore the inter-satellite ranging instruments should be able to rotate the measuring direction in flight. Since this seems to be too demanding for currently available technology, the eMotion project proposes to keep the measuring direction fixed with respect to the spacecraft bodies in order to maintain the stability of the instrument system. Instead, it is proposed to rotate the whole satellite when following the relative position change (Pail, personal communication).

4.5.3. Hydrology recovery with GPS-only constellations

Since it is only possible to recover the full time variable signal up to degree and order 30 with the K-band scenarios, the maximum degree should be limited for the GPS-only solutions in order to find the potential for recovery of the low degree temporal variations. Like shown before, some zonal coefficients can be recovered from a GPS-only single satellite solution. Several studies have already tried to recover the lower spherical harmonic degrees from CHAMP. Moore *et al.* [2005] have combined CHAMP with SLR data from 5 satellites and investigated the variability at the annual and

semi-annual periodicities for degrees 2 to 6. They found that CHAMP has a positive effect in the combined solution on the recovery of the annual variation. They also concluded that only degree 2 to 4 terms of the temporal variations recovery from a CHAMP-only solution may contain useful information. Reigber *et al.* [2007] have also suggested the recovery of the temporal gravity field from CHAMP to be restricted to degree and order 4, corresponding to a half wavelength of 5000 km. A recent study by Prange [2010] shows that it is possible to determine temporal gravity changes up to degree and order 10 by stacking monthly solutions based on 8 years of CHAMP data. According to this study some prominent seasonal signal, e.g. in the Amazon river basin, may be detected with CHAMP up to degree and order 10. Flechtner *et al.* [2010] also confirmed that the coefficients determined up to degree and order 10 from 8 years of CHAMP data show a high correlation to the solutions from GRACE, which means that it is possible to recover the temporal variations up to this degree and order. Obviously higher degree variations (up to degree 10) can be resolved from longer time spans. Since 2 years of data are simulated here, the recovery simulation is carried out up to degree and order 6, which is also the highest degree in the attempt of Moore *et al.* [2005]. In fact, the coefficients up to degree 6 contain already a large part of the 1 cpa component (Zenner, [2006]).

In Figure 4-23 the annual and semi-annual components to degree and order 6 are plotted. Comparing Figure 4-20 and Figure 4-23 it is observable that the annual component to degree and order 6 (Figure 4-23 a)) shows an “attenuated” version of the signal to degree and order 30 from Figure 4-20 a). Despite of losing details the major structure of the annual component, e.g. the Bullet eye in Euro-Asia, is already prominent at a spectral resolution of degree 6. The semi-annual component, however, loses most of the structure which can be seen from Figure 4-20 c). The statistics are listed in Table 4-10.

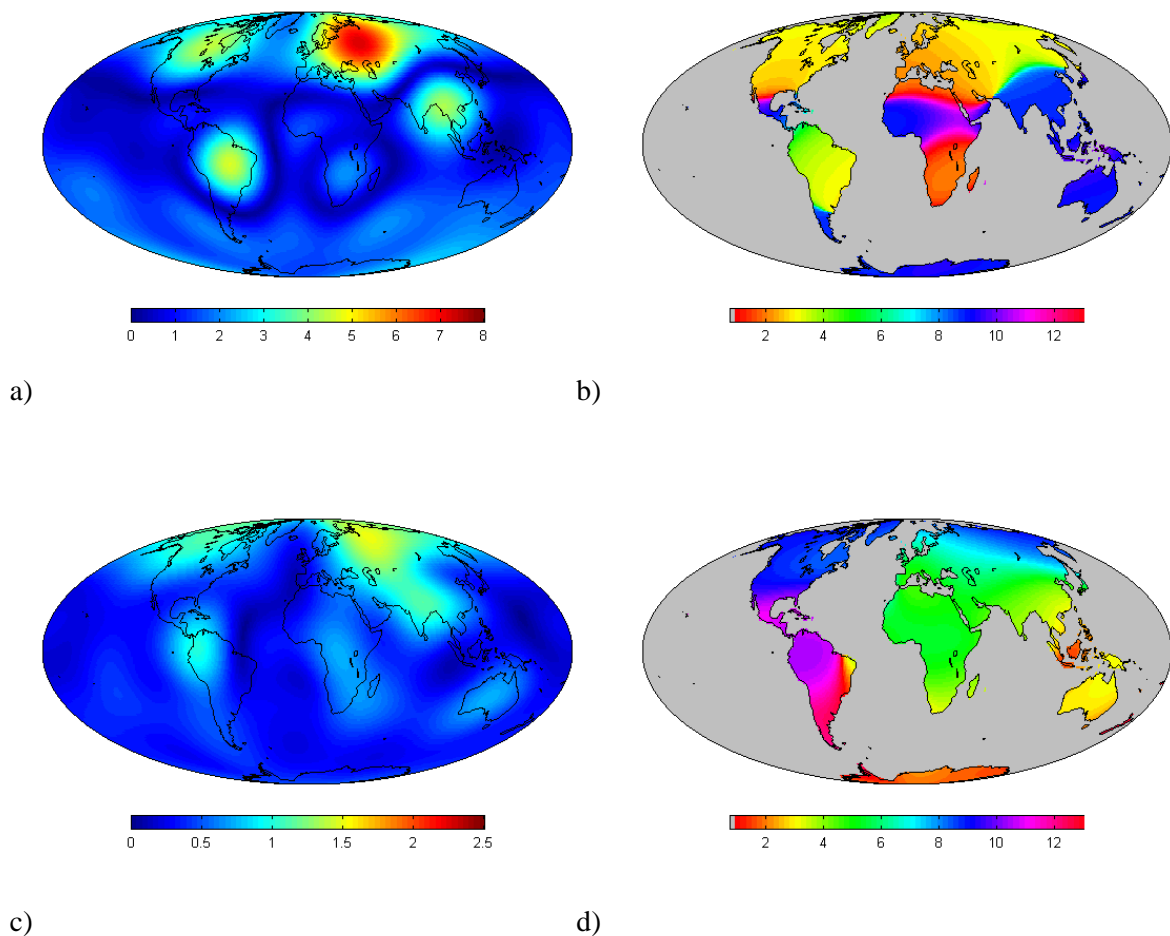
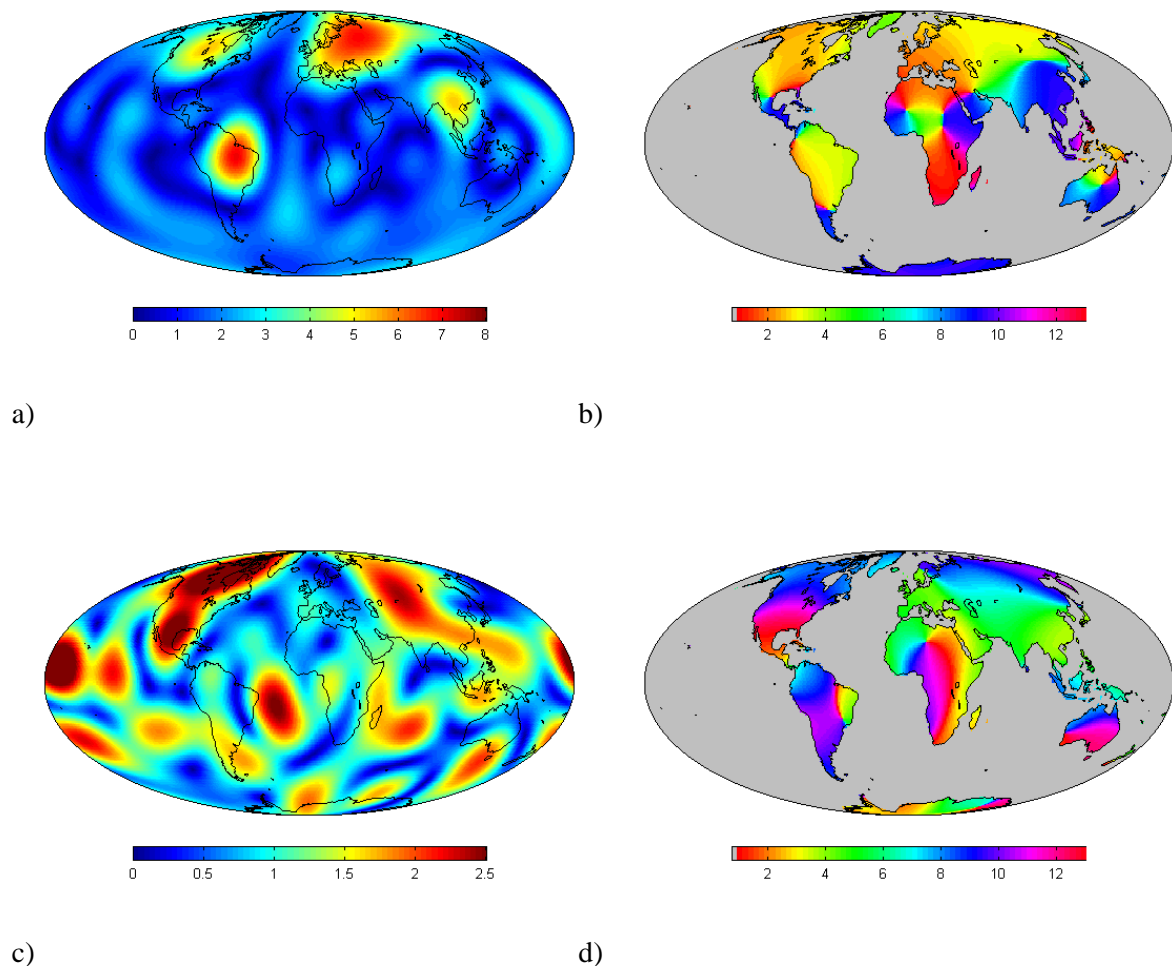


Figure 4-23 Annual and semi-annual component of LaD model to d/o 6, a) annual amplitude [mm], b) annual phase, c) semi-annual amplitude [mm], d) semi-annual phase

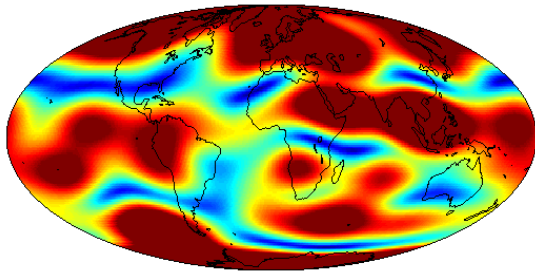
4.5 Time-variable hydrology signal recovery

The results of the recovery from different constellations are plotted in Figure 4-24. Swarm A and the combined solution A+(A-B) can recover the annual component and its phase, although showing errors in both amplitude and phase. The difference between the recovered fields and the original LaD field for these two scenarios is plotted in Figure 4-25 and the statistics of the comparisons are listed in Table 4-10. None of the pure baseline solutions is capable to recover the time variations between degrees 2 to 6. None of the constellations can recover the semi-annual component. The results indicate that single satellite solutions are more promising for recovery of the low degrees than baseline solutions. This again supports the expectation, that baselines are more suitable to increase the resolution in the high degrees, but provide less useful information in the low degrees. Focusing on the single satellite solutions it should be noticed, that Swarm can offer 3 independent single solutions, which in combination should significantly improve the spatial-temporal sampling of the gravity field.

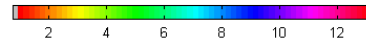
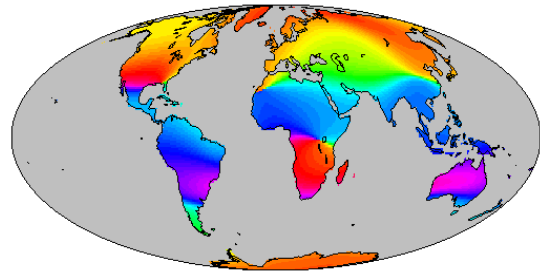
Case 4 Recovery by Swarm A



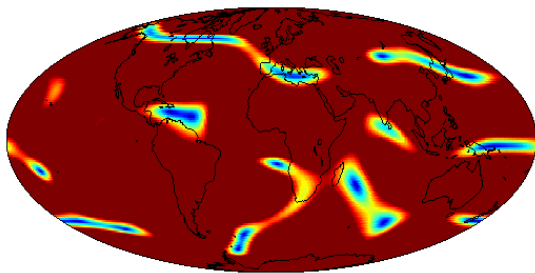
Case 5 Recovery by Swarm A-B



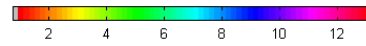
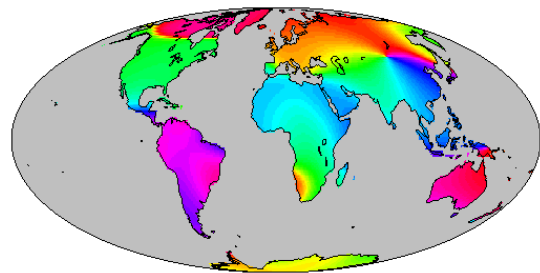
a)



b)

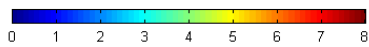
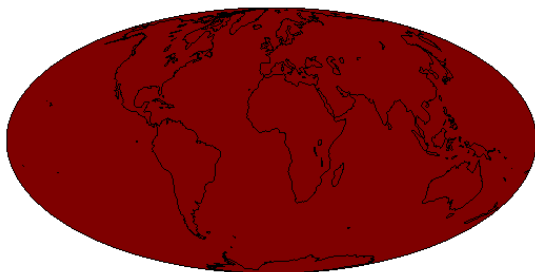


c)

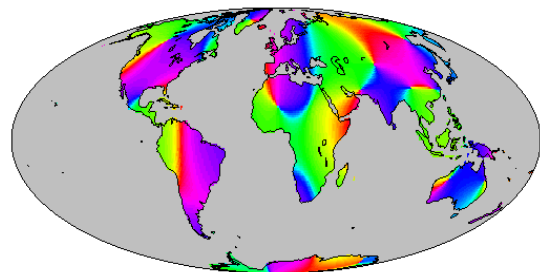


d)

Case 6 Recovery by Swarm A-C

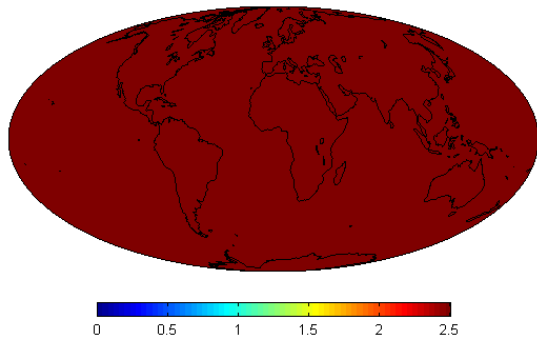


a)

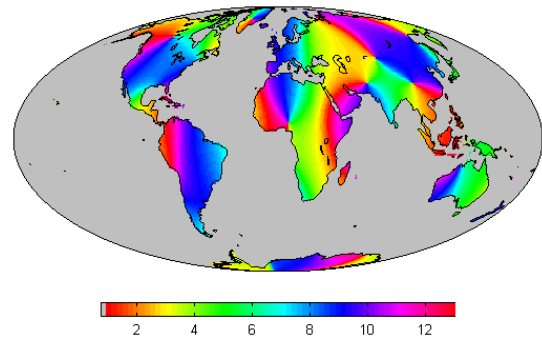


b)

4.5 Time-variable hydrology signal recovery

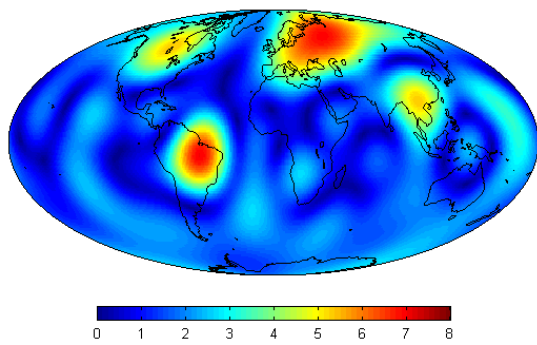


c)

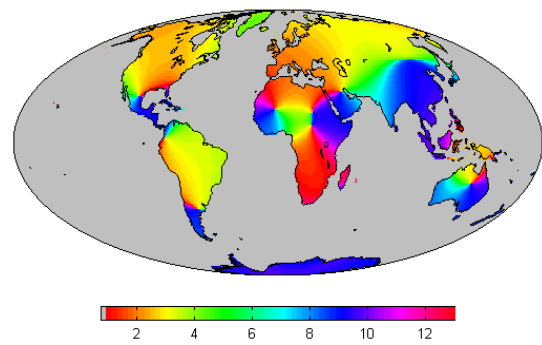


d)

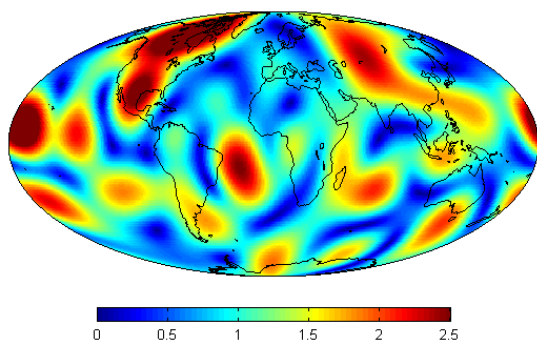
Case 7 Recovery by Swarm A+(A-B)



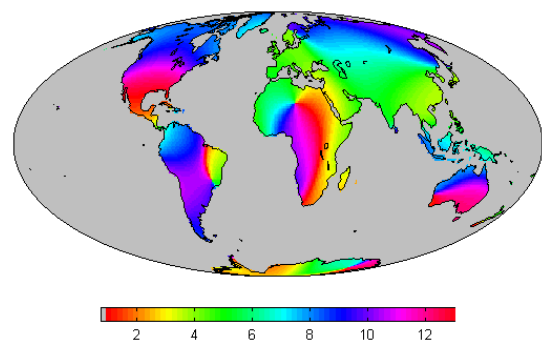
a)



b)



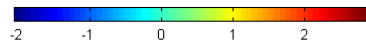
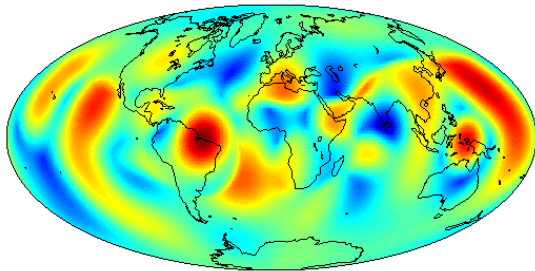
c)



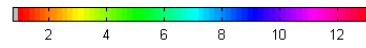
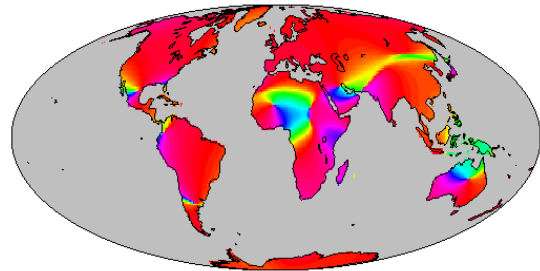
d)

Figure 4-24 Hydrology recovery from different GPS-only constellations to d/o 6, a) annual amplitude [mm], b) annual phase, c) semi-annual amplitude [mm], d) semi-annual phase

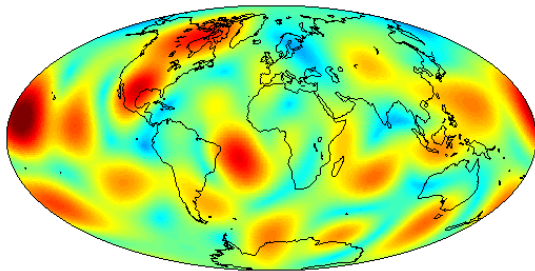
Difference of case 4, recovered by Swarm A



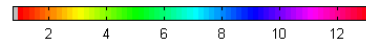
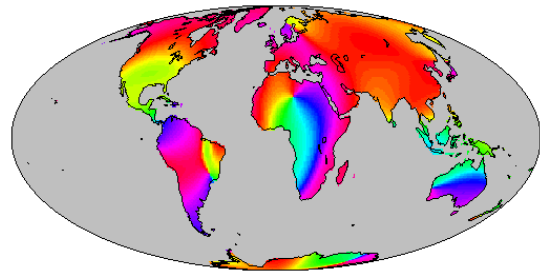
a)



b)

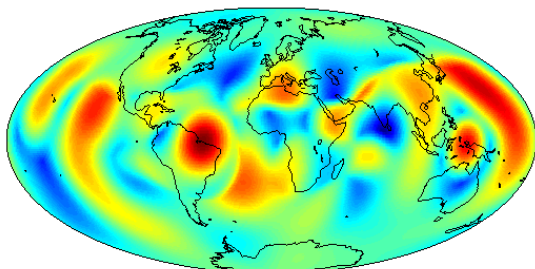


c)

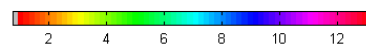
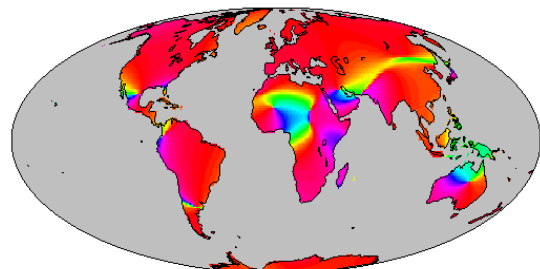


d)

Difference of case 7, recovered by Swarm A+(A-B)

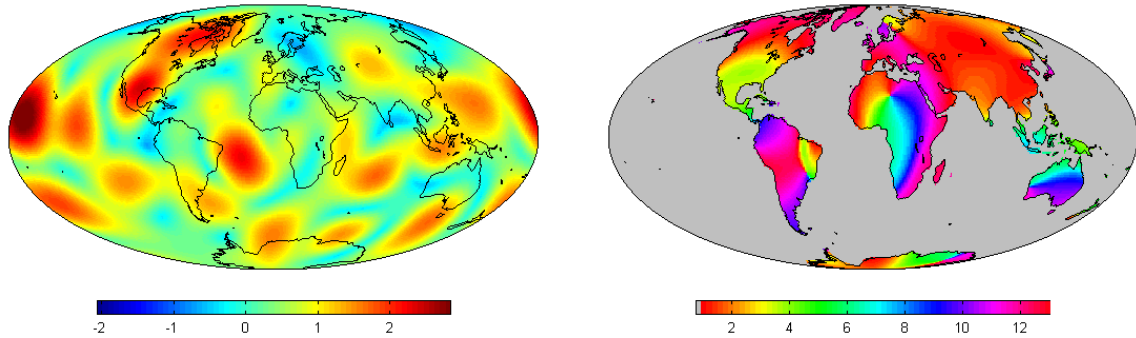


a)



b)

4.5 Time-variable hydrology signal recovery



c)

d)

Figure 4-25 Difference between recovered hydrology signal and LaD model to d/o 6, a) annual amplitude [mm], b) annual phase, c) semi-annual amplitude [mm], d) semi-annual phase

Table 4-10 Geoid difference between recovered and original hydrology, GPS-only constellation, in [mm]

Constellation	Max	Mean	Min	Sigma
Difference in annual component				
Swarm A (case 4)	2.87	0.30	-2.07	0.62
A + (A-B) (case 7)	2.83	0.29	-2.07	0.61
Difference in Semi-annual component				
Swarm A (case 4)	3.06	0.64	-0.73	0.58
A + (A-B) (case 7)	3.03	0.63	-0.74	0.57
Signal strength to degree and order 6				
	Max	Mean	Min	RMS
Annual	7.23	1.92	0.01	1.25
Semi-annual	1.49	0.54	0.004	0.32

Additional discussion about the A-C baseline with future GNSS system

As mentioned in section 4.2, the threshold (max. 5000 km baseline) for selecting the observability of A-C baseline is implemented in order to ensure 5-6 GPS satellites in common view. This criterion holds for the current situation, where GPS is the only available global GNSS system. With the realization of the European GNSS system Galileo and the Chinese system Compass as well as the reactivation of the Russian GLONASS system, there will be likely more than 80 GNSS satellites in the near future, much more than the current 32 GPS satellites. Galileo and Compass are designed to be consistent with GPS and it is thus possible to do navigation tasks with satellites mixed from these systems. In that case it should be less difficult to have enough common GNSS satellites in view even for large baselines. Thus the main criterion to choose observations to form the A-C baseline should be the accuracy, which is to a large extent determined by the relative velocity, as shown in section 2.2. Figure 4-26 shows the observability of A-C baseline according to different baseline velocity thresholds. The threshold of 5000 m/s is approximately equally effective as the old criterion. A larger threshold allows more observations to form the A-C baseline. The upper limit can be set in a way that the accuracy of the baseline A-C is not worse than the simple difference between these two satellites, as derived in section 2.2. This limit results in a relative velocity threshold of 10800 m/s, which allows about 45% observations to form the A-C baseline.

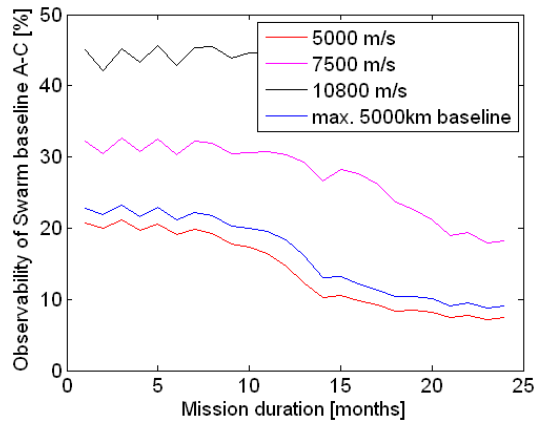


Figure 4-26 Observability of Swarm A-C baseline for different thresholds

Alternatively, one can make use of all the observations and implement an appropriate weighting scheme according to the individual accuracy, as discussed in section 4.1. By doing so, A-C baseline can also contribute to recovery of the annual component of the hydrology signal to degree and order 6. Like shown in Figure 4-27, the recovered annual component reveals the prominent structure in Euro-Asia. The semi-annual signal, however, is still not recovered. The difference between the recovered and the original LaD signal is plotted in Figure 4-28 and statistical values are listed in Table 4-11.

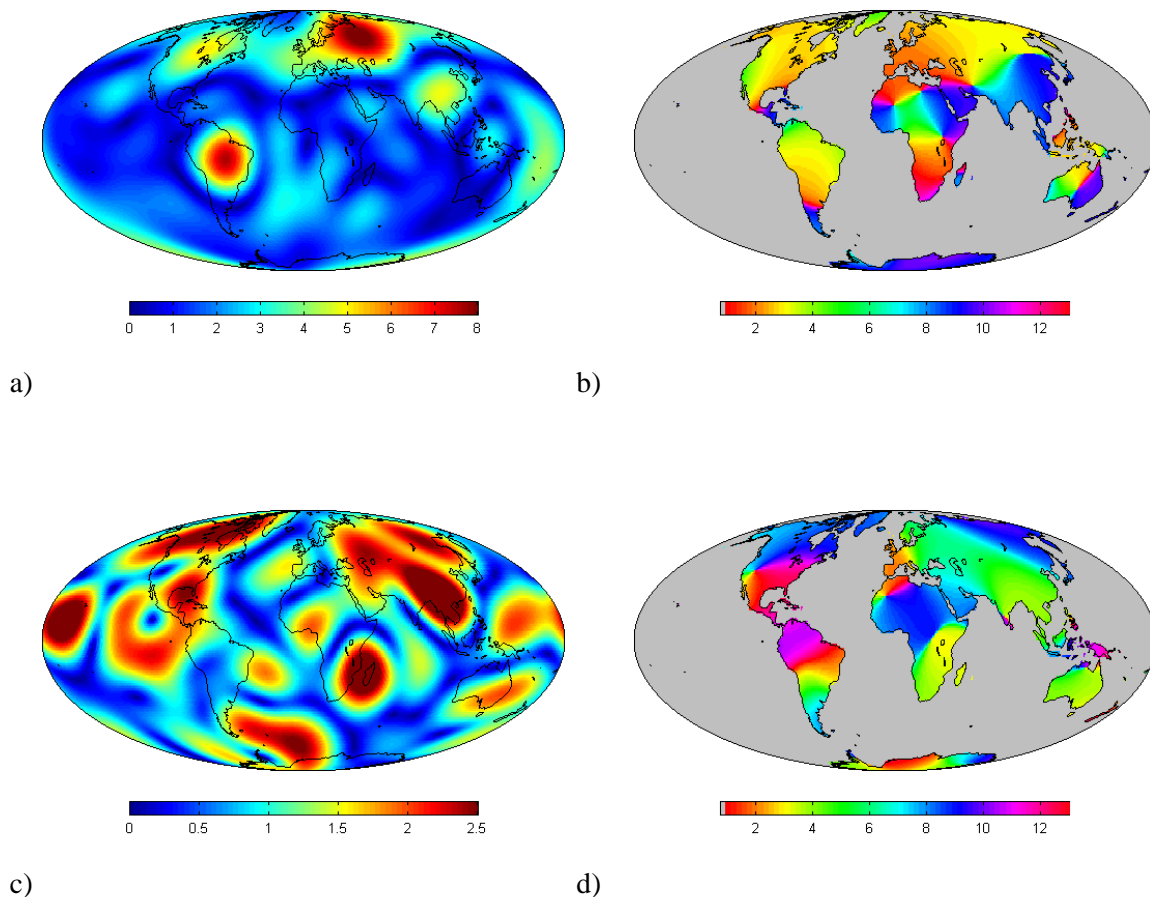


Figure 4-27 Hydrology recovery from A-C baseline with new criterion, a) annual component, b) annual phase, c) semi-annual component, d) semi-annual phase

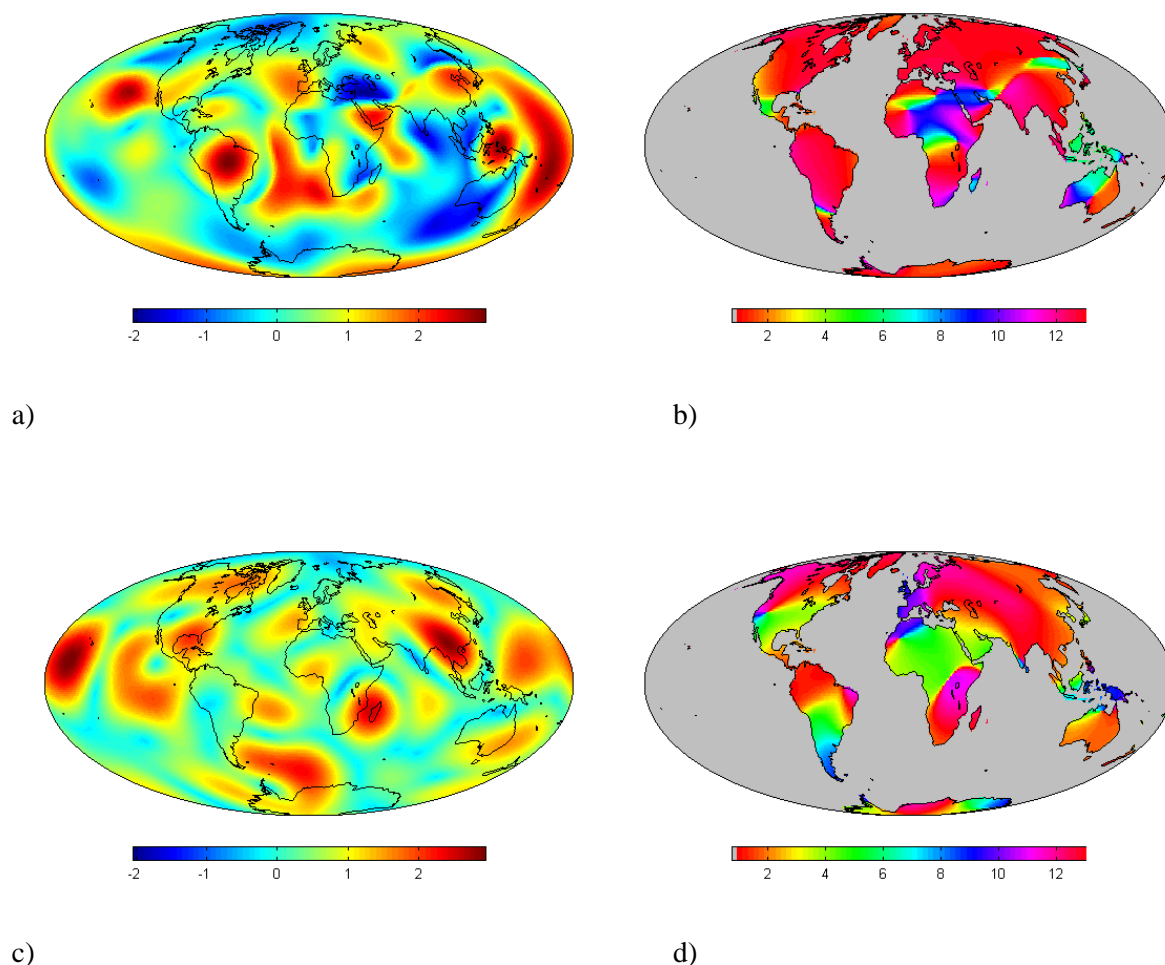


Figure 4-28 Difference between recovered hydrology signal (A-C baseline with new criterion) and LaD model to d/o 6, a) annual amplitude [mm], b) annual phase, c) semi-annual amplitude [mm], d) semi-annual phase

Table 4-11 Geoid difference between recovered and original hydrology, Swarm A-C (new criterion), in [mm]

Constellation	Max	Mean	Min	Sigma
Difference in annual component				
Swarm A-C (new criterion)	2.95	0.39	-2.05	0.87
Difference in semi-annual component				
Swarm A-C (new criterion)	2.97	0.67	-0.81	0.66
Signal strength to degree and order 6				
	Max	Mean	Min	RMS
Annual	7.23	1.92	0.01	1.25
Semi-annual	1.49	0.54	0.004	0.32

The recovery results here show significant improvement in comparison with the A-C baseline with the old threshold, where it was not possible at all to see any signal structure (Figure 4-24 case 6). By comparing Table 4-11 with Table 4-10, Figure 4-28 with Figure 4-25, it is obvious that despite more observations the recovery quality of the A-C baseline is still worse than that of the single satellite solution Swarm A or the combined solution A+(A-B). The results thus still suggest using single satellite solutions to recover the low degree terms of the time-variable gravity signal.

In comparison to K-band constellations, the accuracy of GPS positioning and baseline measurements are not at the same level. Thus the quality of the gravity field recovery by Swarm (GPS-only) is not comparable to that from GRACE in both static and time-variable field recovery. Still, considering that GRACE may terminate in the near future, Swarm may continue the observation of the time-variable gravity field and thus fill the gap to the launch of GRACE follow-on mission, though with much lower accuracy and resolution.

5. Conclusion and discussion

5.1. Summary and conclusion

Information based on time-variable gravity solutions benefits a wide spectrum of Earth sciences, such as continental hydrology, glaciology, and solid Earth as well as oceanography studies. As GRACE has already passed the designed life time, it may terminate due to technical reasons (most likely due to drain-out of the battery) before its gap-filler or follow-on mission is in place. Therefore, it is interesting to see if there can be a mission which can continue providing solutions of time-variable gravity field in case GRACE indeed fails. This dissertation investigates the ESA magnetic field mission Swarm, which consists of three CHAMP-like satellites and will be started in 2012. Although it is not a dedicated gravity mission, the instrument combination GPS receiver/accelerometer makes it appropriate for the gravity purpose as well. Besides absolute GPS positioning for single satellites, the constellation allows also the derivation of GPS baseline measurements between the satellites. GPS baselines are expected to be determined with an accuracy of one magnitude higher than the absolute GPS measurements. It is thus interesting to see if this improvement can benefit the recovery of the time-variable gravity signals (e.g. continental hydrology). Besides, Swarm combines baselines in all different directions, i.e. mixed along-track and radial (Swarm A-C) and cross-track (Swarm A-B). It is well known that different baseline constellations lead to different error structures. For example, for an along-track baseline like GRACE, the sectorial and near-sectorial coefficients are less well determined. Therefore an analysis of such baselines and especially the combination of those are very useful for mission planning.

The energy balance method is implemented here for the purpose of the gravity field recovery simulations. This method is based on the energy conservation law, which states that the sum of kinetic and potential energy should be a constant in a conservative field. Studies on CHAMP, GRACE and GOCE have demonstrated its utilization in praxis in recent years. One special aspect of this method is that the non-conservative forces must be treated appropriately in the energy equation. These forces include e.g. atmospheric drag, solar radiation, albedo and most relevant to this dissertation, the time-variable gravity signals.

In general all non-conservative accelerations must be integrated along the orbit, where the accelerations can be either modeled or measured from the onboard accelerometer. Once the non-conservativeness is neglected, an error will be introduced. The direct tide, ocean tide, atmosphere-ocean and hydrology signals were investigated with regard to this issue. In order to show the size of the effect of non-conservativeness of the time variations, the difference between (i) integration of accelerations along the orbit and (ii) potential series computed directly from a given set of time-variable potential coefficients through spherical harmonics synthesis are shown. While (i) holds for arbitrary fields, (ii) assumes the field to be a conservative one. It was found that in principle all time variations show the non-conservativeness effect (denoted as ϵ_{con}). The size of ϵ_{con} varies for different signals. The largest effect was found for direct tides, while the smallest effect for the continental hydrology. For a single satellite, the non-conservativeness effect shows up as a drift, while for two-satellite constellations the drift is significantly reduced. By comparing the size of ϵ_{con} with the error budget for GPS and GRACE-type K-band measurements, it was found that for both single satellite and satellite constellation, the non-conservativeness for tidal signal are so large that they cannot be neglected. For a K-band measurement, the ϵ_{con} for atmosphere-ocean signal should also be considered. For GPS-only measurements, however, it can be neglected. It was also found that for the hydrology signal, the ϵ_{con} is so small that it can be neglected for both GPS-only and K-band measurements. Thus the hydrology signal can be regarded as conservative, i.e. static within a month. The simulation in section 4.5 for recovery of the continental hydrology signal can therefore employ the specialized

energy balance equation, assuming that all other time variations are well-known from models or accurate enough measured from onboard instruments so they can be fully removed from the observation equation.

A simplified error analysis is provided in order to give an estimate of the achievable accuracy in the simulation studies. Some realistic values are introduced for the error standard deviations of absolute and relative velocities for single satellite and constellations, respectively. It is found that the relative velocity of the baseline gives the largest contribution for error propagation. Based on the relative velocity values for along-track and cross-track, whereby the constellation can be regarded as stable, it was demonstrated that the GPS baseline can indeed lead to an accuracy of about one order of magnitude better than the absolute GPS measurement. This holds, however, not for the oblique baseline, where the relative velocity varies significantly with time as the geometry of such baseline changes with time. In a worst case scenario the error of an oblique baseline is about 20 times larger than that for the stable along- or cross-track baseline and it is even worse than the simple difference between the two satellites. Thus it is suggested that a threshold should be introduced to exclude the observation epochs where the relative velocity is so large that it will degrade the recovery results. It was also demonstrated that a GRACE-type K-band measurement system can bring an accuracy which is about 100 times better than along-track GPS-only baseline, or 1000 times better than absolute GPS measurement for a single satellite.

The spectral analysis of the hydrology signal shows that the dominant frequencies in the LaD model are the 1 cpa and 2 cpa components, which represent annual and semi-annual variations, respectively. It is found that the highest frequency of this model is 6 cpa, which corresponds to a 2-monthly component. It is also found that a large part of the signal is concentrated at the coefficients with degree and orders less than 30. Above degree 70 there is almost no signal observable. This finding holds also for the atmosphere-ocean signal, represented by the ECMWF-OMCT combination, where the strongest signal components are concentrated at the coefficients below degree 10. Besides the low frequency part, AO signal contains very high frequencies as well, such as diurnal or semi-diurnal components. These fast-changing components are beyond the current temporal resolution of the satellite gravimetry missions and will thus alias into the recovery results. Their impacts need to be corrected by applying the de-aliasing process, which is discussed in section 4.4. It is shown that hydrology aliasing effects prevent detection of the hydrology signal above about degree 40 from a single satellite, while at degree 30 the aliasing error is only about 1% of the signal strength. For atmosphere-ocean and ocean tide signals, studies and discussions have shown that for the currently achieved accuracy level of GRACE-type K-band and the GPS-only measurements, the de-aliasing error do not play an important role and thus do not affect the recovered field significantly. For further missions with advanced instruments (e.g. laser ranging), however, such de-aliasing errors can be of importance and should be taken care of to avoid degradation of the recovered field.

In Chapter 4 simulation studies were carried out. The simulation algorithms were introduced and the simulator was validated for its correctness. It was found that despite of some small errors for certain coefficients, the simulator can be regarded as closed-loop. Starting from the Swarm constellations, a GRACE-type constellation, a pendulum constellation and a tandem/pendulum constellation were simulated as well. Besides the absolute and relative GPS measurements for the Swarm constellation, K-band SST link was simulated for the GRACE, pendulum and tandem/pendulum constellations. In section 4.3 the static field recovery was carried out to recover the EGM96 field up to degree and order 70. It was demonstrated in the error-free simulation that the reduction process can effectively remove the effect of the time-variable gravity signals on the static field recovery, despite the sampling of 30 seconds and the simple integration algorithm. Denser sampling or a more accurate integration algorithm can further improve the effectiveness of the reduction process. It was then found in the full-error simulation that Swarm should be able to recover the static field up to degree and order 70. The GPS baseline can increase the spectral resolution slightly, while the accuracy for the lower degree coefficients will be somewhat decreased as compared to a single satellite constellation. It was shown that the sectorial and near-sectorial coefficients are less well determined by an along-track constellation, while the zonal coefficients are less well determined by a cross-track constellation. A

5.1 Summary and conclusion

radial constellation or a combination of along- and cross-track, such as the tandem/pendulum constellation, provides an isotropic error spectrum.

In section 4.5 a 24-month simulation was carried out, attempting to recover the continental hydrology signal. The LaD model was added to the static field EGM96 at the beginning of every month and all other time variations were assumed to be perfectly removed. White noise was applied to the simulated observations. The simulation results confirmed that K-band constellations are capable to recover the time variable field up to degree and order 20 to 30. The best solution is derived from the tandem/pendulum constellation, which shows an isotropic error structure and suffers less from the stripe patterns as compared to the results of the GRACE and pendulum constellations. In contrast, under the current situation, none of the GPS-only baselines are capable to resolve the temporal variations to degree and order 30. Only single satellite solutions can recover the annual signal up to degree and order 6. Over all the GPS-accuracy is too low to detect the smaller semi-annual signal. Given the fact that more GNSS satellites will be available in the near future, the GPS-only Swarm A-C baseline may also detect the annual signal up to degree 6, although still not as good as the single satellite solution. Considering, that Swarm can provide three independent single satellite solutions, the mission can be used for detection of the low degrees of time-variable gravity signal with a spatial-temporal sampling better than CHAMP (due to the availability of 3 satellites). Recent studies reported that it is possible to determine the seasonal variations of the gravity field up to degree and order 10 based on 8 years of CHAMP data. The same can be expected, when multi years of Swarm orbit data become available. In fact, with the availability of 3 satellites, even better results can be expected from Swarm.

Swarm is scheduled for launch in 2012. Considering that GRACE may terminate some time between 2013 to 2015, Swarm may continue the time-series of gravity measurements and bridge the gap between GRACE and the GRACE follow-on mission, though with much lower accuracy and capability. Given the fact that CHAMP has already terminated and GOCE has a design life of only 2 years, Swarm could indeed be the only LEO mission contributing to temporal variations of the low degree spherical harmonics in the near future. Moreover, even a combination of Swarm and GRACE (if it still operates after the launch of Swarm) may help to reduce temporal/spatial aliasing in the low degree harmonics by providing a better sampling in space and time. Therefore, Swarm can be regarded as a welcome complementary mission to the dedicated gravity missions and will provide valuable information on both static and time-variable gravity fields in the near future.

5.2. Discussion

As the simulation results suggest, Swarm may help to bridge a possible interruption of the time-variable gravity field observation after an eventual failure of GRACE in the near future. But clearly, due to the insufficient accuracy of the GPS-only measurements, the quality of the temporal gravity recovery from Swarm will degrade significantly as compared to GRACE. A future mission is needed for continuing and improving the observation of the time-variable gravity field. Although it is not the objective of this dissertation to develop a concept for a future mission, some statements are given here:

- **Advanced sensor techniques** When designing a future mission for the determination of the time-variable gravity field, it may be possible to take advantage of the new developments of the measuring instruments to obtain higher accuracy. One possibility is to replace the microwave ranging instrument implemented on GRACE with a laser ranging system. The latter will allow the distance between satellites to be measured with about 100 times better accuracy (Bender *et al.* [2003], Aguirre-Martinez and Sneeuw [2002], Sneeuw *et al.* [2005]). Another possibility would be to use a drag-compensation system. Such system uses a shielded proof mass as a reference point for inter-satellite measurements. Rather than measuring the non-gravitational accelerations, a thruster system is used to compensate for the non-gravitational forces acting on the satellite and to keep it centered about the proof mass. The proof mass acceleration noise is lower than that of accelerometer, because the noise associated with the acceleration measurement is avoided. Additionally, such system enables the satellite to fly at a lower altitude, thus resulting in a better sensitivity to the mass transport and distribution in the Earth system and an improved spatial resolution. Loomis [2009] claims that the drag-compensation system outperforms the laser ranging system, but even with both systems implemented, the improvement of regional gravity estimates may still only be moderate, due to the limitations of temporal aliasing.
- **Formation flight missions** An appropriate constellation, by incorporating radial or cross-track information into the observation rather than using the GRACE-type pure along-track measurement, can improve the determination of temporal variations. Besides the tandem/pendulum constellation shown in this dissertation, the Cartwheel and the LISA formation flights are alternative options for such constellations (Sharifi *et al.* [2007]). The Cartwheel and LISA formation flights can be established by setting slightly different inclinations, ascending node or the eccentricity for different satellites. Sneeuw *et al.* [2008 a, b] have investigated the stability for GRACE, pendulum, Cartwheel and LISA formations in a realistic gravity field. It was found that while the long-term stability of LISA type formations needs further investigation, the other formations can be regarded as stable, though formation-keeping maneuvers would be needed (Wiese, personal communication). Similar to the simulation results for tandem/pendulum constellation, the Cartwheel formation was also found to be able to significantly reduce the North-South stripe patterns seen in GRACE solutions and it was reported to bring a considerable improvement over the current GRACE mission (Sneeuw *et al.* [2008 a], Wiese *et al.* [2008]).
- **Improvement of de-aliasing** As mentioned in section 4.4, given the currently achieved accuracy level of GRACE and GPS-only measurements, de-aliasing errors do not play an important role in the recovery of the time-variable gravity field. For a future mission with advanced measurement systems, however, the de-aliasing error is of significant importance. De-aliasing can be improved by advancements in modeling of the fast-changing temporal gravity signals, such as atmosphere-ocean and tides. Additionally, satellite constellations with increased time/space sampling may help to detect these temporal changes and thus reduce the aliasing errors. The time-shift and longitude-shift techniques described by Reubelt *et al.* [2010] can be optional methods to increase both time and space sampling. Theoretically, though, the

5.2 Discussion

full determination of these fast-changing variations may require large number of satellites (sensors) and thus may not be feasible. Still, improvement of sampling can be achieved also by combining different constellations. For example, as mentioned, a combination of Swarm and GRACE may help reduce the temporal aliasing in low degree harmonics.

List of abbreviations

AOD	Atmosphere and Ocean De-aliasing product
CHAMP	CHAllenging Minisatellite Payload
CNES	Centre National D'Etudes Spatiales
COSMIC	Constellation Observing System for Meteorology, Ionosphere, and Climate
CSR	Center for Space Research university of Texas at Austin
DFT	Discrete Fourier Transform
ECMWF	European Centre for Medium-Range Weather Forecasts
EGM96	Earth Gravitational Model 1996
ESA	European Space Agency
FES99	global tide Finite Element Solution 1999
FES2002	global tide Finite Element Solution 2002
FFT	Fast Fourier Transform
GFDL	Geophysical Fluid Dynamics Lab
GFZ	GeoForschungsZentrum
GLDAS	Global Land Data Assimilation System
GOCE	Gravity Field and Steady-State Ocean Circulation Explorer
GNSS	Global Navigation Satellite System
GPS	Global Positioning System
GRACE	Gravity Recovery And Climate Experiment
HOPE	Hamburg Ocean Primitive Equation
IB	Inverted Barometer
IDFT	Inverse Discrete Fourier Transform
JPL	Jet Propulsion Laboratory
KBR	K/Ka-Band Ranging
LaD	Land Dynamics Model
LAGEOS	LAser GEOdynamics Satellite
LEO	Low Earth Orbit satellite
NASA	National Aeronautics and Space Administration
NOAA	National Oceanic and Atmospheric Administration
NCEP	National Centers for Environmental Prediction
NOAA	National Oceanic & Atmospheric Administration
OMCT	Ocean Model for Climate and Tides
PGR	Post Glacial Rebound
RMS	Root Mean Square
SLR	Satellite Laser Ranging
SST	Satellite-to-Satellite Tracking
SGG	Satellite Gravity Gradiometry
Swarm	Name of ESA's magnetic field mission
VI	Vertical Integration approach

List of figures

Figure 1-1 Trend derived from 8-years GRACE data, expressed in water column [cm/year]	2
Figure 2-1 Geometry of the baseline between Swarm A/B and Swarm C	12
Figure 2-2 Illustration of temporal aliasing error (based on Loomis [2009]).....	16
Figure 3-1 The hydrology cycle (http://ga.water.usgs.gov/edu/watercyclehi.html).....	22
Figure 3-2 Hydrology geoid for 01.2003 in [mm], max = 6.6, min = -4.06, mean = 0.02, RMS = 1.02	24
Figure 3-3 Degree RMS for LaD model over 24 months, up to degree 180 (a) and degree 30 (b).....	24
Figure 3-4 Mean AO geoid for 01.2003 in [mm], max = 11.3, mean = 1.46, min = -7.22, RMS = 3.19	28
Figure 3-5 Degree RMS of AO for the year 2003, up to degree 180 (a) and degree 30 (b).....	28
Figure 3-6 M2 ocean tides, amplitude in centimeter (top panel) and the corresponding phase (bottom panel), Schrama [2005]	30
Figure 3-7 Time series of tidal potential along a satellite orbit from (gray) integration of tidal accelerations and (black) synthesis from tidal potential harmonic coefficients. The upper panel shows a zoom-in version of the first half day of the 30 days shown in the lower panel.	33
Figure 3-8 Effect of non-conservativeness for a single satellite ($[m^2/s^2]$), a) direct tides, b) ocean tides, c) hydrology and d) atmosphere-ocean	34
Figure 3-9 Effect of non-conservativeness for 2-satellite constellation ($[m^2/s^2]$), a) direct tides, b) ocean tides, c) hydrology, d) atmosphere-ocean	35
Figure 4-1 Simulation flowchart (based on Peters [2007])	37
Figure 4-2 a) ground track plot of 10 days, b) disturbing potential along the orbit from energy balance, c) the difference between b) and the disturbing potential directly computed from synthesis	43
Figure 4-3 Difference between recovered and original EGM96 field in geoid (panel a)) and in spherical harmonics coefficients (panel b)).....	43
Figure 4-4 The Swarm constellation (Olsen <i>et al.</i> [2007]).....	44
Figure 4-5 Scalar distance between Swarm A and B (a), scalar distance between Swarm A and C (b), the changing geometry of baseline A-C (c).....	45
Figure 4-6 Simulated constellations, inter-satellite links marked in red.	47
Figure 4-7 Geoid difference between recovered field and EGM96 without reduction, a) Swarm A, b) Swarm A-B, c) Swarm A-C, d) GRACE, all in [m].....	49
Figure 4-8 Geoid difference between recovered field and EGM96 with correction, a) Swarm A, b) Swarm A-B, c) Swarm A-C, d) GRACE, all in [mm].....	50

List of figures

Figure 4-9 Geoid difference between recovered field and EGM96, with reduction, with noise, a) Swarm A, b) Swarm A-B, c) Swarm A-C, d) Swarm A+(A-B), e) GRACE, f) pendulum, g) tandem/pendulum, in [m]	52
Figure 4-10 Comparison of the potential coefficients, a) Swarm A, b) Swarm A-B, c) Swarm A-C, d) Swarm A+(A-B), e) GRACE, f) pendulum, g) tandem/pendulum.....	54
Figure 4-11 Degree RMS plot for static gravity field recovery	55
Figure 4-12 Aliasing effect from hydrology in [mm], a) Swarm A, b) Swarm A-B, c) Swarm A-C, d) GRACE, e) H mean.....	57
Figure 4-13 Degree RMS of Swarm A.....	58
Figure 4-14 Observability of Swarm A-C baseline during 2 years	60
Figure 4-15 Degree RMS for May (top panel) and October (bottom panel).....	61
Figure 4-16 C20 (left) and C30 (right) determined from Swarm A, B and C	62
Figure 4-17 C20 determined from baseline solutions	63
Figure 4-18 C30 determined from baseline solutions	64
Figure 4-19 Determination of C21, C22, S21, S22 from single satellites	64
Figure 4-20 Annual and semi-annual component of LaD model, a) annual amplitude [mm], b) annual phase, c) semi-annual amplitude [mm], d) semi-annual phase.....	67
Figure 4-21 Hydrology recovery from different K-band constellations, a) annual amplitude [mm], b) annual phase, c) semi-annual amplitude [mm], d) semi-annual phase.....	69
Figure 4-22 Difference between recovered hydrology signal and LaD model to d/o 30, a) annual amplitude [mm], b) annual phase, c) semi-annual amplitude [mm], d) semi-annual phase.....	71
Figure 4-23 Annual and semi-annual component of LaD model to d/o 6, a) annual amplitude [mm], b) annual phase, c) semi-annual amplitude [mm], d) semi-annual phase.....	73
Figure 4-24 Hydrology recovery from different GPS-only constellations to d/o 6, a) annual amplitude [mm], b) annual phase, c) semi-annual amplitude [mm], d) semi-annual phase.....	76
Figure 4-25 Difference between recovered hydrology signal and LaD model to d/o 6, a) annual amplitude [mm], b) annual phase, c) semi-annual amplitude [mm], d) semi-annual phase.....	78
Figure 4-26 Observability of Swarm A-C baseline for different thresholds	79
Figure 4-27 Hydrology recovery from A-C baseline with new criterion, a) annual component, b) annual phase, c) semi-annual component, d) semi-annual phase	79
Figure 4-28 Difference between recovered hydrology signal (A-C baseline with new criterion) and LaD model to d/o 6, a) annual amplitude [mm], b) annual phase, c) semi-annual amplitude [mm], d) semi-annual phase	80

List of tables

Table 2-1 Velocity and velocity errors used for the simplified error analysis	12
Table 3-1 Global water balance (Gruber <i>et al.</i> [2009])	23
Table 3-2 Difference between integrated accelerations and directly computed potential [m ² /s ²]	35
Table 4-1 Adding time variation to static filed	39
Table 4-2 Simulation conditions	48
Table 4-3 Geoid difference between recovered and original EGM96 field without reduction in [m] ..	49
Table 4-4 Geoid difference between recovered and original EGM96 field with reduction, in [mm] ...	50
Table 4-5 Noise level for the simulation in [mm] and [mm/s]	51
Table 4-6 Difference between recovered field and EGM96 in [m]	51
Table 4-7 Aliasing effect from hydrology in [mm], d/o 70	57
Table 4-8 Single coefficients recovery from Swarm constellation	65
Table 4-9 Geoid difference between recovered and original hydrology, K-band constellation, in [mm]	72
Table 4-10 Geoid difference between recovered and original hydrology, GPS-only constellation, in [mm]	78
Table 4-11 Geoid difference between recovered and original hydrology, Swarm A-C (new criterion), in [mm]	80

Bibliography

Aguirre-Martinez M., Sneeuw N. (2002) Needs and tools for future gravity measuring missions. *Space Sci Rev* 108: 409–416

Badura T., Sakulin C., Gruber C., Klostius R. (2005) Derivation of the CHAMP-only global gravity field model TUG-CHAMP04 applying the energy integral approach. *Studia Geophysica et Geodaetica* Volume 50, Number 1, 59-74, DOI: 10.1007/s11200-006-0002-3

Bender P., Hall J., Ye J., Klipstein W. (2003) Satellite–satellite laser links for future gravity missions. *Space Sci. Rev.* 108:377–384

Briggs W. L. (1995) *The DFT: An owner's manual for the Discrete Fourier Transform*. Society for industrial and applied mathematics, Philadelphia

Cartwright D.E. (1993) *Theory of ocean tides with application to altimetry*. Lecture notes in Earth Science, R. Rummel and F. Sansò (eds.), Volume 50, Springer Verlag.

Cartwright D.E. (1999) *Tides, a scientific history*. Cambridge University Press

Chao B.F., Gross R.S. (1987) Changes in the Earth's rotation and low-degree gravitational field induced by earthquakes. *Geophys. J. R. Astron. Soc.*, 91, 569-596

Chao B.F. (1994) The geoid and Earth rotation, in *geoid and its geophysical interpretations*. P. Vanicek and N. Christou (eds.), pp. 285-298, CRC Press, Boca Raton, Fla.

Desai S. (1996) *Ocean tides From TOPEX/POSEIDON altimetry with some geophysical applications*. Dissertation, University of Colorado at Boulder

Ditmar P., Bezdek A., Liu X., Zhao Q. (2009) On a feasibility of modeling temporal gravity field variations from orbits of non-dedicated satellites. *International Association of Geodesy Symposia*, 2008, Volume 133, Part 2, 307-313, DOI: 10.1007/978-3-540-85426-5_36

Ditmar P., Klees R. (2002) *A method to compute the Earth's gravity field from SGG/SST data to be acquired by the GOCE satellite*. DUP science, Delft University Press, ISBN 90-407-2284-6

Drijfhout S., Heinze C., Latif M., Maier-Reimer E. (1996) Mean circulation and internal variability in an ocean primitive equation model. *J. Phys. Oceanogr.*, 26, 559-580

Drinkwater M., Haagmans R., Muzi D., Popescu R., Floberghagen R., Kern M., Fehringer M. (2007) *The GOCE gravity mission: ESA's first core Earth explorer*. Proceedings of the 3rd international GOCE user workshop, 6-8 November, 2006, Frascati, Italy, ESA special publication, SP-627 (2007) 1-8

Dunn C., Bertiger W., Bar-Sever Y., Desai S., Haines B., Kuang D., Franklin G., Harris I., Kruizinga G., Meehan T., Nandi S., Nguyen D., Rogstad T., Thomas J., Tien J., Romans L., Watkins M., Wu S., Bettadpur S., Kim J. (2003) Instrument of GRACE: GPS augments gravity measurements. *GPS World* 14(2): 16-28

Eanes R., Bettadpur S. (1995) *The CSR 3.0 global ocean tide model*. Tech. Memo. CSR-TM-95-06, Cent. for Space Res., Univ. of Tex., Austin

Bibliography

- ESA SP-1279-6 (2004) The Earth's magnetic field and environment explorers. Technical and Programmatic Annex to ESA SP-1279-6, ESA Publication Division, ESTEC, Noordwijk
- Farrell W.E. (1972) Deformation of the Earth by surface loading. *Rev. Geophys.*, 10, 761-797
- Flechtner F. (2007) AOD1b product description document for product releases 01 to 04 GRACE 327-750 (GR-GFZ-AOD-0001), Rev 3.1. GeoForschungszentrum Potsdam, Department 1: Geodesy and Remote Sensing
- Flechtner F. (2010) Beobachtung von Massenverteilung und Massenvariationen im System Erde mit den Satelliten CHAMP, GRACE und GOCE. *Geodätische Woche 2010*, Köln
- Friis-Christensen E., Lühr H., Hulot G. (2002) Swarm—a constellation to study the dynamics of the Earth's magnetic field and its interaction with the Earth system. Proposal for ESA Earth Explorer Opportunity Missions, January 2002, ISSN 1602-527X, DSRI Report 1/2002
- Friis-Christensen E., Lühr H., Hulot G. (2006) Swarm: A constellation to study the Earth's magnetic field. *Earth, Planets and Space*, 58, 4, 351-358.
- Gerlach C. (2003) A note on the use of energy integrals for gravity field recovery. Unpublished note, Technische Universität München.
- Gerlach C., Földvary L., Svehla D., Gruber T., Wermuth M., Sneeuw N., Frommknecht B., Oberndorfer H., Peters T., Rothacher M., Rummel R., Steigenberger P. (2003) A CHAMP-only gravity field model from kinematic orbits using the energy integral. *Geophys. Res. Lett.*, 30(20), 2037, doi:10.1029/2003GL018025.
- Gerlach, C., Visser P. (2006) Swarm and gravity, possibilities and expectations for gravity field recovery. Proceeding of first Swarm international workshop, ESA WPP-261
- Gray R. M., J. W. Goodman (1995) *Fourier Transforms*. Kluwer Academic Publishers, Boston
- Gruber T. (2009) The global water cycle from a geodetic point of view. SPP1257 Meeting, Eitorf, Germany
- Haagmans R. (2004) Swarm - the Earth's magnetic field and Environment Explorer. ESA SP-1279(6), 2004.
- Han S.-C., Jekeli C., Shum C.K. (2004) Time-variable aliasing effects of ocean tides, atmosphere, and continental water mass on monthly mean GRACE gravity field. *J Geophys. Res.*, 109, B04403, doi:10.1029/2003JB002501
- Han S.-C. (2004) Efficient determination of global gravity field from satellite-to-satellite tracking. *Celest. Mech. Dyn. Astron.* 88, pp. 69-102.
- Han S.-C., Jekeli C., Shum C.K. (2002) Efficient gravity field recovery using in situ disturbing potential observables from CHAMP. *Geophys. Res. Lett.*, 29(16), 1789, doi: 10.1029/2002GL015180.
- Hotine M., Morrison F. (1969) First integrals of the equations of satellite motion. *Bull. Geod.*, 91, 41-45, 1969.
- Jekeli C. (1981) Alternative methods to smooth the Earth's gravity field. Rep. 327, Dep. Of Geod. Sci. and Surv., Ohio State Univ., Columbus

Bibliography

Johannessen J., Balmino G., Provost L., Rummel R., Sabadini R., Sünkel H., Tscherning C., Visser P., Woodworth P., Hughes C., Legrand P., Sneeuw N., Perosanz F., Aguirre-Martinez M., Rebhan H., Drinkwater M. (2003) The European Gravity Field and Steady-State Ocean Circulation Explorer satellite mission: its impact on geophysics. *Surveys in Geophysics* 24 (2003) 339-386.

Kaula W.M. (1966) *Theory of Satellite Geodesy*. Blaisdell Pub Comp, Waltham, Massachusetts

Knudsen P., Andersen O. (2002) Correcting GRACE gravity fields for ocean tide effects. *Geophys. Res. Lett.*, 29(8), 1178, doi: 10.1029/2001GL014005.

Kotsiaros S. (2009) Development of algorithms and tools for data analysis, data visualization, and data validation for the Swarm satellite mission. ESA working paper 2355, pp. 20-27

Kurtenbach E., Mayer-Gürr T., Eicker A. (2009) Deriving daily snapshots of the Earth's gravity field from GRACE L1B data using Kalman filtering. *Geophys. Res. Lett.*, 36, L17102, doi:10.1029/2009GL039564.

Le Provost C., Lyard F., Lefevre F., Roblou L. (2002) FES 2002—a new version of the FES tidal solution series. Abstract Volume Jason-1 Science Working Team Meeting, Biarritz, France.

Lefevre F., Lyard F.H., Le Provost C., Schrama E.J.O. (2002) FES99: a global tide finite element solution assimilating tide gauge and altimetric information. *J. Atmos. Oceanic Technol.* 19, 1345–1356.

Loomis B. (2009) Simulation study of a follow-on gravity mission to GRACE. Dissertation, University of Colorado at Boulder, DAI-B 71/01, p. , Jul 2010, publication number 3387503

Matsumoto K., Takanezawa T., Ooe M. (2000) Ocean tide models developed by assimilating TOPEX/POSEIDON altimeter data into hydrodynamical model: a global model and a regional model around Japan. *Journal of Oceanography*, 56, 567-581

Meyer M. (2005) *Signalverarbeitung*, 4. Auflage, Vieweg Verlag

Milly P., Shmakin A. (2002) Global modeling of land water and energy balances. Part I: the Land Dynamics (LaD) model. *J Hydrometeo* 3:283-299

Moore P., King M.A. (2008) Antarctic ice mass balance estimates from GRACE: tidal aliasing effects. *J. Geophys. Res.*, 113, F02005, doi:10.1029/2007JF000871.

Moore P., Zhang Q., Althman A. (2005) Annual and semiannual variations of the Earth's gravitational field from satellite laser ranging and CHAMP. *J. Geophys. Res.*, VOL. 110, B06401, 14 PP., 2005doi:10.1029/2004JB003448

Neubert T., Manda M., Hulot G., R. von Frese, F. Primdahl, J. L. Jørgensen, E. Friis-Christensen, P. Stauning, N. Olsen, and T. Risbo (2001) Ørsted satellite captures high-precision geomagnetic field data. *EOS Transactions, AGU*, 82(7), 81–88

Olsen N., Lühr H., Sabaka T., Manda M., Rother M., Tøffner-Clausen L., Choi S. (2006) CHAOS—a model of the Earth's magnetic field derived from CHAMP, Ørsted, and SAC-C magnetic satellite data. *Geophys. J. Int.* Volume 166, Issue 1, pages 67–75, July 2006, DOI: 10.1111/j.1365-246X.2006.02959.x

Olsen N., Sabaka T., Gaya-Pique L. (2007) Study of an improved comprehensive magnetic field inversion analysis for Swarm (Final report), pp. 14-23

Bibliography

- Pail R., Goiginger H., Mayrhofer R., Schuh W., Brockmann J., Krasbutter I., Höck E., Fecher T. (2010) GOCE gravity field model derived from orbit and gradiometry data applying the time-wise method. ESA Living Planet Symposium 2010, Bergen, Norway
- Peters T. (2007) Modellierung zeitlicher Schwerevariationen und ihre Erfassung mit Methoden der Satellitengravimetrie. dissertation, Technische Universität München, Germany
- Peltier W. (2004) Global glacial isostasy and the surface of the ice-age Earth: the ICE-5G(VM2) model and GRACE. *Ann. Rev. Earth Planet. Sci.*, 32, 111-149
- Prange L. (2010) Global gravity field determination using the GPS measurements made onboard the low Earth orbiting satellite CHAMP. Dissertation, Universität Bern, Switzerland
- Ray R.D., Luthcke S.B. (2006) Tide model errors and GRACE gravimetry: towards a more realistic assessment. *Geophys. J. Int.*, 167, 1055–1059, doi:10.1111/j.1365-46X.2006.03229.x
- Reigber C. (2000) The CHAMP satellite.
http://op.gfz-potsdam.de/champ/systems/index_SYSTEMS.html
- Reigber C., Jochmann H., Wunsch J., Neumayer K., Schwintzer P. (2003) First insight into temporal gravity variability from CHAMP. *Earth Observation with CHAMP Results from Three Years in Orbit*. Springer Verlag, pp. 128-131
- Reigber C., H. Lühr and P. Schwintzer (2002) CHAMP mission status. *Adv. Space Res.*, 30, 129–134
- Reigber C., Jochmann H., Wunsch J., Petrovic S., Schwintzer P., Barthelmes F., Neumayer K., König R., Förste C., Balmino G., Biancale R., Lemoine J., Loyer S., Perosanz F. (2007) Earth gravity field and seasonal variability from CHAMP. *Earth Observation with CHAMP Results from Three Years in Orbit*. Springer Verlag, pp. 25-30
- Reubelt T., Sneeuw N., Sharifi M.A. (2010) Future mission design options for spatio-temporal geopotential recovery. *Gravity, Geoid and Earth Observation, International Association of Geodesy Symposia, 2010, Volume 135, Part 2, 163-170, DOI: 10.1007/978-3-642-10634-7_22*
- Rodell M., Houser PR, Jambor U., Gottschalck J., Mitchell K., Meng CJ, Arsenault K., Cosgrove B., Radakovich J., Bosilovich M., Entin JK, Walker JP, Lohmann D., Toll D. (2004) The global land data assimilation system. *Bull Am Meteor Soc*, 85(3):381-394, doi:10.1175/BAMS-85-3-381
- Rummel R., Balmino G., Johannessen J., Visser P., Woodworth P. (2002) Dedicated gravity field missions-principles and aims. *Journal of Geodynamics Volume 33, Issues 1-2, January-March 2002, Pages 3-20, doi:10.1016/S0264-3707(01)00050-3*
- Sabaka T. J. and N. Olsen (2006) Enhancing comprehensive inversions using the Swarm constellation. *Earth Planets Space*, 58, 371–395, 2006
- Savcenko R. (2010) personal communication
- Savcenko R. and W. Bosch (2008) EOT08a – empirical ocean tide model from multi-mission satellite altimetry. Internal. Report, No. 81, Deutsches Geodätisches Forschungsinstitut, München
- Schrama E. (2005) Tides. Delft University of Technology, Faculty of Aerospace Engineering, lecture notes, Delft

Bibliography

- Schmidt R. (1999) Numerische Integration gestörter Satellitenbahnen mit Matlab. IAPG/FESG Schriftreihe, 5, Diplomarbeit, TU München
- Schneider M.(1967) Beiträge zur Bahnmechanik künstlicher Erdsatelliten, Teil II, Deutsche Geodätische Kommission, Reihe C, No. 113
- Seo K.W., Wilson C.R., Han S.C., Waliser D.E. (2008a) Gravity Recovery and Climate Experiment (GRACE) alias error from ocean tides. *J. geophys. Res.*, 113/B03405, doi:10.1029/2006JB004747, March 2008.
- Seo K.W., Wilson C.R., Chen J., Waliser D.E. (2008b) GRACE's spatial aliasing error. *Geophys. J. Int.* 172, 41–48, doi: 10.1111/j.1365-246X.2007.03611.x
- Sharifi M., Sneeuw N., Keller W. (2007) Gravity recovery capability of four generic satellite formations. In: Kilicoglu A, Forsberg R (eds.) Gravity field of the Earth. General Command of Mapping, ISSN 1300-5790, Special Issue 18, pp 211–216
- Sneeuw N. (1994) A semi-analytical approach to gravity field analysis from satellite observations. Dissertation, ISSN 0065-5325, ISBN 3769695666
- Sneeuw N. (2003a) Modelling a time-variable potential in the energy balance equation. Unpublished note, University of Calgary.
- Sneeuw N. (2003b) Space-wise, time-wise, torus and Rosborough representation in gravity field modeling. *Space Science Reviews* 108, 37-46
- Sneeuw N., Gerlach C., Svehla D., Gruber C. (2003 c) A first attempt at time variable gravity recovery from CHAMP using the energy balance approach. In: Tziavos, I. N. (eds.) Gravity and Geoid: Proceedings of 3rd Meeting of the International Gravity and Geoid Commission, Thessaloniki, 2002, pp 237-242, ZITI-Publishing
- Sneeuw N., Flury J., Rummel R. (2005) Science Requirements on Future Missions and Simulated Mission Scenarios. *Earth, Moon, and Planets*, 94:113-142, doi:10.1007/s11038-004-7605-x
- Sneeuw N., Sharifi M., Keller W. (2008a) Gravity recovery from formation flight missions. VI Hotine-Marussi Symposium on Theoretical and Computational Geodesy, International Association of Geodesy Symposia, 2008, Volume 132, Part I, 29-34, DOI: 10.1007/978-3-540-74584-6_5
- Sneeuw N., Sharifi M., Schaub H. (2008b) Formation flight stability in a gravitational field. Proc. 3rd Int. Sympo. on Formation Flight, Missions and Technologies, Noordwijk, the Netherlands, 23-25 April 2008 (ESA SP-654, June 2008)
- Strang G. (1986) Introduction to applied mathematics. Wellesley-Cambridge Press, Wellesley, MA
- Swenson S., Wahr J. (2006) Post-processing removal of correlated errors in GRACE data. *Geophys. Res. Lett.*, VOL. 33, L08402, 4 PP., 2006 doi:10.1029/2005GL025285
- Tapley BD, Bettadpure S, Watkins MM, Reigber C (2004a) The gravity recovery and climate experiment: mission overview and early results. *Geophys. Res. Lett.*, 31, L09607, doi:10.1029/2004GL019920
- Tapley BD, Bettadpure S, Ries JC, Thompson PF, Watkins MM (2004b) GRACE measurements of mass variability in the Earth system. *Science* 305, 503 (2004), doi: 10.1126/science. 1099192

Bibliography

- Thomas M. (2002) Ocean induced variations of Earth's rotation – results from a simultaneous model of global circulation and tides. Ph.D. diss., 129 pp., Univ. of Hamburg, Germany
- Torge W. (2001) Geodesy. Walter DeGruyter, Berlin.
- Van Dam T., Visser P., Sneeuw N., Losch M., Gruber T., Bamber J., Bierkens M., King M., Smit M. (2008) Monitoring and modeling individual sources of mass distribution and transport in the Earth system by means of satellites. Final report 20403, November 2008
- Velicogna I., Wahr J. (2002) Postglacial rebound and Earth's viscosity structure from GRACE. *J. Geophys. Res.*, 107 (B12), 2376, doi:10.1029/2001JB001735, 2002
- Velicogna I., Wahr J. (2005a) Greenland mass balance from GRACE. *Geophys. Res. Lett.*, Vol. 32, L18505, doi:10.1029/2005GL023955
- Velicogna I., Wahr J., Hanna E., Huybrechts P. (2005b) Short term mass variability in Greenland, from GRACE. *Geophys. Res. Lett.*, VOL. 32, L05501, doi:10.1029/2004GL021948
- Velicogna I., Wahr J. (2006a) Acceleration of greenland ice mass loss in spring 2004. *Nature*, 443, 329–331, doi:10.1038/nature05168
- Velicogna I., Wahr J. (2006b) Measurements of time-variable gravity show mass loss in Antarctica. *Science*, 311, 1754–1756
- Visser P. (2006) Space-borne gravimetry: progress, predictions and relevance for Swarm. Proceeding of first Swarm international workshop, ESA WPP-261.
- Visser P., Sneeuw N., Reubelt T., Losch M., van Dam T. (2010) Space-borne gravimetric satellite constellations and ocean tides: aliasing effects. *Geophys. J. Int.* 181, 789–805 doi: 10.1111/j.1365-246X.2010.04557.x
- Wahr J., Molenaar M., Bryan F. (1998) Time variability of the Earth's gravity field: Hydrological and oceanic effects and their possible detection using GRACE. *J. Geophys. Res.*, VOL. 103, NO. B12, PP. 30,205-30,229, 1998 doi:10.1029/98JB02844
- Wahr J., Swenson S., Velicogna I. (2006) Accuracy of GRACE mass estimates. *Geophys. Res. Lett.*, 33, L06401, doi:10.1029/2005GL025305.
- Wahr J., Swenson S., Zlotnicki V., Velicogna I. (2004) Time-variable gravity from GRACE: first results. *Geophys. Res. Lett.*, 31, L11501, doi:10.1029/2004GL019779.
- Walker J. S. (1991) Fast Fourier Transforms. CRC Press Inc., Boca Raton, FL, 1991.
- Wei Q. (2008) Mass variations in the system Earth and their impact on the gravity field. Nr. D205., Master thesis, Technische Universität München
- Wiese D.N., Folkner W.M., Nerem R.S. (2008) Alternative mission architectures for a gravity recovery satellite mission. *Journal of Geodesy*, DOI 10.1007/s00190-008-0274-1
- Wolff J.O., E. Maier-Reimer, S. Legutke (1996) The Hamburg Ocean Primitive Equation Model HOPE. Technical Report No. 13, DKRZ, Hamburg, 103pp, 1996.
- Wolff M. (1969) Direct measurements of the Earth's gravitational potential using a satellite Pair. *J. Geophys. Res.*, 74(22), 5295–5300

Bibliography

Zenner L. (2006) Zeitliche Schwerefeldvariationen aus GRACE und Hydrologiemodellen. Diplomarbeit, Technische Universität München

Zenner L., Gruber T., Jäggi A., Beutler G. (2010) Propagation of atmospheric model errors to gravity potential harmonics – impact on GRACE de-aliasing. *Geophys. J. Int.*, 182, 797-807, doi: 10.1111/j.1365-246x.2010.04669.x